



THÈSE

En vue de l'obtention du

DOCTORAT DE L'UNIVERSITÉ DE TOULOUSE

Délivré par Institut National Polytechnique de Toulouse
Discipline ou spécialité : Dynamique des fluides

Présentée et soutenue par Mehdi ELHIMER
Le 20/06/2012

The dynamics of neutrally buoyant particles in isotropic turbulence : an experimental study

JURY

M. Jacques BOREE	rapporteur
M. Jean-Charles SAUTET	rapporteur
Mme Véronique ROIG	Examineur
Mme Laurence BERGOUGNOUX	Examineur
M. Rudy BAZILE	Directeur de thèse
M. Olivier PRAUD	Co-Directeur de thèse

Ecole doctorale : Mécanique, Energétique, Génie Civil, Procédés (MEGEP)
Unité de recherche : *Institut de Mécanique des Fluides de Toulouse (IMFT)*
Directeur(s) de Thèse : O. Praud R. bazile

The dynamics of neutrally buoyant particles in isotropic turbulence : an experimental study

November 23, 2012

Remerciements

Je tiens d'abord à remercier Frédérique Risso et Sébastien Tanguy pour m'avoir accueilli pour la première fois à l'IMFT. Je remercie également Olivier Simonin pour m'avoir accueilli au groupe PSC (EEC à l'époque) et de m'avoir consacré du temps pour discuter ses travaux sur les écoulements gaz-particules.

Les expériences décrites dans ce mémoire n'aurait pu être réalisées sans le concours de Gérard Couteau qui a construit le générateur de turbulence et participé activement à sa conception. Je tiens à le remercier pour son engagement, son goût du « travail bien fait » et pour m'avoir consacré du temps pour de longues discussions fructueuses pour la résolution des problèmes rencontrés lors de la conception de l'expérience. A travers lui je tiens à remercier tous les membres de l'atelier de fabrication mécanique de l'IMFT. Je lui souhaite également une retraite heureuse.

Le dispositif de synchronisation a été conçu par la Hervé Ayrolles. Je le remercie pour m'avoir consacré du temps pour m'expliquer le fonctionnement du système et d'avoir pris le temps de résoudre les problèmes « d'impédance » ! La réussite des expériences, notamment des mesures de vitesses simultanées, doit beaucoup à la compétence du service signaux et images, en la personne de Sébastien Cazin, Moïse Marshal et Emmanuelle Cid.

Au long de ces quatre années, c'était un grand plaisir pour moi de partager le bureau avec mon collègue et ami Zafer Zeren. J'ai énormément apprécié ses soirées passées à discuter des aspects théoriques des écoulements gaz-particules et de la modélisation mésoscopique, même si ces travaux n'ont malheureusement pas pu aboutir. Je le remercie également pour m'avoir prêté oreille et pris le temps de m'écouter pendant les moments difficiles, et de m'avoir aidé à corriger ma thèse... *teşekkür ederim bash batteriste!* Je souhaite également remercier tous les autres collègues et amis du groupe PSC.

Je remercie les directeurs de mes travaux, Olivier Praud et Rudy Bazile, pour leur assistance tout au long du déroulement de la thèse. Leurs expertises en matière de méthodes de mesures a

permis de résoudre plusieurs problèmes, notamment concernant la mise en place des mesures simultanées. Je les remercie également d'avoir, avec patience, corrigé mon manuscrit et de m'avoir bien préparé pour la soutenance.

Enfin je remercie mon épouse Jing pour sa présence son aide et son écoute dans les moments difficiles, et mes parents pour leur soutien et leurs encouragements.

Abstract

In this experimental study, the focus is made on the characterization of the dynamics of solid neutrally buoyant particles embedded in a freely decaying, nearly isotropic turbulence, with a weak mean flow. The particles are spherical with diameters several times larger than the Kolmogorov scale. The study of this flow configuration is still challenging both theoretically and numerically. Due to large particle sizes, the local flow around particles can not be considered as uniform and due to fluid-particle density ratio of around unity, the history and Basset forces cannot be neglected in comparison with the viscous drag force. Particle equation of motion is then fully non-linear, in contrast to the equation for heavy particles with diameters smaller than the Kolmogorov scale, for which only the Stokes drag is considered.

In several experimental and numerical studies, the effect of particle size on velocity and acceleration statistics has been investigated (Homann & Bec 2010 ; Qureshi et al. 2008 ; Ouellette et al. 2008 ; Xu & Bodenschatz 2008). In the case of isotropic turbulence, Homann & Bec (2010) show that while the PDF of the particle velocity normalized by the square root of its variance does not vary with particle size, the variance itself is size dependent. A scaling relation for particle velocity variance has been proposed by using the Faxen correction (Gatignol 1983) which takes into account the non uniformity of the fluid flow at the scale of the particle.

The aim of our research is to further study the dependence of particle dynamics on particle size. To that purpose, a turbulence generator has been set-up and the resulting turbulence is characterized. Then the flow was seeded with millimeter sized, neutrally-buoyant particles and the velocity of the two phases have been measured simultaneously. Simultaneous measurements of particle and surrounding fluid velocities show that although the global velocity statistics of the two phases have comparable values, the particles may have different local velocity from the velocity of the neighboring fluid.

Table des matières

1	Introduction	9
1.1	General introduction	9
1.2	Turbulence	12
1.3	Point-particle model	14
1.4	Finite-sized neutrally buoyant particles	18
1.5	Previous works on finite size neutrally buoyant particles	22
2	Experimental set-up and techniques	29
2.1	Overview	29
2.2	Experimental set-up	29
2.2.1	Particles	33
2.3	Particle image velocimetry	35
2.3.1	Principle	35
2.3.2	Operation	37
2.4	Particle tracking velocimetry	42
2.5	Simultaneous velocimetry	48
2.5.1	Optical discrimination	49
2.5.2	Operation	52
2.6	References	56
3	Fluid turbulence	59
3.1	Overview	59
3.2	Large scale dynamics	59
3.3	Small scales dynamics	67
3.3.1	Velocity gradients statistics	67
3.3.2	Velocity differences statistics	75
3.4	Conclusions	78

3.5	References	81
4	Particle Dynamics	84
4.1	Overview	84
4.2	Turbulence modification	86
4.3	Velocity and position statistics	88
4.3.1	Results	88
4.3.2	Discussion	93
4.4	Velocity difference statistics	94
4.4.1	Results	95
4.4.2	Discussion	97
4.5	Conclusions	97
4.6	References	98
5	Conclusions and Perspectives	105

Liste des symboles

\dots_L	Averaging operator over the realizations
\dots_S	Spatial averaging operator over the whole measurement field
\dots_T	Total averaging operator
B	Cross-correlation pattern box (pixel)
d_p	Particle diameter (m)
$D_{L,i}$	Longitudinal structure function of the velocity component i
$D_{N,i}$	Transverse structure function of the velocity component i
δu	Velocity norm difference
η_k	Kolmogorov length scale (m)
λ	The Taylor length scale (m)
M	Grid mesh size (m)
Φ	Size ratio d_p/η_k
Re_λ	Reynolds number based on the Taylor length scale
S	Cross-correlation search box (pixel)
St	Stokes number
τ_k	Kolmogorov time scale (s)
τ_p	Particle relaxation time (s)
θ	Angle between particle velocity and fluid velocity (rad)
\vec{u}_{fp}	Fluid velocity at particle position (m/s)

\vec{u}_p	Particle velocity (m/s)
u_i	Velocity r.m.s along the component i (m/s)
U	Grid translation velocity (m/s)
$U_{m,i}$	Local mean velocity components (m/s)
$u_{t,i}$	Turbulent velocity components (m/s)
\vec{v}_r	Relative velocity between the fluid and the particle
w	Normalized relative velocity norm

1 Introduction

This chapter is dedicated to the introduction of the study presented in this thesis. Since the study involves turbulence, a brief introduction to this phenomena is given in the second subsection of this chapter. While only the classical view of turbulence is presented in this chapter, more recent aspects of the turbulent flows, such as their intermittency, will be discussed in the third chapter of the present thesis.

Different models of the motion of a solid particle in a fluid flow are presented. Beginning with the simplest and most used model : the point-like particle model, which consists on considering the particle as mass points, i.e. neglecting their size (and hence the related size effects) in comparison to the smallest eddy size of the flow. Some important results and predictions of this model are also presented. Then the more complicated and less understood case of particles with finite size (i.e. larger than the smallest scale of the flow) is presented. The study of the motion these particles is particularly challenging, since their equation of motion is fully non-linear.

1.1 General introduction

A large number of industrial and natural occurrences of the turbulent flows involve the presence of inclusion in fluid undergoing turbulent motion.

In nature one interesting example is the transport of aerosol particles in the atmosphere. These aerosol can both originate from natural phenomena (transport of sand by violent winds, airborne ash issued from volcanic activities ...) or industrial activities (pollution from industrial activities). In both cases, it is of interest to predict the evolution of the concentration of the aerosols in space and time, i.e. to be able to predict their diffusion in the atmosphere.

In the industry, the particle laden turbulent flow configuration is involved in a several reactive or non-reactive mixing process. One of the most studied in the literature being the combustion of fuel in thermal engines : generally the fuel is introduced into the combustion chamber as a spray and the resulting droplets interacts with the fluid turbulence in the combustion chamber and evaporates ; the understanding of the interaction of the fuel droplets with the flow is of interest to predict the rate of evaporation of the particles and the efficiency of the combustion reaction.

The understanding of particle–turbulence interaction is therefore of central importance for several scientific and engineering disciplines, and have drawn the attention of a wide research community.

Mainly these studies have been concerned with the study of particles with a size significantly larger than the smallest length scale of the flow, and density larger than the fluid density. This is mainly due to the relative simplicity of their equation of motion, since the dominant effect is the drag force. Albeit its simplicity, the dynamics of these kind of particles in a turbulent flow have shown a rich phenomenology, mainly controlled by their relaxation time, that is the time required to a particle to adapt it velocity to that of the surrounding fluid velocity.

When this time is sufficiently small compared to the smallest time scale of the flow, the particle can be considered as a tracer ; conversely, when this time is relatively large, the particles move in fashion which is often different from the surrounding fluid ; in this case the particle is called inertial. In addition, When the particle mass loading is sufficiently large (of the order of 10^{-2}) the presence of the particles may influence significantly the carrier turbulence statistical properties, resulting in “turbulence modulation” by the particles. Previous studies of particle-laden flows have shown that a dilute dispersion of fine particles can either augment or attenuate the carrier-phase turbulent kinetic energy. Other effects of particles presence have been reported in the literature, such the modification of the turbulence spectrum (Boivin et al. 1998).

One important aspect of the dynamics of inertial particles is their dispersion by turbulence, first investigated in the framework of the Tchen-Hinze theory (Hinze 1975). These studies have shown that the particles disperse less rapidly when increasing inertia. The diffusion of inertial particles have also been studied experimentally by Snyder & Lumley (1971).

More recent studies have emphasized other aspects of inertial particles dynamics : the inertial particles have been shown to form clusters, i.e. to concentrate preferentially in particular lo-

cations of the flow, this phenomena is known in the literature as “preferential concentration”. Inhomogeneous distributions of inertial particles in turbulent flows have also been observed in several experiments (Aliseda et al. 2002 ; Salazar et al. 2008) and simulations (Sundaram & Collins 1997 ; Collins & Keswani 2004 ; Fevrier et al. 2005). The clustering is due to the fact that in a turbulent flow, inertial particles with small to moderate inertia and sizes smaller than the Kolmogorov length scale tend to move to regions with high strain and low vorticity (Bec 2005).

Nevertheless, different flow configurations require to take into account the non-uniformity of the fluid flow at the scale of the particle size, or involve particles having a density close to the fluid density. In this cases the equation of motion of the particle is then fully non-linear, in opposition to the previous case of dense and point-like particles.

A direct numerical approach will consist on simulating the fluid flow at the vicinity of the surface of each particle in the flow. Although this approach yield interesting and fundamental results about the dynamics of finite size particles, it can not obviously be applied directly to cases involving a large number of particles or a highly turbulent and complex flows, since it is computationally costly. As an alternative one may seek for simplified models of particles motion in order to solve their motion. This model have to take into account the non-uniformity of the fluid flow at the scale of the particles and the interaction of the particle with its own wake, through the Basset-Boussinesq history term.

This aspect of particle dynamics in the case of neutrally buoyant particles have been studied by Ouelette & al. (2008), who measured simultaneously the velocity of the particles and the surrounding fluid, these particles were suspended in two-dimensional chaotic flow.

The aim of the present thesis is to generalize this study to the case of three-dimensional, fully turbulent flow. To our best knowledge, experimental comparison of local velocities in this case are still lacking.

To that purpose, a turbulence generator has been set-up and the resulting turbulence has been characterized. Then the flow was seeded with small, neutrally-buoyant particles and the velocities of the two phases have been measured simultaneously. This thesis is organized as follow, The rest of the present chapter is dedicated to the presentation of the particle equation of motion and the reviewing of previous experimental and numerical investigation of the dynamics of neutrally buoyant particles in turbulence.

In the second chapter, we will describe the constructed experimental set-up and the velocimetry techniques used in this study. The focus is made first on the design of the turbulence generator, aimed to yield an isotropic and homogeneous turbulence with a weak mean flow. Then we discuss how the the simultaneous velocimetry technique, based on optical discrimination between flow tracers and neutrally buoyant particles, have been adapted to our specific case.

The third chapter is dedicated to the study of the statistical properties of the generated turbulence in the absence of the particles. The departure from isotropy, homogeneity and local isotropy are quantified, and the characteristic length and time scales of the flow are measured. In the last chapter the dynamics of the particle is studied and is compared to the dynamics of the surrounding fluid, using the simultaneous velocimetry technique.

1.2 Turbulence

As we shall see, the dynamics of particles is directly affected by the properties of the turbulent flow by which their are carried. Turbulent flows are characterized by their complexity and the coexistence of fluid motion at different scales from the large scale at which the kinetic energy is produced to the smallest scales at which it is dissipated. In this section we will introduce some of the most important notions about turbulence that will be used later.

The focus is made on the case of homogeneous and isotropic turbulence where the two points velocity statistics are only dependent on the distance between the two points. Although such flows are not widespread in nature, they have been considered widely for the study on turbulence phenomena since they lead to simplified equations of the velocity statistics. In this subsection we will introduce some concepts and quantities pertaining to the turbulence phenomena, which will be extensively used in the following.

The central idea consists on considering the fluid motion to be organized in eddies of different sizes which are exchanging energy. The largest eddies are directly governed by the flow geometry and the turbulence generation mechanism (for example they have a size of the order of the the grid mesh in grid generated turbulence). Generally the kinetic energy, through the turbulence generation mechanism, is directly injected at these scales, they thus contain most of the flow kinetic energy.

Due to inertia, the large eddies beak-up in smaller and smaller eddies, in a process called *energy cascade* ; this lead to the coexistence of a whole range of eddy size in the turbulent

flow, the extension of which increases with the flow Reynolds number. At the end of the eddy breaking process, the eddy size become so small that the viscous effect dominate over the inertial effects. At those scales the kinetic energy of the flow is dissipated into heat by the effect of viscosity ; this range of eddies, responsible of most of the dissipation is called the dissipative range. In between, lies a range of eddies performing inertial energy exchange, where both the effects of viscous dissipation and large scales are negligible ; these eddies constitute what is called the inertial sub-range.

When the turbulence is in equilibrium, the dissipation rate of kinetic energy by viscosity matches the rate of energy transfer between the eddies. In this case, an important result is the fact that the statistics of eddies belonging to the inertial and dissipative scales are independent from the large scales and not dependent of the flow geometry. They have universal statistical features highlighted in the two Kolmogorov similarity hypothesis.

The first hypothesis states that in an isotropic turbulence with sufficiently high Reynolds number, the statistics of dissipative range are locally isotropic and only dependent on fluid viscosity and the value of the mean viscous energy dissipation. By combining the two parameters ν and ε on which the velocity statistics depends, we can obtain the two space and time scales $\eta_k = (\nu^3/\varepsilon)^{1/4}$, $\tau_k = (\nu/\varepsilon)^{1/2}$, called the Kolmogorov length and time scales.

The second hypothesis states that it exist a range of time and length scale, sufficiently smaller than the integral scale, where the velocity differences statistics at these scales depend uniquely on the dissipation. The scales where the second hypothesis is valid is referred to as the inertial sub-range. For all the time and space scales τ and r sufficiently larger than η_k and τ_k but sufficiently smaller than the large scales, all statistical laws depends only on the value of the viscous dissipation (Yaglom & Monin 1975).

These hypothesis have permitted an universal approach to the study of turbulent flows, since they can be applied to a wide variety of high Reynolds flow in nature and industry. In addition they have constituted an important basic theoretical framework to the study of such flows. Several predictions of the Kolmogorov hypothesis have been verified experimentally. Those prediction are mainly related to turbulence spectra shape, and turbulent kinetic energy decay rate and dynamics.

However, the small scales dynamics of the turbulence are not sufficiently well described by this theory. Different refinement to that theory have been added to the theory, mainly in order

to take into account the non-Gaussianity of the time or space increments of the fluid velocity field.

1.3 Point-particle model

This section is dedicated to the presentation of the equation of motion of a single particle in a fluid flow. These equations are of interest since they permit the modeling of the motion of a particle in a fluid flow. Generally this modeling can lead to interesting results pertaining to the kinetic energy or the dispersion of an ensemble of particles in a fluid flow.

There is no general equation for the motion of a particle of an arbitrary size in an arbitrary flow. In order to be able to write down equations, one needs to consider simplified flow configurations. The simplest flow configuration considered in the literature is the case of a uniform creeping flow (highly viscous flow) in the vicinity of the particle, with the particle moving with a constant velocity. In this case the Navier-Stokes equation around the particle can be simplified to yield a linear equation of motion for the particle. This simplification yields the point-like particle model, which is largely used in the literature due to its simplicity.

The local fluid flow around a spherical solid particle is resolved and the simplifying equations are used in order to permit the analytical solution of the flow around the particle and thus deduce the force applied on the inclusion.

In the limit of creeping flow, i.e. vanishing Reynolds numbers $Re \rightarrow 0$, the Navier-Stokes equations are simplified: the convective term representing the inertia is negligible compared to the viscous term which becomes:

$$\nabla p = \nu \nabla^2 \vec{u}_f, \quad \nabla \cdot \vec{u}_f = 0$$

The creeping flow can be considered as a vorticity diffusion process, with the motion of the particle in the fluid causing the vorticity production due to the no-slip condition on its surface. The produced vorticity diffuses from the particle surface to the outer fluid due to viscosity (Batchelor 2000). In the following, the vorticity diffusion equation is first set, then solved using the boundary conditions imposed by the no-slip condition on the surface of the particle and the uniformity of the flow field at infinity. This flow configuration is axis-symmetrical

about the particle axis thus we might use the ‘‘Stokes stream function’’ ψ which can be regarded as a definition a ‘‘potential vector’’ from which the fluid velocity field can be deduced (Batchelor 2000 ; Clift et al. 2005). Using this mathematical device, the fluid flow velocity field is resolved along with the pressure distribution around the particle, so the drag force experienced by the particle can be estimated. The case of unsteady motion is then analyzed in a similar fashion, and the general equations of particle in an unsteady creeping flow are eventually set.

First we consider the case of a spherical particle in a steady translational motion with a velocity \vec{U} parallel to the symmetry axis, in an otherwise still and unbounded creeping fluid flow. The viscous term in the Navier-Stokes equation can then be expressed in terms of vorticity $\vec{\omega} = \nabla \times \vec{u}_f$ by using the incompressibility condition we end up with an equation of the diffusion of the vorticity from the particle surface to the surrounding fluid as :

$$\nabla^2 \vec{\omega} = \vec{0}$$

In the case of axi-symmetric flow the fluid velocity field can be deduced from the stream function ψ , the value of $2\pi\psi(\vec{x})$ is the volumetric flow rate through a surface delimited by a circle centered on the axis of symmetry and passing by \vec{x} . The fluid velocity is related to the stream function by :

$$\vec{u}_f = \nabla \times \vec{B} \text{ with } \vec{B} = \frac{\psi}{r \sin \theta} \vec{e}_\phi$$

The vorticity is deduced from the stream function as :

$$\vec{\omega} = \nabla \times \vec{u}_f = \nabla \times (\nabla \times \vec{B})$$

And it can be shown that (Batchelor 2000) :

$$\vec{\omega} = \frac{E^2 \psi}{r \sin \theta} \vec{e}_\phi$$

with the operator E^2 being :

$$E^2 = \frac{\partial^2}{\partial r^2} + \frac{1}{r^2} \frac{\partial^2}{\partial \theta^2} - \frac{\cot \theta}{r^2} \frac{\partial}{\partial \theta}$$

To solve the vorticity diffusion equation we will rewrite it in terms of stream function :

$$\nabla^2 \vec{\omega} = -\nabla \times (\nabla \times \vec{\omega}) = -\frac{E^4 \psi}{(r \sin \theta)^2} \vec{e}_\phi = \vec{0}$$

Leading to the fourth order differential equation for the stream function :

$$E^4 \psi = 0$$

Finally we add the relevant boundary condition on ψ at the surface of the particle and at infinity to solve the equation above :

- No-slip condition : $\vec{u}_f = \vec{U}$ at the particle surface $r = r_p$
- Uniform stream flow at infinity $\vec{u}_f = \vec{0}$ as $r \rightarrow \infty$

Expressing these boundary conditions in terms of a stream function leads to the solution (Clift et al. 2005) :

$$\psi = U r^2 \sin^2 \theta \left(\frac{3 r_p}{4 r} - \frac{1 r_p^3}{4 r^3} \right)$$

To deduce the overall force applied by the fluid on the particle, we first evaluate the stress tensor at any point on the particle surface, then integrate it around the whole surface of the particle. The stress tensor at position $r = r_a$ is constituted from the normal stress tensor, deduced from the distribution of the pressure, and the tangential tensor deduced from the velocity distribution, the final expression for the Stokes drag force is :

$$\vec{F}_D = 3\pi d_p \mu \vec{U}$$

Now we consider the case of a sphere in rectilinear oscillatory motion along a unique mode ω in the sphere axis (Landau & Lifshitz 1987) :

$$U(t) = U_\omega e^{-i\omega t}$$

We first consider the simple case of translational oscillating motion of the particle with one mode, always under the creeping flow assumption the problem become an unsteady vorticity diffusion equation :

$$\frac{\partial}{\partial t} \vec{\omega} = \nu \nabla^2 \vec{\omega}$$

And it can be solved in the same fashion as above by the use of the stream function method.

The total drag on the sphere is obtained as above by integrating the stress tensor on the surface of the particle.

$$\vec{F}_D = 3\pi\mu d_p \vec{U} + \frac{\pi d_p^2}{12} \rho_f \frac{d\vec{U}}{dt} + \frac{3}{4} \pi d_p^2 \left(\frac{2\mu \vec{U}}{\delta} + \delta \rho_f \frac{d\vec{U}}{dt} \right)$$

Where δ is the distance from the particle surface beyond which the flow can be considered as non-rotational and below which the flow is rotational.

$$\delta = \sqrt{2\nu/\omega}$$

The first term of the equation of \vec{F}_D is the standard Stokes drag. The second is the “virtual added mass or the “acceleration response” of the surrounding fluid to the acceleration of the particle (Batchelor 2000). The virtual added mass term is the same as the one obtained from potential flow theory (i.e by considering the unsteady motion of a sphere in a potential inviscid flow) (Auton et al. 1988). These two terms are not related directly to the oscillation frequency ω so they can be understood as the permanent response of the fluid to the imposed oscillating particle motion. The two last terms are directly function of oscillation frequency and thus can be understood as the fluid transient response to the imposed particles oscillatory motion at a unique frequency ω . The generalization to multiple frequency motion and then to the general case of arbitrary motion is done by representing particle velocity as a Fourier integral :

$$U(t) = \int_{-\infty}^{\infty} U_{\omega} e^{-i\omega t} d\omega$$

Therefore, by integrating the transient fluid response term over all values of ω , the general equation of arbitrary motion for a spherical particle in a creeping flow is set :

$$\vec{F}_D = 3\pi\mu d_p \vec{U} + \frac{\pi d_p^3}{12} \rho_f \frac{d\vec{U}}{dt} + \frac{3}{2} d_p^2 \frac{\pi \rho_f \mu_f}{\pi \rho_f \mu_f} \int_{-\infty}^t \left(\frac{d\vec{U}}{dt} \right)_{t=s} \frac{ds}{t-s}$$

The last term in the above equation is commonly referred to as the “Basset history term” and includes the effect of past particle accelerations weighted as $(t-s)^{-1/2}$. The form of the

history term results from the vorticity diffusion from the surface of the particle (Clift et al. 2005 ; Landau & Lifshitz 1987).

This equation for small particles is very complex and different numerical studies (Bec 2005 ; Babiano et al. 2000) have used a simplified model taking into account only for the stokes drag force and the added mass :

$$\frac{d\vec{u}_p}{dt} = \beta \frac{d\vec{u}_f}{dt} + \frac{1}{\tau_p} (\vec{u}_f - \vec{u}_p)$$

Where $\beta = 3\rho_f/(\rho_f + 2\rho_p)$ is the added mass coefficient and $\tau_p = d_p^2/(12\beta\nu_f)$ is the particle relaxation time. When normalized by the Kolmogorov length scale of the flow the relaxation time gives the Stokes number of the particle $St = \tau_p/\tau_k$ this non-dimensional number is of importance since it characterize the inertial behavior of the particles. In addition, particles clustering is shown to be maximal for $St = 1$ by several authors (Bec 2005 ; Fevrier et al. 2005).

1.4 Finite-sized neutrally buoyant particles

The presented derivation above is the simplest one found in the literature and have been used only to set the basic theoretical framework. More general and rigorous derivations of the equation of motion have been proposed by several authors (Maxey 1983 ; Gatignol 1983) for the more general case of non-uniform creeping flow, and with the particle rotation and torque taken into account. The first to consider the effect of fluid flow local curvature on drag was Faxen, who shows that the local curvature introduce a correction on the drag force (Happel & Brenner 1983). For higher Reynolds numbers, i.e for non-creeping fluid flows, some experimental and numerical studies have tried to fit the equation issued from the creeping flow assumptions to high Re flows by recovering modified drag and added mass coefficient from their results (for reviews see E. E. Michaelides (1997) ; Efstathios E. Michaelides (2003) ; Clift et al. (2005)).

Faxen correction An equation for spherical particle motion taking into account the non-uniformity of the fluid velocity at the scale in a creeping flow have been proposed by several

authors (Maxey 1983 ; Gatignol 1983). The derivation performed is based on the distinction between unperturbed and perturbed flow field by the presence of the particles.

Each of the two flow fields is resolved separately, and so is the resultant stress tensor at the surface of the particle. The perturbed fluid flow is resolved by Fourier transforming the unsteady creeping flow equation, and the general solution is deduced from the particular solution in the case of uni-modal translational oscillating motion. The resulting force on the particle (and also the torque on the particle) is deduced by the integration of the stress tensor along the particle surface, which yields terms containing fluid velocity and acceleration integrals along particle surface and volume. The resulting particle modified equation of motion is (Gatignol 1983) :

$$\begin{aligned} \vec{F}_D = m_p \frac{d\vec{u}_p}{dt} = & -3\pi\mu_f d_p (\vec{u}_p - \langle \vec{u}_f \rangle_{S_p}) + \frac{\pi d_p^3}{6} \rho_f \left\langle \frac{d\vec{u}_f}{dt} \right\rangle_{V_p} + \frac{\pi d_p^3}{12} \rho_f \left(\left\langle \frac{d\vec{u}_f}{dt} \right\rangle_{V_p} - \frac{d\vec{u}_p}{dt} \right) \\ & + \frac{3}{2} d_p^2 \frac{\pi \rho_f \mu_f}{\pi \rho_f \mu_f} \int_{-\infty}^t \left(\left\langle \frac{d\vec{u}_f}{ds} \right\rangle_{S_p} - \frac{d\vec{u}_p}{ds} \right) \frac{ds}{t-s} \end{aligned}$$

Where

$$\langle \vec{u}_f \rangle_{S_p} = \frac{1}{\pi d_p^2} \int_{S_p} \vec{u}_f . dS \quad \text{and} \quad \left\langle \frac{d\vec{u}_f}{dt} \right\rangle_{V_p} = \frac{6}{\pi d_p^3} \int_{V_p} \frac{d\vec{u}_f}{dt} . dV$$

Are the fluid unperturbed velocity average along particle surface and the unperturbed fluid acceleration average along particle volume. If the particle diameter is sufficiently small $d_p/\lambda \ll 1$ the first order expansion of those quantities about the center of the sphere yields to (Gatignol 1983) :

$$\begin{aligned} \langle \vec{u}_f \rangle_{S_p} &= \vec{u}_{fp}(\vec{x}_p) + (d_p^2/24)\nabla^2 \vec{u}_{fp}(\vec{x}_p) + \mathcal{O}(d_p^4) \\ \left\langle \frac{d\vec{u}_f}{dt} \right\rangle_{V_p} &= \left(\frac{d}{dt} \right) (\vec{u}_{fp} + (d_p^2/40)\nabla^2 \vec{u}_{fp}(\vec{x}_p) + \mathcal{O}(d_p^4)) \end{aligned}$$

Where the $\vec{u}_{fp}(\vec{x}_p)$ and $\nabla^2 \vec{u}_{fp}(\vec{x}_p)$ are the unperturbed velocity and velocity gradients at the position of the particle \vec{x}_p . The first order of this Taylor development is called ‘‘Faxen correction’’ and account for the curvature of unperturbed flow at the particle location.

The case of neutrally buoyant particles is of interest as a reference because it ‘‘isolate’’ finite size effects : since $\rho_p = \rho_f$ the particles dynamics are expected to be affected mainly by

spatial filtering of the velocity field, instead of the dominant temporal filtering as in the case of small and heavy particle. It is also of experimental practical interest since it avoid particle dynamics to be effected by crossing trajectory effect due to gravity, and are the easiest to suspend in the absence of a strong mean motion as it is the case in our experiments. In addition, such particles are involved in several measurements techniques. Such examples include the use of large neutrally buoyant balloons to measure the turbulence Lagrangian spectra in the atmospheric boundary layer (Hanna 1981) or the use of large floaters (roughly 1m in scale) in the oceanic boundary layer (Lien et al. 1998).

In the case of neutrally buoyant particles, the slip velocity is small so in the limit of small particles size, i.e. for d_p/λ sufficiently small it can be shown that (Homann & Bec 2010) :

$$\vec{u}_p = \langle \vec{u}_f \rangle_{S_p} + \vec{u}_f + (d_p^2/24)\nabla^2\vec{u}_f + \mathcal{O}(d_p^4)$$

Stated differently, this means that particles behave like tracers with respect to the filtered undisturbed fluid velocity field $\langle \vec{u}_f \rangle_{S_p}$. This hypothesis have been the starting point of recent theoretical and numerical studies (Homann & Bec 2010), the aim of which is to understand how the spatial filtering may influence particles velocity and acceleration statistics. These studies have been interested in setting the limit of validity of the point-like particle model and proposing simple yet accurate models for finite size particles dynamics. This effort is mainly motivated by the obviously prohibitive computational cost of accurately computing the fluid flow at the scale of small yet finite-sized particles, specially for real world applications where a large number of particles is involved.

In the following, different theoretical implication regarding the particles velocity statistics are drawn from this minimal model. They mainly consist on scaling of two phase velocity differences statistics with particle size. Some of this scalings have been verified numerically by different authors, but to our best knowledge no experimental study have been dedicated to the verification of this minimal model.

A first consequence one can draw from this model is its inability to catch clustering effects, if any, since the resulting “ synthetic” particles velocity field is divergence free (Homann & Bec 2010). Another consequence is that the relative velocity is dependent on d_p^4 as leading order (Calzavarini et al. 2012) :

$$\vec{u}_p - \langle \vec{u}_f \rangle_{S_p} = \mathcal{O}(d_p^4)$$

We focus now on the behavior of velocity difference with changing particle diameter. By squaring the equation of the minimal model and retaining only second order terms in d_p^2 , we end up with :

$$\vec{u}_p^2 - \vec{u}_f^2 = \frac{d_p^2}{12} \vec{u}_f \cdot \nabla^2 \vec{u}_f$$

Considering the specific case of isotropic turbulence with no mean motion, the fluctuating and total velocities of the two phases are always equal, thus the Taylor length scale as $\lambda^2 \sim \langle \vec{u}_f \rangle / \langle |\nabla^2 \vec{u}_f| \rangle$ (Calzavarini et al. 2009). So by averaging the previous equation :

$$\langle \vec{u}_p^2 - \vec{u}_f^2 \rangle_T = \frac{d_p^2}{12} \langle \vec{u}_f \cdot \nabla^2 \vec{u}_f \rangle_T = -\frac{d_p^2}{12} \frac{\varepsilon}{\nu} = -\frac{5}{3} \langle \vec{u}_f^2 \rangle_T \left(\frac{d_p}{2\lambda} \right)^2$$

$$du = \frac{\langle (\vec{u}_p^2 - \vec{u}_f^2) \rangle_T}{\langle \vec{u}_f^2 \rangle_T} = -\frac{5}{3} \left(\frac{d_p}{2\lambda} \right)^2, \text{ with : } du = \frac{(\vec{u}_p^2 - \vec{u}_f^2)}{\langle \vec{u}_f^2 \rangle_T}$$

Where ε is the viscous dissipation and λ the Taylor scale estimated as $\lambda^2 = (5\nu \langle \vec{u}_f^2 \rangle) / \varepsilon$. An important consequence of this scaling is that it guaranties that the particles mean kinetic energy is always smaller than the fluid mean kinetic energy. This model is of importance since it permit a simple prediction on the kinetic energy of the particles from the knowledge of the kinetic energy of the fluid and the Taylor length scale of the flow. However, this minimal model need to be checked in the range of it is validity need to be set. As we shall see, at this point, no experimental verification of the scaling is provided in the literature.

In the next section we will present different numerical and experimental studies for the case of interest. we will summarize main conclusions of those studies and compare them to the those drawn from the minimal model.

1.5 Previous works on finite size neutrally buoyant particles

In this section, the main studies on the velocity statistics of finite sized neutrally buoyant particles embedded in a chaotic flow are reviewed. Important discrepancies between the different studies are stressed, and their accordance with the consequences of the minimal model presented previously is highlighted. Although no clear conclusion can be drawn on the dependence of velocity statistics on particles size, all the presented studies agree on the similarity of the normalized velocity P.D.Fs of the two phase, regardless of the size of the particles. The two principal study cited here have been devoted to testing and discussing the consequences of the minimal model on velocity statistics. Only the individual dynamics of the particles have been considered, and the back effect of particles on the fluid is not considered. Other recent studies have been concerned with the case of relatively higher mass loading and how then carrier turbulent flow is modified. Since our study is concerned with the small the volume loading, the modification of turbulence by the presence of neutrally buoyant particles is not reviewed here, interested readers are referred to studies such as (Yeo et al. 2010).

What is measured We first present the numerical methods and experimental techniques used by the different reviewed studies, along with their framework and parameters. Prior to any comparison, we first define clearly what is actually measured by the different investigators and under which experimental conditions or numerical parameters.

Beginning with numerical studies, in the latest work of Calzavarini et al. (2012), different Lagrangian model equations are used to track the particle in the fluid flow field. These models are : the classical stokesian model (with constant drag and added mass coefficients); the non stockesian drag (with a particle Reynolds number dependent drag coefficient); and the viscous drag (with history term addition). The three different Lagrangian models are used to resolve the acceleration (and hence the velocity) of the particle from the values of the filtered fluid velocity and acceleration. First the stokesian drag and added mass are activated then the other force terms, with the aim to investigate the influence of the different force terms on the particles velocity statistics. The Lagrangian model is one way, so that the presence of the particle do not modify the fluid velocity around, the measured fluid velocity at the position of the particle is thus truly unperturbed and fits the rigorous definition given by the theory. The implementation of the Faxen is based on a Gaussian approximation : the filtered

velocity field $\langle \vec{u}_f \rangle_{S_p}$ is first computed by applying a convolution with a Gaussian envelope on the fluid velocity field (Calzavarini et al. 2009). The Gaussian filter do not correspond to the rigorous definition of the spatial filtering on a spherical shell, but have been used by the author because it is computationally less expensive.

In Homann & Bec (2010) study, no Lagrangian model is used, instead a pseudo-penalization method is used to impose a no-slip condition at the surface of the particle. It consist on imposing a strong drag on the fluid at the location of the particle, so it tend rapidly to a solid motion. The hydrodynamical force experienced by the particle is computed by integrating the stress tensor over a homogeneous grid located at the surface of the spherical particle. Then the surface integral of the fluid velocity $\langle \vec{u}_{fp} \rangle_{S_p}$ is computed from evaluating the average velocity on spherical shells surrounding the particle. Only one particle at time was used in order to avoid particle-particle hydrodynamical interactions. These simulations take into account local disturbance of the fluid flow by the presence of the particle (as noted by the authors a wake like structure is visible in the vicinity of the particle). Computations were conducted for a moderate Reynolds number of $Re_\lambda = 32$, the ratio between particles diameter and the Kolmogorov length scale Φ between 2 and 14.

Two experimental studies are reviewed here, In the first investigation made by Qureshi (2009) (see also Qureshi et al. (2007)) the turbulence is generated behind a grid in a closed wind tunnel with a mean velocity of the fluid $U = 15 \text{ m.s}^{-1}$. The used particles are actually soap bubbles inflated with helium in order to match their density to the surrounding air. The particles are injected individually the resulting seeding is thus very small and no turbulence modulation is expected. Using a 1D acoustic Doppler velocimetry particles are individually tracked and their stream wise velocity component is measured along their trajectory. Fluid velocity is measured separately using hot wire anemometry (prior to seeding).

In a different series of experiments made by Ouellette et al. (2008), a quasi two dimensional flow is generated by driving electromagnetically a thin layer of an electrolytic *KCl* solution using a square lattice of permanent magnet with alternating polarity. The flow is seeded with particle of different diameters. The one of $80 \mu\text{m}$ diameter are used as tracers, the remaining particles of diameter 0.92 mm and 2 mm are the finite size particles with Stokes numbers between $0.5 \times 10^{-2} \leq St_L \leq 7.6 \times 10^{-2}$ based on the distance L between the magnets . A visualization zone of $7.5 \text{ cm} \times 7.5 \text{ cm}$ is imaged at a frequency of 30Hz so the particles can be tracked, then velocity and acceleration are measured by fitting polynomials to short segment of trajectories.

Study	Re_L	Re_λ	L/η_k	λ/η_k	$\Phi = d_p/\eta_k$	d_p/λ	$St_L = \tau_p/T_L$	$St = \tau_p/\tau_k$	Remarks
HOMANN BEC	68	32	24	11.3	2 17	0.17 1.5			<i>pseudo – penalization method</i>
CALZAVARINI	95.45	31	35	11	0 32	0 2.9			<i>Lagrangian model</i>
QURESHI	1621 1758	155.6 165	243 270	23.3 24.65	12.5 25.06	0.53 1			<i>wind tunnel experiment</i>
OUELETTE	72 220	×	×	×	×	×	$0,53 \cdot 10^{-2}$ $7,6 \cdot 10^{-2}$	×	<i>2D chaotic flow experiment</i>
Present study		< 180			4 5			1 2	<i>towed grid turbulence</i>

TABLE 1.1: Previous studies parameters

Velocities statistics Several authors have compared the velocity P.D.F of the two phases for different values of Reynolds numbers and size ratios, in the case of neutrally buoyant particles. A common and fundamental observation is that the the P.D.F of the velocity normalized by variance is not effected by the size of the particles and fits well with a Gaussian distribution. In the case of 2D chaotic flow (Ouellette et al. 2008), the same observation is made by the investigators, although the normalization is by fluid velocity variance. A comparison with fluid velocity PDF is made and no sensible difference between the two is observed. interestingly enough this is the only direct comparison between fluid and particles velocity PDFs found in the literature.

Velocity variance difference As seen in the previous paragraph no clear influence of the particles size on velocity statistics have been observed by previous investigators. However the effect of particles size on particles velocity variance have been extensively studied in the case of isotropic turbulence. The aim of the numerical and theoretical studies reviewed here is to check the minimal model in order to assert to what extend does it describe accurately the particles dynamics statistical features.

The only experimental evidences of two phases velocity variance differences in the case of isotropic intense turbulence have been provided by Qureshi’s results, who shows that, in contradiction with all theoretical predictions, no influence of particles diameter is found on particles velocity fluctuation, which fluctuate slightly and with no clear trend around the value of fluid velocity fluctuation. This result is rather surprising with regard to the high size ratios involved : $\Phi > 12$ and $d_p/\lambda = 0.53 \quad 1$, it is also inconsistent with the theoretical prediction of d_p^2 variance growth. A closer examination of authors data shows a discrepancy between -3% and 8.7% in particles fluctuation levels compared to fluid velocity fluctuation level, which compare well with the values from numerical simulations but for smaller size ratios $\Phi \leq 4$.

Numerically, the most resolved simulation to our best knowledge are reported by Homann & Bec (2010). The pseudo-penalization method without the use of an a priori Lagrangian model offers higher accuracy but with a significantly higher computational cost. In this study the authors have compared the minimal model deduced from the first order Faxen correction to the actual velocity variance du from the simulations results. The authors show that the scaling fits well data for scales ration $\Phi < 4$ (This observation have been confirmed by Calzavarini's results).

For larger values of Φ the variance difference is shown to behave as $\Phi^{2/3}$ suggesting a scaling reminiscent of the inertial range scaling : the velocity variance difference may be interpreted as the second order Eulerian structure function of the velocity field, with d_p the spatial separation. Hence, following K41 theory this quantity should scale with $d_p^{2/3}$ for d_p included in the turbulence inertial sub-range. Authors then conclude that beyond this size ratios the inertial scale physics begin to dominate particles dynamics. Nevertheless this conclusion have to be taken cautiously since the inertial range is small in these simulations ($Re_\lambda = 32$) . The measured two phases velocity variance difference for $\Phi \leq 4$ is smaller than 10%. For $6 \leq \Phi \leq 14$ the difference ranges from 14% to 27%.

Calzavarini's study first focuses on the effects of different Lagrangian models on the two phases velocity variance differences. For size ratios smaller than $\Phi \leq 6$ the three considered models seems to yield to close values of variance differences. At higher size ratio different models results begin to diverge signally : the stokesian drag model is shown to be inconvenient since it leads to a particle velocity variance larger than that of the fluid which is presented by the authors as an unphysical results since particles cannot have on averages larger energy that the carrier fluid. This incoherence is cured by the addition of the non-stokesian term.

Still, the resulting model results show a large discrepancy with results from Homann & Bec (2010) study for large size ratios. Authors then conclude that the most complete model accounting for the Basset-Bousinesq history term is the one that fits the best Homann and Bec results, although no clear scaling for high size ratios is found from their results . Hence authors a propose a different explanation for the $2/3$ scaling introduced by previous authors : the change of scaling may be due to an effect of the viscous drag and specially the non-stokesian term.

Although no clear agreement is found between the two studies, an agreement is reached on the tendency of variance difference to increase with particles size. This observation still lack

an experimental support, since the only available experimental evidence do not share this conclusion.

References

- Aliseda, A. et al., 2002. Effect of preferential concentration on the settling velocity of heavy particles in homogeneous isotropic turbulence. *Journal of Fluid Mechanics*, 468(1), pp.77–105.
- Auton, T., Hunt, J. & Prud'Homme, M., 1988. The force exerted on a body in inviscid unsteady nonuniform rotational flow. *Journal of Fluid Mechanics*, 197, pp.241–257.
- Babiano, A. et al., 2000. Dynamics of a Small Neutrally Buoyant Sphere in a Fluid and Targeting in Hamiltonian Systems. *Physical Review Letters*, 84(25), p.5764.
- Bec, J., 2005. Multifractal Concentrations of Inertial Particles in Smooth Random Flows. *Journal of Fluid Mechanics*, 528(-1), pp.255-277.
- Boivin, M., Simonin, O. & Squires, K.D., 1998. Direct Numerical Simulation of Turbulence Modulation by Particles in Isotropic Turbulence. *Journal of Fluid Mechanics*, 375(-1), pp.235-263.
- Batchelor, G.K., 2000. *An introduction to fluid dynamics*, Cambridge Univ Pr.
- Calzavarini, E. et al., 2009. Acceleration Statistics of Finite-Sized Particles in Turbulent Flow : The Role of Faxen Forces. *Journal of Fluid Mechanics*, 630(-1), pp.179-189.
- Calzavarini, Enrico et al., 2012. Impact of trailing wake drag on the statistical properties and dynamics of finite-sized particle in turbulence. *Physica D : Nonlinear Phenomena*, 241(3), pp.237-244.
- Clift, R., Grace, J.R. & Weber, M.E., 2005. *Bubbles, Drops, and Particles*, Dover Publications.
- Collins, L.R. & Keswani, A., 2004. Reynolds number scaling of particle clustering in turbulent aerosols. *New Journal of Physics*, 6, p.119.

- Février, P., Simonin, O. & Squires, K.D., 2005. Partitioning of Particle Velocities in Gas solid Turbulent Flows into a Continuous Field and a Spatially Uncorrelated Random Distribution : Theoretical Formalism and Numerical Study. *Journal of Fluid Mechanics*, 533(-1), pp.1-46.
- Falkovich, G., Fouxon, A. & Stepanov, M., 2002. Acceleration of rain initiation by cloud turbulence. *Nature*, 419(6903), pp.151–154.
- Gatignol, R., 1983. The Faxén formulae for a rigid particle in an unsteady non-uniform Stokes flow. *J. Mec. Theor. Appl*, 1(2), pp.143–160.
- Hanna, S.R., 1981. Lagrangian and Eulerian time-scale relations in the daytime boundary layer. *J. Appl. Meteorol.* ;(United States), 20(3).
- Happel, J. & Brenner, H., 1983. *Low Reynolds Number Hydrodynamics : with special applications to particulate media* 1st ed., Springer.
- Hinze, J.O., 1975. *Turbulence* 2nd ed., McGraw-Hill Companies.
- Homann, H. & Bec, J., 2010. Finite-Size Effects in the Dynamics of Neutrally Buoyant Particles in Turbulent Flow. *Journal of Fluid Mechanics*, 651(-1), pp.81-91.
- Landau, L.D. & Lifshitz, E.M., 1987. *Fluid Mechanics*, Second Edition : Volume 6 2nd ed., Butterworth-Heinemann.
- Lien, R.-C., D’asaro, E.A. & Dairiki, G.T., 1998. Lagrangian Frequency Spectra of Vertical Velocity and Vorticity in High-Reynolds-Number Oceanic Turbulence. *Journal of Fluid Mechanics*, 362, pp.177-198.
- Maxey, M.R., 1983. Equation of motion for a small rigid sphere in a nonuniform flow. *Physics of Fluids*, 26(4), p.883.
- Michaelides, E. E., 1997. Review—The Transient Equation of Motion for Particles, Bubbles, and Droplets. *Journal of Fluids Engineering*, 119(2), pp.233-247.
- Michaelides, Efstathios E., 2003. Hydrodynamic Force and Heat/Mass Transfer From Particles, Bubbles, and Drops - The Freeman Scholar Lecture. *Journal of Fluids Engineering*, 125(2), pp.209-238.
- Ouellette, N.T., O’Malley, P.J.J. & Gollub, J.P., 2008. Transport of Finite-Sized Particles in Chaotic Flow. *Physical Review Letters*, 101(17), p.174504.

Qureshi, M.N., 2009. *Etude Experimentale de la Dynamique de Particules Inertielles dans une Turbulence de Grille en Soufflerie : Effets de Densité et de Taille Finie*. Grenoble : Université Joseph Fourier.

Qureshi, N.M. et al., 2007. Turbulent transport of material particles : An experimental study of finite size effects. *Physical review letters*, 99(18), p.184502.

Salazar, J.P.L.C. et al., 2008. Experimental and Numerical Investigation of Inertial Particle Clustering in Isotropic Turbulence. *Journal of Fluid Mechanics*, 600(-1), pp.245-256.

Snyder, W.H. & Lumley, J.L., 1971. Some Measurements of Particle Velocity Autocorrelation Functions in a Turbulent Flow. *Journal of Fluid Mechanics*, 48(01), pp.41-71.

Sundaram, S. & Collins, Lance R., 1997. Collision Statistics in an Isotropic Particle-Laden Turbulent Suspension. Part 1. Direct Numerical Simulations. *Journal of Fluid Mechanics*, 335, pp.75-109.

Tanaka, T. & Eaton, J.K., 2007. A correction method for measuring turbulence kinetic energy dissipation rate by PIV. *Experiments in Fluids*, 42(6), pp.893-902.

Yaglom, A.M. & Monin, A.S., 1975. *Statistical Fluid Mechanics : Mechanics of Turbulence* Dover Ed., Dover Publications Inc.

Yeo, K. et al., 2010. Modulation of homogeneous turbulence seeded with finite size bubbles or particles. *International Journal of Multiphase Flow*, 36(3), pp.221–233.

2 Experimental set-up and techniques

2.1 Overview

This chapter is dedicated to the description of both the experimental set-up and the velocimetry techniques used in this investigation.

In order to generate a nearly homogeneous and isotropic turbulent flow, a towed grid turbulence generator have been set-up. Its design is described and discussed in the first part of this chapter.

In order to measure the velocities of both phases simultaneously, two whole field velocimetry techniques have been combined in a two camera set-up. The two velocimetry techniques particle image velocimetry and particle tracking velocimetry are first introduced separately, then the combination of the two techniques is described.

2.2 Experimental set-up

Introduction Since the early days of the experimental investigation of turbulent flow, different apparatus have been used in order to generate, at the scale of the laboratory, highly turbulent flow with well defined properties. Due to the relative simplicity of its mathematical description, the homogeneous and isotropic study is a widely used academic configuration to study turbulent phenomena. From the beginning of experimental turbulence research (Townsend & Taylor 1948 ; Stewart & Townsend 1951 ; Batchelor 1953), the use of the grid

in wind tunnels was extensively used to generate turbulent flow with satisfying homogeneity and isotropy. This flow configuration however has several drawbacks, the most important being the weak turbulence intensity, that is ratio of the generated turbulent kinetic energy to the mean kinetic energy of the flow.

Then, an interesting feature is to generate an isotropic turbulent flow without mean motion : if the larger part of the injected energy is converted into turbulent motion, it is easier to generate highly turbulent flow. A classical example of such set-ups is the Von Karman flow, which consists on generating a turbulent flow between two counter rotating disks resulting in a flow with small mean motion. The main drawback of such apparatus is to show a certain small scale anisotropy (Ouellette et al. 2006). This set-up has however been successfully used for investigating the motion of inertial particles in turbulent flows (Volk, Calzavarini, et al. 2011).

Another widely reported method to generate mean flow free turbulence is diffusive turbulence : in this case the turbulence is produced by a steady flow and transported by turbulent diffusion of momentum far from the region where it was created. This leads to a stationary flow without advection but inhomogeneous in one direction (Risso & Fabre 1997). One method of generating diffusive turbulence is the oscillating grid setup, which has been used by several authors to study turbulent mixing layers (McKenna & McGillis 2004 ; Fernando & De Silva 1993). The turbulence is produced by a horizontal grid oscillating in the vertical direction inside a square tank. At a certain distance z far from the grid diffusive turbulence is obtained.

In their experiments Yang & Shy (2003) used a comparable apparatus to study the modification of settling velocities of heavy particles in an aqueous turbulence. It consists on a pair of vertically oscillating grids producing an intense stationary turbulence in the core region between the grids. It is shown that this region has almost zero mean velocities, and is roughly homogeneous in horizontal directions. In addition, the isotropy is nearly achieved with a velocity r.m.s ratio of 1.2 (Shy et al. 1997).

Another set-up consists on translating (rather than oscillating) the grid at a constant velocity from the bottom to the top of a water square tank. The grid is then kept fixed at the top of the tank and the turbulence is let to decay freely. Such a device, called towed grid turbulence generator, has been previously used for the study of quantum turbulence in liquid helium (Stalp et al. 1999). Recently C. Morize et al. (2005) (see also Cyprien Morize 2006) used this device in order to study the decay of an isotropic turbulence submitted to a bulk rotation.

For all those methods of turbulence generation, the existence of a mean secondary flow in the vertical plan have been observed in the different studies and found as a vortex of characteristic scale comparable to the height of the water tank . This secondary flow was measured by comparing the total kinetic energy and turbulent kinetic energy, the ratio was found to be 2 to 3 in the case of freely decaying turbulence (Morize 2006). Several authors (Fernando & De Silva 1993 ; Staplehurst et al. 2008) have proposed design criteria to reduce the strength of the secondary motion, this is discussed further.

Turbulence generator In our experimental study, the choice has been made on towed grid generated turbulence. One realization of the turbulent flow is produced by moving the grid upward, in a glass tank filled with filtered water, at a velocity of $U = 1 \text{ m/s}$ along a stroke of 0.5 m (with acceleration and deceleration along 0.1 m), the turbulence then decays freely until the next stroke. The tank is equipped with a surface tray, so the flow is not perturbed by the free surface motion.

To make converged statistics 500 independent realizations are considered. The grid is attached to a linear slide which is set in motion by an electrical motor connected to a controller. A schematic representation of the turbulence generator is shown in *figure 2.1* .

The electrical motor is synchronized to the image acquisition system through a specifically designed synchronization box designed by H. Ayrolle at the IMFT : this box generates a first signal to trigger one grid motion cycle. This cycle consists on first moving the grid down gently at a velocity of 0.1 m/s , then to move it up at a velocity of 1 m/s in order to generate the turbulence.

The box generates a second delayed signal to trigger camera acquisition during a user specified time interval (acquisition window). These two signals are synchronized to the frequency of the LASER source (*figure 2.2*). The delay between two successive grid motion cycles is set to 54.4 s equivalent to 1000 integral time scales ; such a large delay has been chosen in order to avoid sustaining the mean flow. In our experiments the initial time $t.U/M = 0$ is taken at the end of grid stroke. The PIV measurements are triggered at $t.U/M = 40$, where the turbulence is considered to be homogeneous and isotropic (Morize 2006).

Cycle motion repetitiveness has been assessed by checking the position of the grid in images taken at the same stage for several cycles. The position of the grid have been found not to

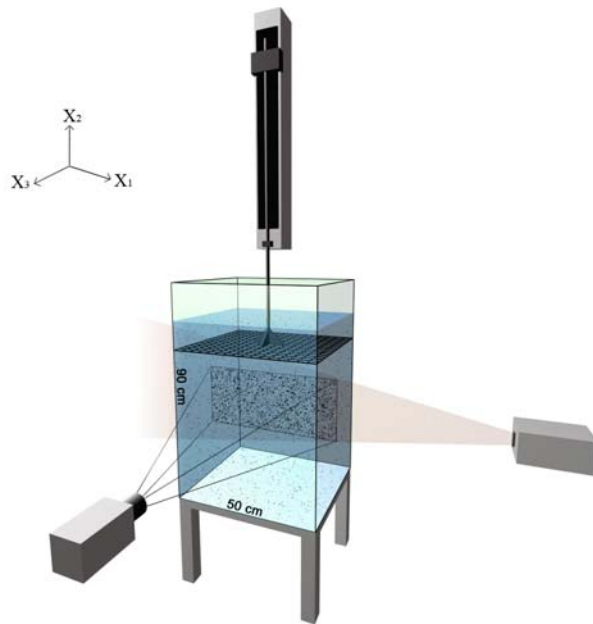


FIGURE 2.1: Scheme of the towed grid turbulence generator, with the PIV set-up. To generate the turbulent flow the grid moves upward in the water tank, the turbulence then decays freely until the next stroke of the grid.

vary noticeably, we thus conclude that the repetitiveness of the grid motion is satisfactory for the purposes of our experiments.

Grid design The most important part of the turbulence generation system is the grid, on which relies the quality of the generated turbulence. The first constraint on the grid design is the reduction of the mean flow ; Fernando & De Silva (1993) put forward a design criterion to reduce this flow by choosing judicious near wall conditions : The grid need to obey to reflective symmetry with reference to the walls of the tank. In their experiments two grid designs are tested : the first case corresponds to a grid design which respects symmetry criterion while in the second case the design does not match that criterion : the mean flow is shown to be reduced more than 4 times with the first design. The symmetry criterion has been respected when designing the grid : the spacing between the wall and the nearest parallel bar is half a grid mesh size $M/2$.

Another method to reduce the mean motion has been used by Staplehurst et al. (2008) : the authors have clamped a square tube to the back of the grid so that both the grid and the tube are lowered through the tank at the same time, and the authors report a diminution by a factor

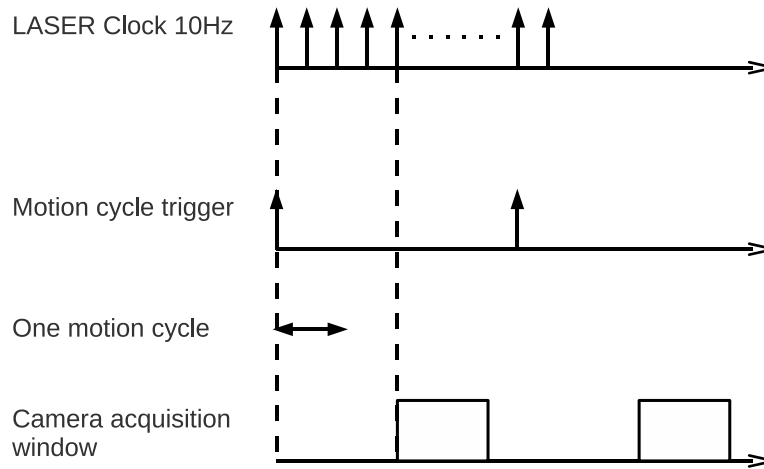


FIGURE 2.2: Scheme of the synchronization between grid motion and acquisition system.

of around 5 of the strength of the mean flow. Nevertheless this method is not used in our experimental set-up due to design restrictions.

As shown in *figure 2.3* the grid is made of square rods of sides 1cm with a mesh size $M = 4.5\text{cm}$, and a solidity $\sigma = 0.395$ which is close to the solidities of grids usually used in wind tunnels (Mohamed & Larue 1990). In order to avoid the deformation of the grid by the drag force applied by the fluid motion, the grid rods were made of duralium, an aluminum alloy. We have previously used a PVC plastic grid and observed a significant planar deformation, we thus rule out the use of this material. However rotational oscillations of the grid around the bar axis are noticed which may cause the grid to hit the tank walls and to cause scratchings on the glass walls ; to avoid this, we added Teflon (PTFE) pins at the both ends of the rods of the grid.

2.2.1 Particles

After characterizing the generated turbulence, the flow is seeded with solid particles made of polystyrene. It is important to note that particles are not injected but they are added to the water tank initially and they are used for all the experiments.

Polystyrene has been chosen because its density is the closest to that of water. To achieve

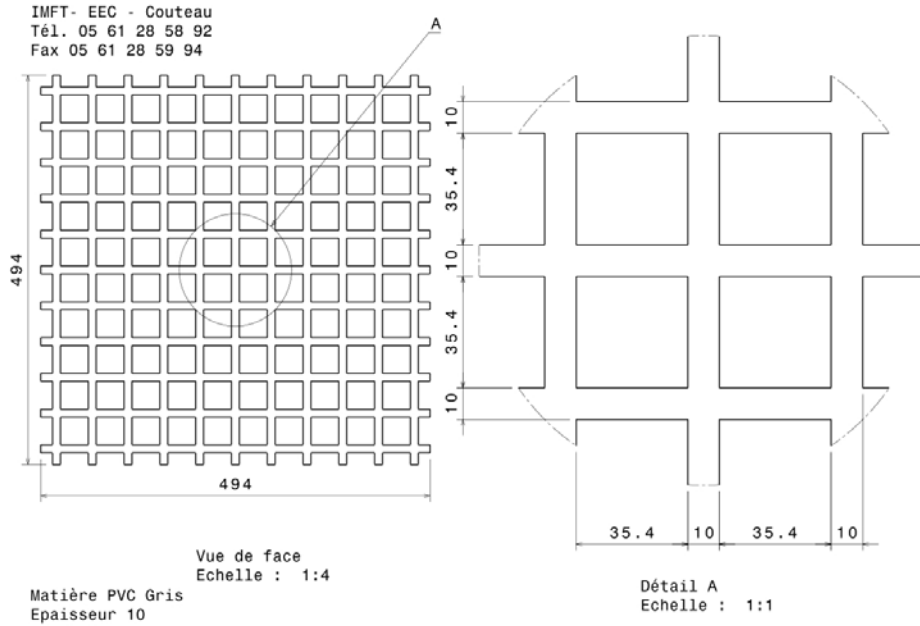


FIGURE 2.3: The used grid with the dimensions in millimeter

a better density match for the two phases water density is increased by salt addition and measured using a hydrometer before filling the tank (the water is filtered before filling the tank to eliminate both salt particles and dust particles). Then the settling velocity of the particles in the still water is measured by tracking the particles in successive images acquired by a camera. The settling velocity of the particles is found to be $V_s = 6.76 \cdot 10^{-4} \text{ m/s}$ in average for a measured water density of $\rho_f = 1.037 \text{ g/ml}$; this settling velocity is negligible compared to fluid velocity r.m.s u since $V_s/u = 2.24 \cdot 10^{-2}$ at $t.U/M = 66.6$ the particles buoyancy is thus considered to be negligible in comparison with the other forces .

We chose particles with diameters of around 1 mm , hence significantly larger than the Kolmogorov length scale, which is estimated to be of the order of $200 \mu\text{m}$; the achieved Stokes number close to 1. Prior to their use, the polystyrene particles were sieved to obtain a distribution of diameter between $d_p = 1.12 - 1.8 \text{ mm}$. We measured the diameters of a sample of 58 particle by imaging these particles, the histogram of measured diameters is shown in figure 2.4. The measured diameters are shown to vary between 1 mm and 1.5 mm , the dominant value being close to 1.4 mm .

The volume loading of the particles in the water tank was set to $\Phi_v = 3 \cdot 10^{-3}$; the choice of such a small loading is intended to make negligible both turbulence modulation and inter-

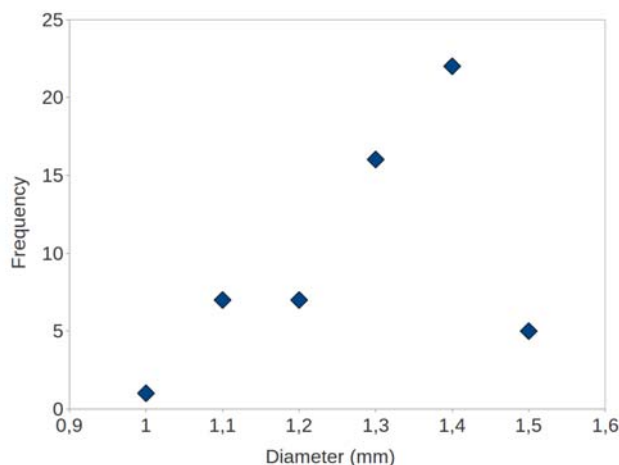


FIGURE 2.4: Histogram of used particles diameters

particle hydrodynamic interactions, while having a sufficient number of detected particles in the measurement volume.

2.3 Particle image velocimetry

2.3.1 Principle

At the contrary of the previous precise velocimetry techniques used in fluid mechanics, such as the Hot Wire Anemometer (HWA) which have been used in the first experimental investigations of the turbulence, or the more recent Laser Doppler Anemometer (LDA), the PIV yield the whole flow velocity field. Classical PIV techniques used hereinafter gives only two of the three velocity components over a measurements plan. Advanced PIV techniques such as stereoscopic PIV can give the three components.

From the pioneering research works in the eighty's (*e.g.* Utami & Ueno 1987) the particle image velocimetry technique have been set it self as one of the leading velocimetry methods in fluid mechanics. The use of digital imaging systems instead of photographic films have further increased the use of the PIV and simplified the batch processing of the resulting images.

The basic idea of the PIV technique is to measure the displacement of tracer particles of a given fluid flow between two successive images taken at a time Δt apart. The flow is seeded

with those tracers particles and illuminated using a light sheet, the commonly used light source is a dual cavity LASER : each cavity emits a Laser pulse, the two pulses are separated by a time Δt . The light is reflected by the tracers and received by a CCD sensor, the camera acquisition being synchronized with the LASER source to yield one image frame per cavity pulse. The method used hereinafter to deduce the tracers from the two successive acquired image is called “Correlation image velocimetry” (CIV) and have been introduced by Fincham & Spedding (1997), this method is described in the following.

The first frame images is subdivided into small pattern boxes of size B pixels, each box being centered around a node of a measurement grid defined by the user. Provided that B and Δt are small enough to yield reduced out-of-plan motion and in-plan tracers displacement, then most of the particle images contained in a pattern box of the first frame centered at coordinates (x_1, x_2) , will appear in the second frame within a search box of size $S = 2D_{max} + B$ where D_{max} is the estimated maximum in-plane flow displacement in pixels. Thus if the tracers undergo a simple translation $D < D_{max}$, the group of images within each box will retain a similar pattern.

A pattern matching technique is then best suited in order to calculate the displacement D of the tracer ensemble. The ensemble of the pixels contained in each pattern box in the first frame is cross-correlated with a shifted same size pattern box in the second frame, within the defined search box. For each applied shift a correlation coefficient is associated. This yields a two-dimensional correlation function, and the shifting corresponding to the largest local maxima of this function is the most likely mean integer displacement of the tracers contained in the pattern box. Furthermore, in order to achieve a sub-pixel accuracy a local curve fit of the correlation coefficient matrix is performed : the local maxima of the correlation function is fitted and the corresponding non-integer shift is computed.

However, the hence computed correlation peak may not be associated with the true displacement of the fluid in the sample box, especially when the correlations are weak, there is always some chance of a random pattern correlation giving vectors that are false. This is due to the presence of “secondary” local maxima of the correlation function, which may be larger than the “principal” local maxima associated with the actual particle motion. Those secondary peaks are associated with the random spatially uncorrelated errors and not to the actual displacement. The ratio of the principal to the secondary local maximas of the correlation function are called peak detectability (Adrian & Westerweel 2010), and may be understood as an analogous to the signal-to-noise ratio of the displacement measurement : an optimal PIV

measure yield a detectability significantly larger than 1.

In order to enhance the principal peak detectability the correlation function at a given position of the grid is multiplied by the correlation function at the neighbor position in the measurement grid (distant by $B/2$). Since the maximum of the correlation function, corresponding to the physical displacement, should be close at neighboring positions, the multiplication therefore enhance the strength of the principal peak, while reducing the strength of secondary peaks, since those peaks are related to a random error and are hence spatially uncorrelated. This method, called correlation based correction (CBC) technique, have been first proposed by Hart (2000).

After this process, false vectors do remain. Those vectors are unrelated to the neighboring flow, and should stand out when compared with their neighbors. In the CIV software a vector correcting routine is implemented which compares each vector with its neighbors computing the relative deviations in both magnitude and direction, the most deviant neighbor is discarded (Fincham & Spedding 1997). The results from this first iteration are improved in a second iteration with reduced pattern box search zone, using the prior knowledge of the local deformation rate and rotation is used to refine the pattern matching.

After describing the general principles of the used PIV technique, the imaging set-up and correlation parameters used in our measurements of the unladen turbulent flow will be presented and discussed.

2.3.2 Operation

The generated turbulence has been first characterized in the absence of the particles with Particle Image Velocimetry technique PIV, the velocity fields where computed using CIV software. The flow is seeded with borosilicate hollow glass spheres tracers of size $10\ \mu m$, which is significantly smaller than the flow Kolmogorov length scale. The tracers loading have been successively increased until reaching an average 45000 to 50000 tracers images per frame.

Laser Those tracers were illuminated using a vertical light sheet, which is generated by an Nd :YAG pulsed LASER light source with an energy output of $150mJ$ for each cavity,

at wavelength of $\lambda = 532 \text{ nm}$. The light sheet is formed by expanding the laser beam in the vertical direction by means of a cylindrical lens. Since the laser have a diameter (8mm) that does not match the desired thickness of the light sheet a long focal length spherical lens is applied to obtain the desired thickness, which can be tuned by varying the position of the spherical lens. Despite its simplicity , the main drawback of such a systems is that it does not yield to a constant laser sheet thickness ; this may be corrected by adding a cylindrical lens which corrects the diverging sheet into a collimated sheet (Adrian & Westerweel 2010).

We measured the light sheet thickness at the tank wall using a photosensitive paper. Due to the expected isotropic and tri-dimensional character of the flow, the LASER sheet thickness is taken equivalent to the interrogation window size B . For the present measurements, the interrogation window for the first cross-correlation is $B = 24 \text{ pixels}$, corresponding to 3.4 mm . In consequence, in order to reduce the out plan motion, the LASER sheet thickness need to be close to the interrogation window size B . Consequently, in our experiments the thickness being set to about 5 mm in the middle of the tank (note that this is an estimation based on the value of the thickness at the wall of the tank). As shown by PIV images the main drawback of the non constancy of the light thickness is to yield a non-uniform illumination of the measurement volume, since the illumination decay in the direction of the light propagation.

Since the velocity of the fluid varies significantly through the decay, the delay Δt between the two pulses is variable during the decay, from a value of $\Delta t = 9.10^{-3} \text{ s}$ at the beginning of the decay to $\Delta t = 25.10^{-3} \text{ s}$ at the end. The choice of the delay between the two pulses is conditioned by the desired average displacement of the tracers and by the reduction of the out-of-plane motion. The time between the two pulses should be chosen to achieve mean displacements sufficiently small in order to minimize displacement gradients and out-of-plane motion, yet sufficiently large to have significant measurements For the the values of Δt used, a typical measurement produces a mean displacement between $2 - 3 \text{ pixels}$ at every considered stage of the decay, which is expected to result in small displacement gradient in the interrogation window, reducing the corresponding bias (Raffel et al. 1998).

Prior to the measurements, in order to ensure that the two pulses used from the two cavities are focused on the same volume, we perform a co-linearity test. This test consists on cross-correlating the two images issued from laser pulses emitted from the two cavities at very small time lag apart, hence no motion of the tracers between the two pulses is expected . The resulting correlation coefficients are found to be larger than 0.8, thus proofing the good co linearity of the two cavities.

Camera The light scattered by tracers passes through an imaging system to be caught by a CCD sensor (PCO sensicam 12 bits), in two successive frames, each corresponding to one LASER pulse. Each cavity emits light pulses at a frequency of 10 Hz , the acquisition frequency of the CCD sensor being 5 Hz (the frequency of the camera is set by its read-out time).

First, the camera optical axis is first made perpendicular to the water tank wall, and the field of view of the camera was set to a size of 20 $cm \times 11.8 cm$ using a test card (*figure 2.5*) placed at the position of the desired measurement volume. This test card is also used to measure the magnification of the whole optical system, that is the correspondence pixel to millimeter.

Then the tuning of the optical system is performed : the aperture of the lens $f_{\#}$ should be large enough to enough scattered light, while yield a camera depth of field that is larger than light sheet thickness in order to avoid the presence of out of focus tracers images in the resulting PIV image.

The depth of field is related to the aperture number as $\delta_z = 4(1 + \frac{1}{M})^2 f_{\#}^2 \lambda$ (Raffel et al. 1998) where M is the magnification (the size of each pixel of the CCD sensor is 8 μm , the magnification is estimated as $M = 0.05$). For an aperture number of $f_{\#} = 4$ the depth-of-field is $\delta_z = 1.4 cm$ which is larger than the sheet thickness, thus for this aperture number all tracers images are expected to be in focus ; this confirmed by the visual inspection of PIV images. If the aperture number was reduced to $f_{\#} = 2$, the resulting depth of field will be equal to 3.5 mm which is smaller than the Laser sheet thickness, which may lead to significantly out-of-focus tracer images. Thus the aperture number $f_{\#} = 4$ is found to achieve the best compromise.

Besides, the size of the particle image should be larger than 1 *pixel* in average in order to reduce the bias of the measured displacements towards integer values, a phenomenon called “peak-locking” (Raffel et al. 1998). The expected focused tracer image size is given by the diffraction limited image diameter, which can be calculated using $\delta_s = 2.44 f_{\#} (M + 1) \lambda = 5.45 \mu m$, the tracer image size is hence smaller than a pixel size (8 μm) with the used aperture number. Instead of changing $f_{\#}$ we rather choose to de-focus slightly in order to “blur” and so increase tracers images size, the resulting size is found to be 1.8 *pixels* on average. This de-focusing have been found to reduce the peak-locking, by checking the resulting displacement histograms.

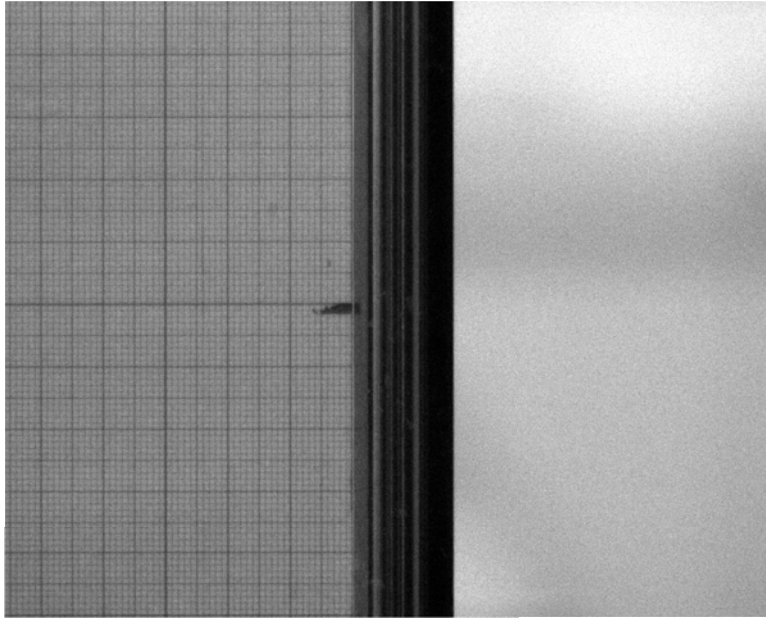
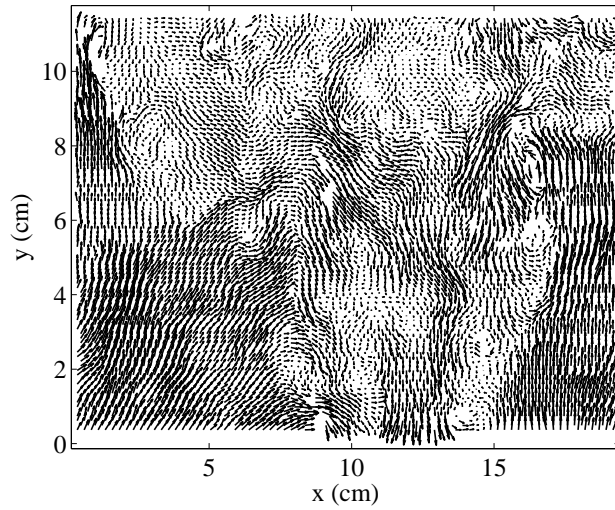


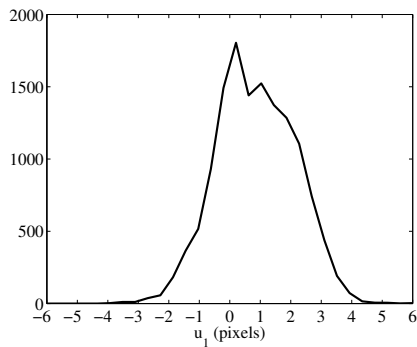
FIGURE 2.5: The used test card. The mark indicate the vertical center of the measurement volume and is matched with the center of the image.

Cross-correlation After the acquisition of the images, a cross-correlation analysis is performed in order to measure the tracers displacement between the two frames. The pattern box size is set to $B = 24 \text{ pixels}$ for the first interrogation and $B = 16 \text{ pixels}$ for the second, The search box sizes were set to $S = 48 \text{ pixels}$ for the first interrogation and $S = 40 \text{ pixels}$ for the second interrogation, yielding a maximal accessible displacement of 11 *pixels* in both cases.

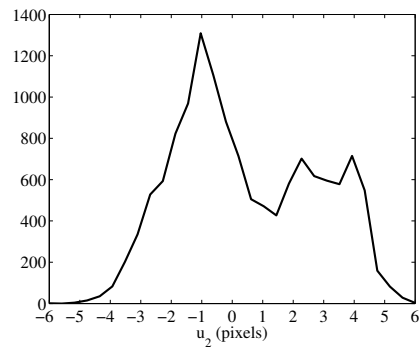
The choice of B and S sets respectively the spatial resolution and the dynamic range of the PIV measurement. In our case since $B/\eta_k \approx 10$, at the early stage of the decay ($t.U/M = 66.66$) small scales of the turbulence are not resolved by the present measurements. However our measurement's spatial resolution is sufficient to resolve Taylor scale λ since $B = \lambda/1.8$ at the beginning of the decay (For the estimation of both η_k and λ , see the chapter "Fluid turbulence"). The used search box size is found to be sufficiently large since a displacement of 11 *pixels* is rarely measured, the average displacement being 2 to 3 pixels. An example of the resulting PIV measures is shown *figure 2.6* : the resulting values of the correlation coefficient are mainly large than 0.5 proofing the quality of the cross-correlation analysis. Nevertheless, the inspection of the displacement histograms shows the occurrence of a slight peak-locking.



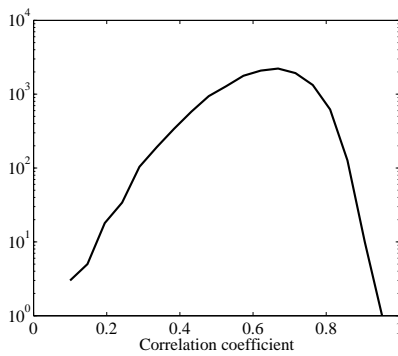
(a)



(b)



(c)



(d)

FIGURE 2.6: (a) Example of obtained PIV field, the number of vectors have been reduced for clarity. (b) and (c) Histogram of the displacements in pixels. (d) Histogram of the correlation coefficient.

2.4 Particle tracking velocimetry

The particle tracking velocimetry (PTV) technique consist on tracking the motion of individual particles between the two successive camera frames, in contrast with the PIV, which deals with an ensemble of particles contained in an interrogation window. Thus each particle image needs to be first detected on each camera frame and their positions estimated, then the two particles images need to be matched, i.e. identified as belonging to the same particle, without ambiguity ; the difference of position of the two particle images gives the particle displacement. Those three stages of the PTV process are detailed in the following.

Detection The acquired images consists of white particle images on dark background. Therefore, the common procedure for detecting particle images is by means of image segmentation : typically, a gray level-threshold applied to label all pixels with gray levels exceeding the threshold value as particle images and all other pixels as background. The pixels belonging to particle images are tagged 1 and the background pixels are tagged 0, the resulting images are hence called binarized images (*figure 2.7*).

A visual inspection of the acquired images shows that it contains a large number of particles images, all of them are not included in the measurement volume. The particles included in the thickness of the Laser sheet are considered to be the largest and the most illuminated particle images, the other particles outside the Laser sheet being illuminated through multiple scattering. The value of the size and gray scale threshold is then set to eliminate the later from the images ; after a visual inspection of the particles images we set the gray scale threshold to 10000 (while the maximum gray scale is 65535) and the size threshold to an equivalent diameter of the particles images of 4 *pixels*.

Other methods for particles detection have been reported in the literature. Takehara & Etoh (1998) have introduced the mask correlation method which is basically a pattern recognition method : it consists on cross-correlating the entire acquired image with a “mask”, *i.e.* a model particle image with Gaussian illumination profile, the correlation maxima then corresponds to the detected particles locations in the image. The authors show that this method works only when the particles images illumination profile is nearly Gaussian, which is not the case in our experiments since the particles saturate over several pixels. Another method used by Khalitov & Longmire (2002) is based on the detection of local maxima of the illumination

in the images. This method cannot be used in our experiments for the same reason : the saturation of the particle images over several pixels, i.e. the truncated illumination profile.

Centroid position After the detection of the particle image located in the measurement volume, the position of each detected object is estimated through its centroid. The centroid of each particle is computed as the barycenter of the ensemble of the pixels belonging to the binarized particle image weighted by their gray-level values. If the particle images are perfectly circular and the illumination profile perfectly symmetrical around the particle image center, this method yields an unbiased estimation particle image location. However, the centroid of particle images with an asymmetric shape yields a biased estimate for the particle location (Adrian & Westerweel 2010).

Thus an estimation of the circularity of the binarized particle image is needed in order to evaluate the bias on the centroid, this may be provided by the eccentricity : provided that the particle image may be approximated by an ellipse the eccentricity is the ratio of the distance between the foci's of the ellipse and its major axis length. The value is between 0 and 1 : an ellipse whose eccentricity is 0 is actually a circle, while an ellipse whose eccentricity is 1 is a parabola.

The histogram particle image eccentricities at $t.U/M = 84.4$ is shown in *figure 2.8* for the two camera frames : it is shown that most of the particle images can be considered as circular, since the most probable value of eccentricity is around 0.3 ; it shows however that a non negligible number of particles have an eccentricity larger than 0.6.

A visual inspection of some particle images having the largest eccentricities shows that some of them may cause erroneous displacement of the centroid between the two frames ; examples of the high eccentricity particles images causing erroneous displacement are shown in *table 2.1*. Some causes of errors are :

- The “crescent like” particle images, which are probably due to an obscuration by a particle outside the measurement volume.
- Particles which are too close to each other may be counted for as one object after image binarization (such problem may alternatively be resolved by eroding particle images in order to separate them).

Thus a threshold of eccentricity of 0.7 has been chosen in order to ensure a good symmetry of particles image used for the measurement and to avoid errors in the estimation of the displacement of the particles.

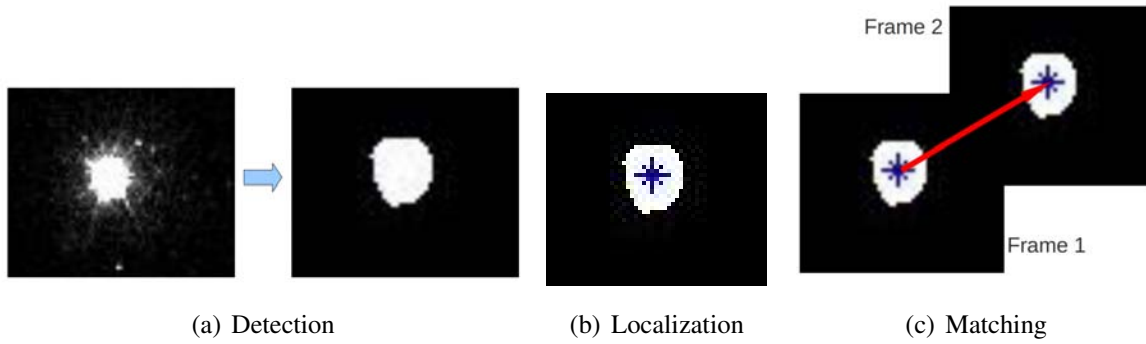


FIGURE 2.7: Particle tracking velocimetry process

When the bias errors are identical for particle image centroid on both frame, they cancel each other, and thus the measured particle displacement (which is the difference of the two centroid positions) is unaffected by this bias (Adrian & Westerweel 2010). However, when the particle shape changes significantly between the two frames, the bias errors are different and doesn't cancel each other, hence introducing a bias on the measurement of the displacement. Stated differently, the large variations of the particle shape between the two frames may induce a displacement of particle centroid which is different from the “physical” displacement of the particle.

Thus we verify the change of the shape of the binarized particle image between the two frames, by comparing the change in both eccentricity and diameter between the two frames. As depicted in *figure 2.9* the eccentricity and diameter are shown to be unchanged or slightly changed between the two frames. Thus, the measured particle displacement is often unaffected by bias on the particle centroid.

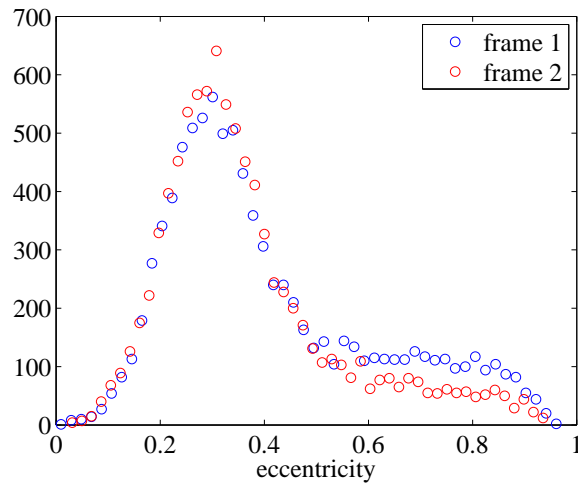


FIGURE 2.8: Histogram of the measured eccentricity of the detected particles image, on both of the camera frames.

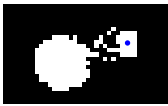




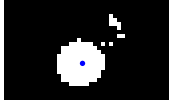

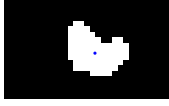
Frame1	Frame2	displacement (pixels)	eccentricity
		17.5906	0.8390
		19.3859	0.8473
		15.0862	0.8507
		12.2610	0.9033

TABLE 2.1: Examples of the cases of high eccentricities leading to erroneous centroid localization and displacements. The dots represents the position of the weighted centroid of the object.

Tracking After the detection and the estimation of the position of each particle image, the next step is to identify for each particle image in the first frame the corresponding image in

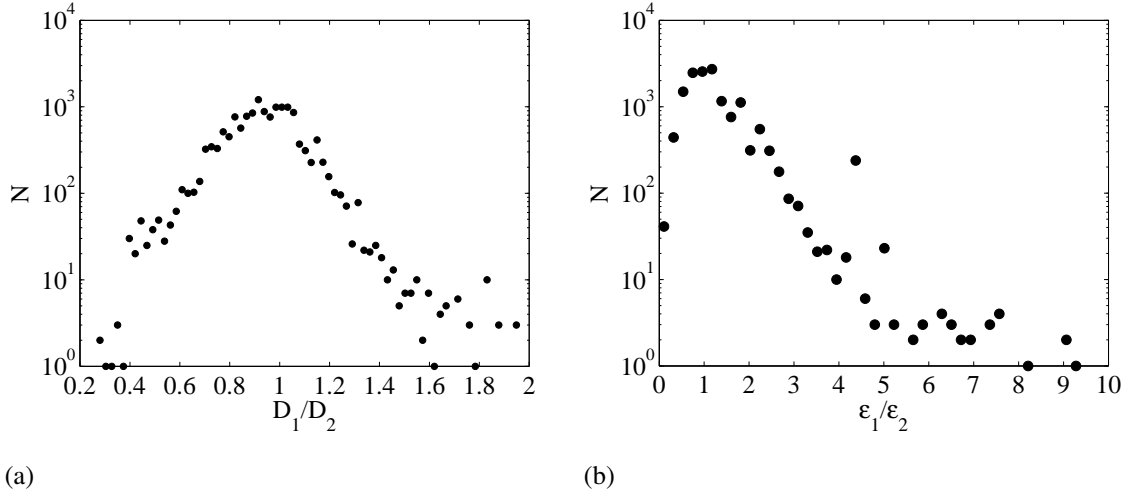


FIGURE 2.9: D_i and ε_i are the diameter and the eccentricity of the particle image in the frame $i = 1, 2$. For the two ratios the most probable value is 1

the second frame. When the displacement of the particle images is small with respect to the mean spacing of the particle images, the matching particles pairs can be found by pairing each particle image in the first frame with its closest neighbor in the second frame (Adrian & Westerweel 2010). This is verified in our case, since the mass loading is small.

For each particle image centroid, the tracking algorithm find the closest neighbor in the second frame within a search radius of 20 pixels. This limit have been validated by visually checking the largest detected displacement detected by the algorithm, and by verifying the resulting displacement histograms : if the search radius is too small, the histogram will be truncated at large values.

This tracking algorithm was tested in two ways :

First by applying a simple known movement to an image issued from the PTV measurement, and comparing the applied displacement to the one measured by the tracking algorithm. Thus, we impose a displacement by translating an image with equal values along the two directions x_1 and x_2 . Then the displacement computed by the algorithm D_{meas} is compared to the imposed displacement D_{imp} , and the average difference $\langle D_{meas} - D_{imp} \rangle$ is computed over the 300 images.

The results for different values of the imposed displacement D_{imp} are reported *figure 2.10*. The discrepancy is found to be on average smaller than one pixel for values of D_{imp} smaller

than 10 pixels. The average discrepancy then grows rapidly with the imposed displacement. Since the tracking algorithm matches each particle in the first frame to its neighbor in the second frame, an erroneous matching always leads to an underestimation of the actual displacement. This explains the fact that the average measured displacement is always larger than the imposed (actual) displacement.

In our measurements, the time between the two frames have been chosen to ensure a mean displacement of $5 - 7$ pixels; thus the resulting displacement measurements are weakly affected by the errors on particles matching.

The second test of the tracking algorithm was performed by applying a random known displacement on synthetic particle images, this test is described in details in the Master thesis of Jean (2011).

The test was performed for different numbers of particles in the images (densities) N_p and different maximal displacements D_{max} . For each of these parameters the ratio C of the number of correct matching to the total number of matching is computed and shown in figure 2.11. The results of the tests shows that more than 90% of the particles are correctly matched when the images contain less than 60 particles, even for largest maximum displacement of 15 pixels. In our experiments, the images contain 14 particles in average and the average displacement is between 5 and 7 pixels. Thus this tracking can be used confidently in our experiments, the matching rate is expected to be larger than 90%.

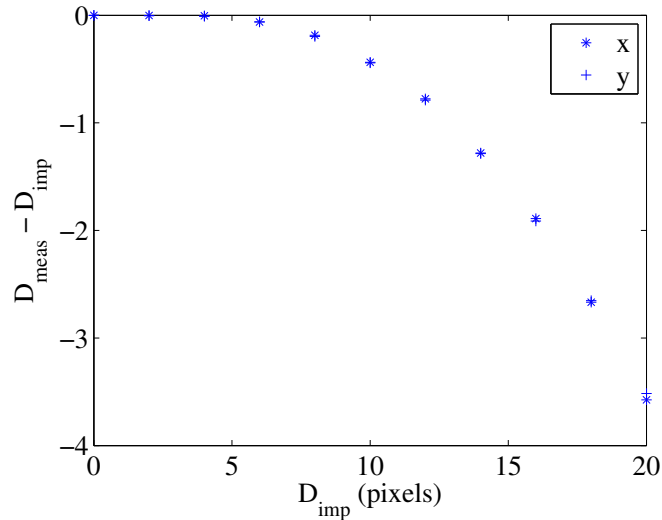


FIGURE 2.10: Imposed displacement D_{imp} against its difference with the mean measured displacement D_{meas}

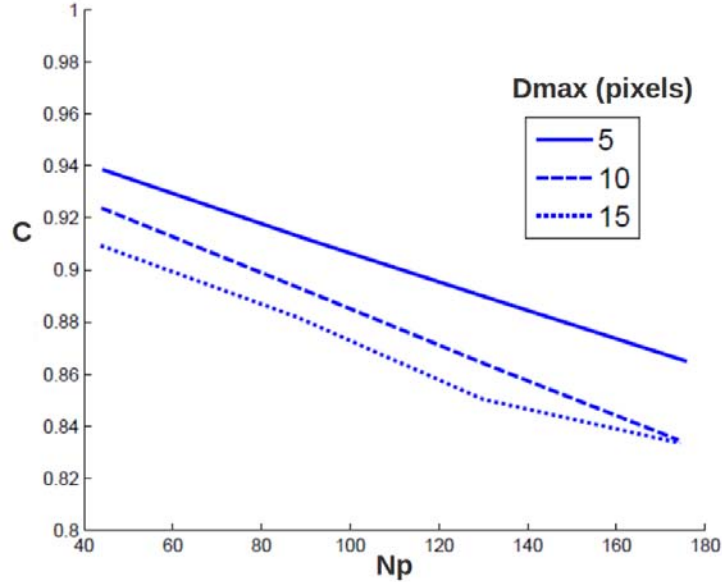


FIGURE 2.11: The rate of correct particles matching C versus the number of particles per image N , for different maximal displacements in pixels D_{max} . Results issued from tests on synthetic images performed by Jean (2011)

2.5 Simultaneous velocimetry

The aim of our experimental study is to measure simultaneously the velocities of the two phases and then to compare them locally. To that purpose, the velocimetry technique for the continuous phase (PIV) and dispersed phase (PTV) should be combined and operated simultaneously.

Several techniques are reported in the literature for combining the two techniques. One set of techniques is based on the separation of particle and fluid tracers images during the post-processing of the acquired image by means of various image processing techniques (Khalitov & Longmire 2002 ; Kiger & Pan 2000 ; Vignal 2006). Those techniques are based on the recognition of the large particle tracers, and their elimination from the image prior to the cross-correlation analysis of the resulting images. The main advantage of those methods is the simplicity of the associated set-up, since only one black & white camera is needed. The main drawbacks of such techniques are the presence of “holes” at the location of the eliminated particle images, which make it impossible to measure the velocity of the fluid sufficiently close to particle position.

2.5.1 Optical discrimination

Another set of methods is based on optical discrimination : each phase emits light at a different wavelength (color). This is generally done using a fluorescent dye encapsulated in the tracer particles. The fluorescent dye absorbs energy at the laser wavelength and emits light at a longer wave-length, i.e. with a different color, while the dispersed phase reflect the incoming light at the same wavelength.

To separate the two signals one may use a color camera to record the images and separation the two phases by their color (i.e. splitting the RGB channels) in the post-processing step. Another method consists on using a two camera set-up where each camera is dedicated to one phase ; the tracers dedicated camera being equipped with an appropriate cut-off filter in order to receive only the fluorescent light emitted by the tracers. This method have been successfully used by Poelma (2004) to study the modification of an isotropic turbulence due to the presence of the particles (see also Poelma, Westerweel, et al. (2005) and Poelma, Westerweel, et al. (2007)). We chose to use this method of phase discrimination for our experiments.

Thus, the flow was seeded with DANTEC fluorescent polymer tracers of size $20 - 50 \mu m$ and the dedicated camera equipped with a cut-off filter, thus receiving only the fluorescence signal and avoiding to catch the light reflected by the polystyrene particles (*figure 2.12*). As shown by the rhodamine absorption and emission spectrum (*figure 2.13*), the fluorescent tracers absorb the incoming light at a wavelength of $532 nm$ and re-emit it at a higher wavelength $> 550 nm$.

The used filter have a cut-off wavelength of $550 nm$ so a large part of the fluorescent light passes through the filter, while the light emitted by the particles is blocked, since its wavelength is significantly below the cut-off wavelength. However, a visual inspection of the resulting PIV images shows that the polystyrene particles appears on those images. This is explained by the fact that the particle do reflect the fluorescent light emitted by the tracers.

The presence of particle images may influence the cross-correlation results of PIV images and hence the resulting fluid tracer displacement : in order to eliminate them, we apply an intensity threshold to the PIV images prior to the cross-correlation. The chosen threshold have to be sufficiently large to eliminate particle images, while avoiding to eliminate too much tracers images, and preserving sufficient gray levels in order to ensure the quality of the cross-correlation. Based on these criteria, the chosen threshold is 6000, as shown in *figure 2.14* this threshold yields a particle free PIV images.

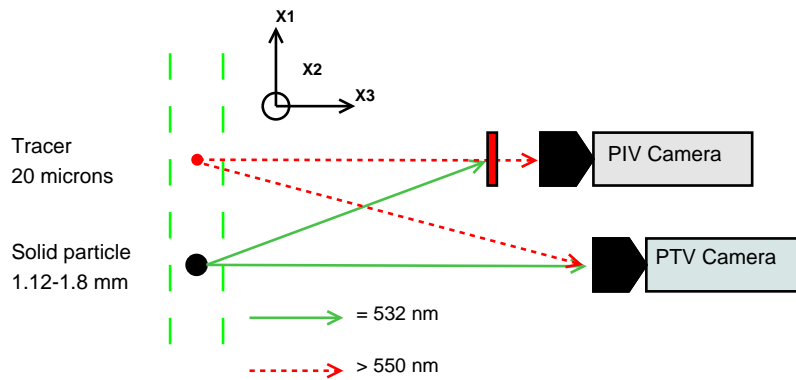


Figure 2.12: Simultaneous velocimetry set-up scheme. The fluorescent tracers absorb the incoming light at the LASER source wavelength 532 nm and re-emit it at a higher wavelength $> 550 \text{ nm}$. The PIV dedicated camera is equipped with an appropriate cut-off filter, thus receiving only the light emitted by the tracers.

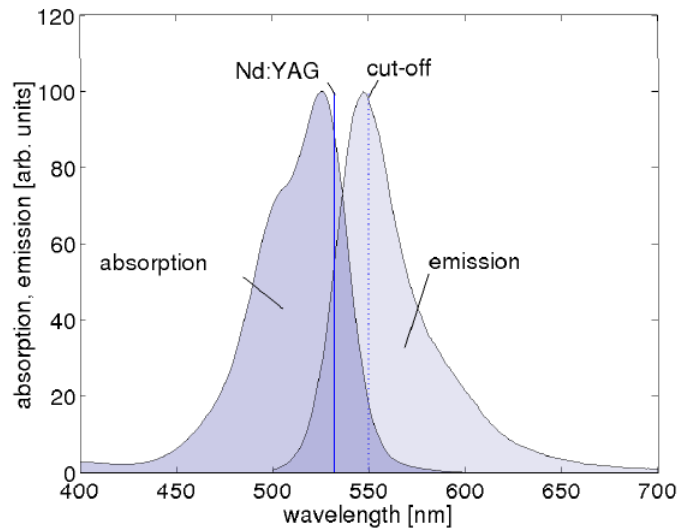
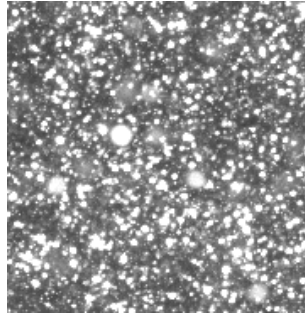
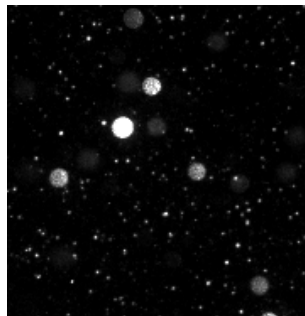


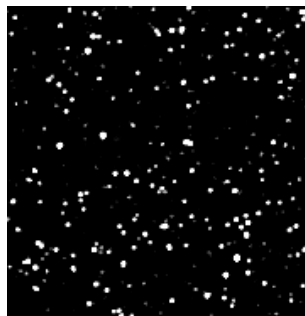
FIGURE 2.13: Emission and absorption spectra of the rhodamine, from Poelma (2004)



(a)



(b)



(c)

FIGURE 2.14: (a) Portion of the original PIV image, showing the presence of particle images in PIV images (b) corresponding PTV image (c) PIV image after thresholding at 6000

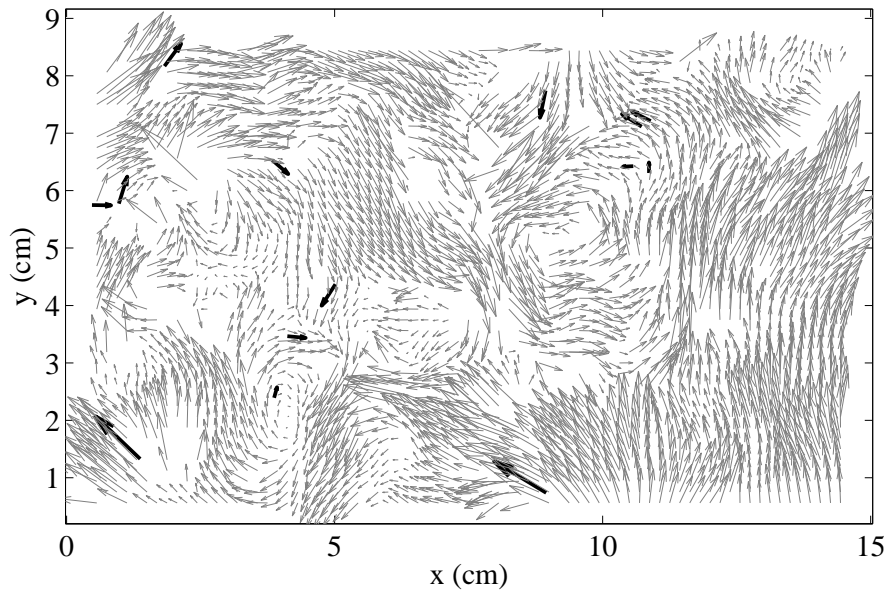
However, the resulting images are shown to be full of “holes” i.e. area void of tracers images, and to contain fewer gray levels. Thus, in order to ensure the good quality of the cross-correlation analysis, a large pattern box is needed. We chose a pattern box of size of $B = 64$ pixels with an overlap of 75%, this value have been shown to yield to an acceptable values of the correlation coefficient, although some resulting velocity vectors are non-valid, as suggested by the presence of “holes” in the velocity field (*figure 2.15*). This may be explained by both the observed holes in the PIV images, and the out-of-plane motion, since the time lag Δt between the Laser pulses have been increased and the light sheet thickness reduced, in comparison with the previous standard PIV measurements (see the next subsection).

Conversely, although the PTV camera catches both the images of tracers and particles. the applied thresholding for particles detection do eliminates the tracers images, so the resulting binarized image and the subsequent displacement measurements are not affected by the presence of the tracers.

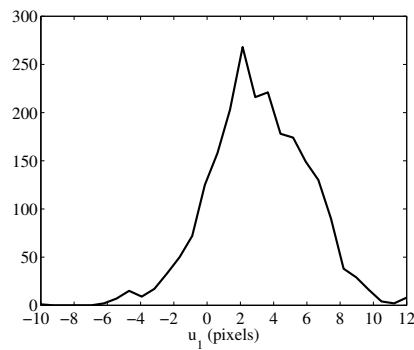
2.5.2 Operation

Camera The used velocimetry set-up is similar to a standard PIV set-up, except the use of two cameras and fluorescent tracers. The main difficulty of this set-up is to make the view field of the two cameras strictly identical. This is achieved by using a view field splitter (*figure 2.16*), which is an optical set-up constituted from an elliptical beam splitter and an elliptical mirror ; those two optical components are placed at 45° from the cameras optical axis so that their section seems circular. Two camera supports are associated to the view field splitter, which are designed to enable the fine tuning of the camera position along the three axis of translation and three axis of rotation. The relative positions of the two cameras in the horizontal plane is set in order to yield the same optical length and hence the same magnifications for both cameras, this is first checked by comparing the two images of the test card issued from each camera (the same issued card used for PIV) .

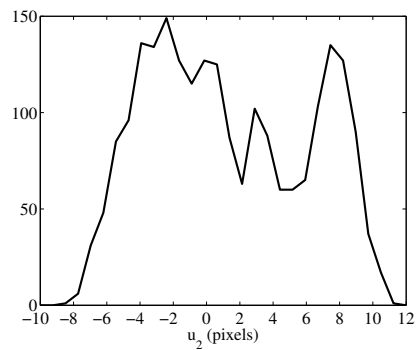
Before performing any measurement we need to verify that the two cameras are focused on exactly the same field of view. First the optical axes of both cameras are made perpendicular to the water tank wall, then the camera are made aligned precisely to each others: the position of the PIV camera is set and taken as a reference. Then both cameras are focused on a “calibration image” placed at the center of the water tank which is a computed generated synthetic tracers image (*figure 2.17*). Thus, the images captured by the two camera resemble



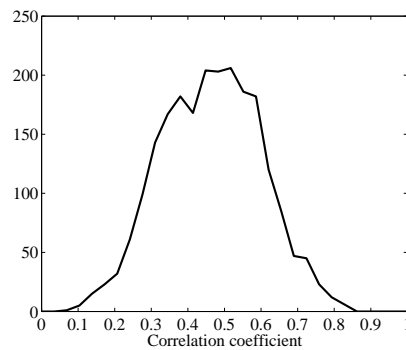
(a)



(b)



(c)



(d)

FIGURE 2.15: (a) Example of the two phases velocity fields : fluid velocity in gray and particle velocity in black (b) and (c) Histogram of the tracers displacements (c) Histogram of the correlation coefficient used from the PIV measurements on fluorescent tracers.

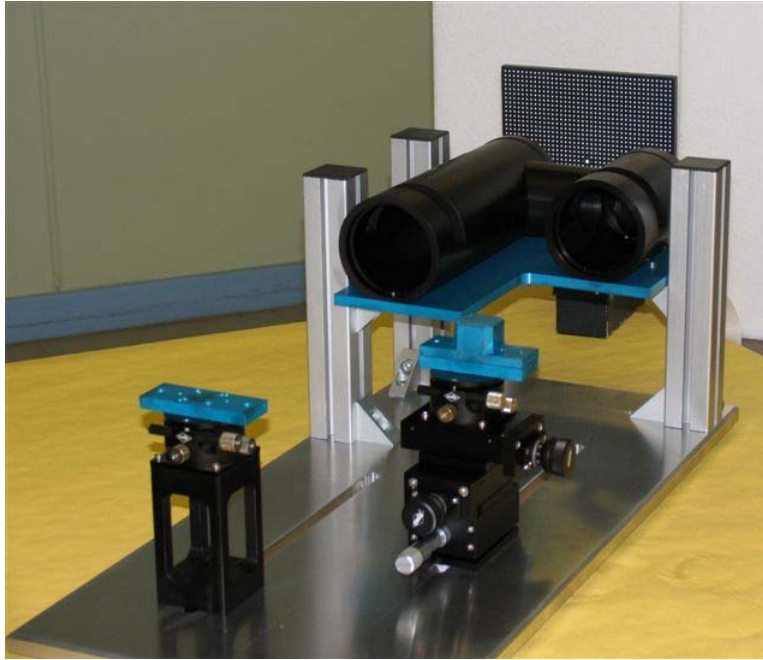


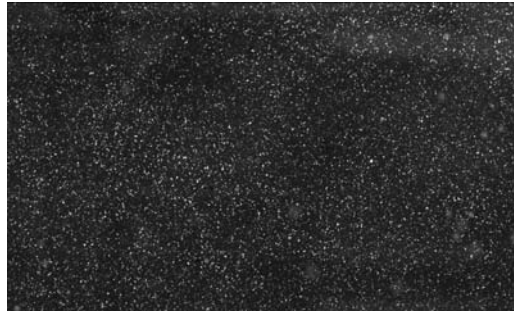
Figure 2.16: The field of view splitter and the two associated camera supports

to tracers image issued from a standard PIV set-up and can be cross-correlated in order to estimate the relative misalignment field between the two cameras. The calibration consist then on fine-tuning the position of the PTV camera in order to reduce this displacement and hence the related misalignment with the PIV camera. The final cross-correlation result is shown in *figure2.17* the misalignment ranges from 5 to 7 pixels.

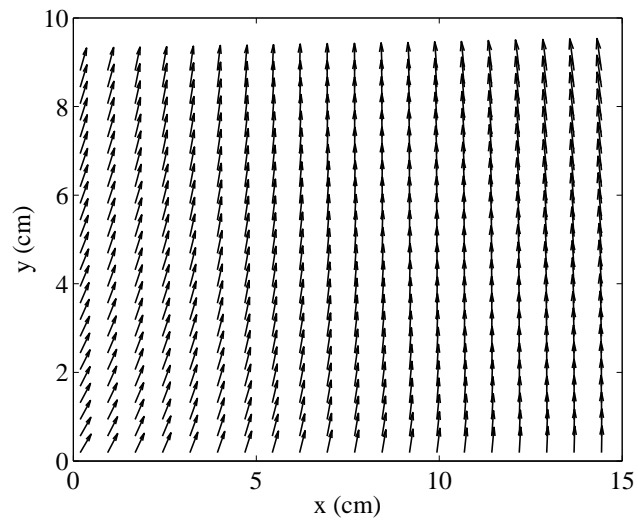
In the post-processing of PTV results, the misalignment field is used to correct the position of the particles. The calibration process is repeated at each measurements day: the camera position may slightly change due to different factors (*e.g.* temperature variation). The misalignment field is shown not to changes significantly, so the same misalignment field is used to correct particles positions for all the two phase flow realizations.

Laser In order to have a sufficiently intense fluorescent signal, the light received by the tracers should be increased. In order to maximize the the light received by the tracers, the power of the Laser source have been increased to 200 *mJ* and the thickness of the LASER sheet reduced to about 2 *mm*.

One of the difficulties of the simultaneous velocimetry is the choice of the time lag Δt between the two frames. The two used techniques PIV and PTV require different optimal values of



(a)



(b)

Figure 2.17: (a) The used calibration image (b) The measured misalignment between the cameras, the misalignment ranges from 5 to 7 pixels.

Δt , and a compromise is hence to be found. On one hand, in order to achieve optimal PIV measurements, the tracers displacement should be small on average (see previous section). On the other hand, in order to make the uncertainty on centroid position small in comparison to the measured displacement of the particles, it should be ideally larger in average than the particle image size, which is around 10 *pixels* ; such a large average displacement is not achievable since it will lead to a significant out-of-plan loss of particles images. Finally the time lag was set in order to achieve 5 – 7 *pixels* of average displacement for both phases.

An example of the results obtained from the simultaneous velocimetry is shown in *figure 2.15*. The particular advantage of this technique is remarkable: the velocity of the particles and the nearest fluid tracers can be measured simultaneously ; that is the presence of the particles do not yield to “holes” or false vectors in the fluid velocity field. Consequently, this velocimetry method is suited for the differences between the velocity of each particle and the surrounding fluid.

2.6 References

Adrian, R.J. & Westerweel, Jerry, 2010. *Particle Image Velocimetry*, Cambridge University Press.

Batchelor, G.K., 1953. *The Theory of Homogeneous Turbulence*, Cambridge University Press.

Fernando, H.J.S. & De Silva, I.P.D., 1993. Note on secondary flows in oscillating-grid, mixing-box experiments. *Physics of Fluids A: Fluid Dynamics*, 5, p.1849.

Fincham, A.M. & Spedding, G.R., 1997. Low cost, high resolution DPIV for measurement of turbulent fluid flow. *Experiments in Fluids*, 23(6), pp.449-462.

Hart, D.P., 2000. PIV error correction. *Experiments in Fluids*, 29(1), pp.13-22.

Jean, A., 2011. *Etude expérimentale du transport turbulent de particules de taille finie*. Institut de Mécanique des Fluides de Toulouse.

Khalitov, D.A. & Longmire, E.K., 2002. Simultaneous two-phase PIV by two-parameter phase discrimination. *Experiments in Fluids*, 32(2), pp.252-268.

- Kiger, K.T. & Pan, C., 2000. PIV technique for the simultaneous measurement of dilute two-phase flows. *Journal of Fluids Engineering*, 122, p.811.
- McKenna, S.P. & McGillis, W.R., 2004. Observations of flow repeatability and secondary circulation in an oscillating grid-stirred tank. *Physics of Fluids*, 16, p.3499.
- Mohamed, M.S. & Larue, J.C., 1990. The Decay Power Law in Grid-Generated Turbulence. *Journal of Fluid Mechanics*, 219(-1), pp.195-214.
- Morize, C., Moisy, F. & Rabaud, M., 2005. Decaying grid-generated turbulence in a rotating tank. *Physics of Fluids*, 17(9), p.095105.
- Morize, Cyprien, 2006. De la turbulence 3D en déclin à la turbulence anisotrope dominée par la rotation. *Université Denis Diderot - Paris VII*.
- Ouellette, N.T. et al., 2006. Small-scale anisotropy in Lagrangian turbulence. *New Journal of Physics*, 8(6), pp.102-102.
- Poelma, C., Westerweel, J. & Ooms, G., 2007. Particle-fluid interactions in grid-generated turbulence. *Journal of Fluid Mechanics*, 589(1), pp.315–351.
- Poelma, C., Westerweel, J. & Ooms, G., 2005. Turbulence statistics from optical whole-field measurements in particle-laden turbulence. *Experiments in Fluids*, 40(3), pp.347-363.
- Poelma, Christian, 2004. *Experiments in particle-laden turbulence*. Delft University of Technology.
- Risso, F. & Fabre, J., 1997. Diffusive Turbulence in a Confined Jet Experiment. *Journal of Fluid Mechanics*, 337(-1), pp.233-261.
- Raffel, M., Willert, C.E. & Kompenhans, J., 1998. *Particle image velocimetry: a practical guide*, Springer.
- Staplehurst, P.J., Davidson, P.A. & Dalziel, S.B., 2008. Structure Formation in Homogeneous Freely Decaying Rotating Turbulence. *Journal of Fluid Mechanics*, 598(-1), pp.81-105.
- Shy, S.S., Tang, C.Y. & Fann, S.Y., 1997. A nearly isotropic turbulence generated by a pair of vibrating grids. *Experimental Thermal and Fluid Science*, 14(3), pp.251-262.

Stalp, S.R., Skrbek, L. & Donnelly, R.J., 1999. Decay of Grid Turbulence in a Finite Channel. *Physical Review Letters*, 82(24), pp.4831-4834.

Stewart, R.W. & Townsend, A.A., 1951. Similarity and Self-Preservation in Isotropic Turbulence. *Philosophical Transactions of the Royal Society of London. Series A, Mathematical and Physical Sciences*, 243(867), pp.359 -386.

Takehara, K. & Etoh, T., 1998. A study on particle identification in PTV particle mask correlation method. *Journal of Visualization*, 1(3).

Townsend, A.A. & Taylor, G., 1948. Experimental Evidence for the Theory of Local Isotropy. *Mathematical Proceedings of the Cambridge Philosophical Society*, 44(04), pp.560-565.

Utami, T. & Ueno, T., 1987. Experimental Study on the Coherent Structure of Turbulent Open-Channel Flow Using Visualization and Picture Processing. *Journal of Fluid Mechanics*, 174(-1), pp.399-440.

Vignal, L., 2006. *Chute d un nuage de particules dans une turbulence diffusive. Etude des couplages entre phases par diagnostics optiques*. Thesis Institut National Polytechnique de Toulouse

Volk, R. et al., 2011. Dynamics of Inertial Particles in a Turbulent Von Kármán Flow. *Journal of Fluid Mechanics*, 668, pp.223-235.

Yang, T.S. & Shy, S.S., 2003. The settling velocity of heavy particles in an aqueous near-isotropic turbulence. *Physics of Fluids*, 15(4), pp.868-880.

3 Fluid turbulence

3.1 Overview

In this chapter the turbulent flow is characterized in the absence of the particles using the standard PIV technique. The aim is first to investigate the degree of homogeneity and isotropy of the turbulence and to appreciate the intensity of the mean motion.

Then the focus is made on the small scale dynamics of the generated turbulence. This is of primarily interest with regard to the study of the motion of the particles, since the local two phases velocity differences are mainly related to the dynamics of scales of the order or larger than the particle diameter. First the velocity gradients statistics, used for the estimation of the viscous dissipation, are presented ; then the velocity differences statistics for larger separations are computed. In both cases we asses the local isotropy of the generated flow. The flow resulting Reynolds number based on the Taylor scale λ was $Re_\lambda = 180$ at the stage of the decay $t.U/M = 66.6$, the generated flow is then fully turbulent at the beginning of the decay.

3.2 Large scale dynamics

In this section we are interested in the dynamics of the largest, energy containing scales of the generated turbulence. As shown by several authors (McKenna & McGillis 2004; Morize 2006), the confinement of the flow may generate a “secondary” mean flow; this mean flow will be first characterized through its spatial structure and its its strength in comparison with the turbulent motion.

Then the focus is made on the turbulent motion. First the isotropy and homogeneity of the turbulent motion are quantified and compared to the values found in the literature for the case of wind tunnel static grid generated turbulence without upstream contraction.

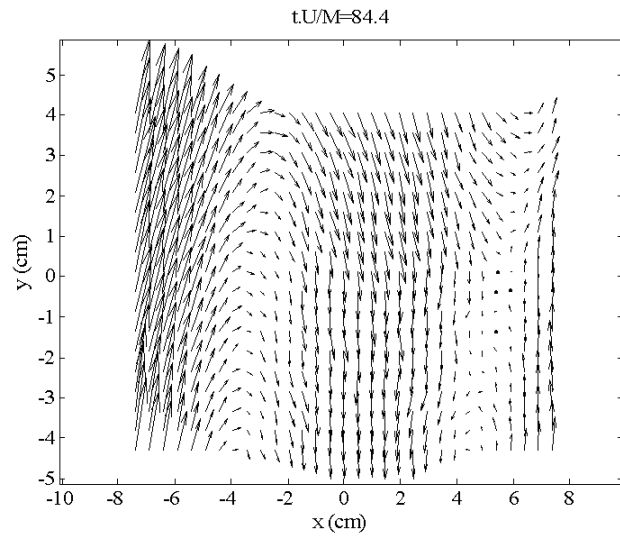
Finally the decay dynamics of the flow are investigated: we compute the decay exponent of the turbulence kinetic energy, and compare the measured temporal decay rate to an estimation of the viscous dissipation rate computed from the available turbulent velocity gradients. This comparison is made in order to evaluate the influence of the mean motion on the decay dynamics.

Since the flow is *a priori* not homogeneous, we shall make a difference between the average taken over the space and over the realizations. To that purpose we define the averaging operator over the realizations \dots_L , and the spatial averaging operator over the whole measurement field \dots_S . The total averaging operator is defined as the combination of the two operators and is written as $\dots_T = \dots_{LS}$. The local mean velocity components at each position (x_1, x_2) are $U_{m,i}(x_1, x_2) = \dots_L u_i(x_1, x_2)$ where u_i is the velocity component along the directions $i = 1, 2$. The turbulent velocity field is defined as $u_{t,i}(x_1, x_2) = u_i(x_1, x_2) - U_{m,i}(x_1, x_2)$ and the turbulent velocity r.m.s field is $u'_i(x_1, x_2) = \langle u_{t,i}^2 \rangle_L^{1/2}$. These averaging operators are used in the following.

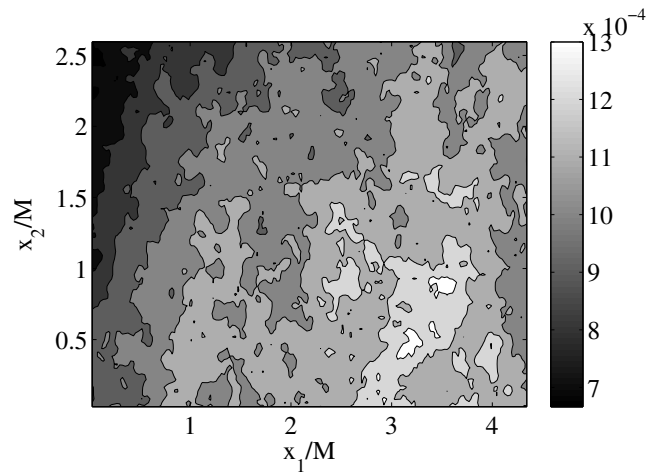
Mean motion First we verify the spatial configuration and intensity of the mean flow. In *figure 3.1* a snapshot of the mean velocity field \vec{U}_m is presented. The main observation concerns the particular spatial configuration of the mean flow : the velocity field shows vertical “streak-like” structures with alternating directions, the shape of which may recall the wake of the grid’s rods. However the periodicity of the Streak-like structures are different from that of the grids rods, so these streaks are not linked to the grid’s rod wake. The spatial structure of the mean flow seems also to change with the decay: the central streaks disappears while the two lateral streaks seems not to change in an important way.

At this point, no clear explanation to the observed spatial configuration of the mean flow is advanced. In addition, this observation is in contradiction with the observations of the mean flow in similar apparatus where the mean motion is in form of large vortical structure (Morize 2006).

One of the objectives of the construction of the turbulence generator is to generate a turbulent flow with the weakest mean flow possible. We need to show that the turbulent mean motion is



(a)



(b)

Figure 3.1: a) Mean velocity field at $t.U/M = 84.4$, the number of vectors have been reduced for clarity. Vertical “streak-like” structures are visible, with alternating up and down directions. b) Turbulent kinetic energy map at $t.U/M = 84.4$.

weak in comparison to the turbulent flow. i.e. the confinement do not generates an important mean flow, and the energy injected in the flow through the motion of the grid is mainly converted into turbulent motion.

The intensity of the turbulent motion compared to the mean motion is quantified through the ratio of the spatial averages of the turbulent kinetic energy to the kinetic energy of the mean motion $e_{c,t}/E_{c,m}$ where $e_{c,t} = \frac{1}{2}\langle 2u_1^2 + u_2^2 \rangle_S$ and $E_{c,m} = \frac{1}{2}\langle 2U_{m,1}^2 + U_{m,2}^2 \rangle$. This ratio is shown in *figure3.2* at different stages of the decay. From these figures, we conclude that the turbulent motion is always stronger than the mean motion (in the contrary of the what is the case for other turbulence generating setups, such as wind tunnel).

Isotropy and homogeneity Then, we verify both the homogeneity and isotropy of the turbulent motion. One of the consequences of the statistical isotropy of the turbulent flow is the condition of probability conservation under rotation which implies that the statistical moments of any order of the three velocity component are equal. For the second order statistics this yield :

$$\langle u_{r,1}^2 \rangle_L = \langle u_{r,2}^2 \rangle_L = \langle u_{r,3}^2 \rangle_L$$

The first consequence of the conservation under rotation have been verified at different times of the decay by computing the spatial average $I = \langle u_2^2/u_1^2 \rangle_S$ of the ratio of the two velocity components r.m.s. The ratio I remains in the range $[1.1, 1.2]$, which compares well with the values reported for static grid turbulence in a wind tunnel without contraction (Comte-Bellot & Corrsin 1966).

The turbulence generated in a static grid wind tunnel have been generally considered as homogeneous in two directions, and the main experimental results concerning isotropic turbulence have been obtained using such apparatus (Comte-Bellot & Corrsin 1966). However wall effects reduce the domain of lateral homogeneity, and different studies (Grant & Nisbet 1957; Ertunç et al. 2010) have shown important departure from homogeneity for different velocity statistics. In the case of cylindrical rod grid, Grant & Nisbet (1957) have measured the inhomogeneity of the mean velocity and the r.m.s of the fluctuating velocity in a plane normal to the mean flow situated at 80 mesh-sizes downstream the grid. The spatial dispersion compared to the mean of the fluctuating velocity r.m.s in the direction of the mean flow is found to have a maximum of 30%. However, no sensible spatial dispersion of the mean velocity in the stream wise direction have been found by the authors. The inhomogeneity

of the mean velocity stream wise have been measured by Ertunç et al. (2010) in a similar apparatus, and found of a maximal value of 2%.

In our case, in order to quantify turbulence's homogeneity, the mean spatial dispersion of the turbulent velocity r.m.s about the mean for the two measured components is obtained by using the quantity $H_i = 100 \left\langle (u_i - \langle u_i \rangle_S)^2 \right\rangle_S^{1/2} / \langle u_i \rangle_S$. Until $t.U/M = 150$, spatial dispersion is found smaller than 11%. The inhomogeneity is often greater for the r.m.s velocity in the direction of the grid motion, suggesting that the initial large scale inhomogeneity induced by the grid motion persists throughout the decay. This inhomogeneity may also originate from a non-negligible mean motion which occurs due to the confinement by the wall of the tank (McKenna & McGillis 2004). In *figure 3.1* we represents the spatial distribution of the turbulent kinetic energy of the flow at time $t.U/M = 84.4$.

Decay dynamics Now we turn attention to the temporal decay dynamics of the generated turbulence. For a homogeneous isotropic turbulence, the turbulent kinetic energy decay in time following a power law $e_{c,t} \sim t^{-n}$ where the value of the exponent is often found to be close to $n = 1$. The decay of the component energies is shown in *figure 3.2*, the measured decay exponent is found to be closer to $n = 1.1$, which is comparable with values reported in the literature for wind tunnel grid turbulence (Mohamed & Larue 1990).

The time decay of the turbulent kinetic energy at a given point is due to different mechanisms: convection by the mean motion, production by the mean shear, transport by turbulent fluctuations, viscous diffusion and viscous dissipation. Thus the production convection or diffusion of turbulent kinetic energy is due to mean motion or spatial homogeneity of the flow velocity field. In a homogeneous turbulence, the time variation of the turbulent kinetic energy is solely due to viscous dissipation which is related to the smaller scales of the turbulence spectra. Under the local isotropy hypothesis the viscous dissipation rate in our experiments may be computed from the available components of the velocity gradients $\varepsilon = 3\nu (\langle s_{11}^2 \rangle_L + \langle s_{22}^2 \rangle_L) + 12\nu \langle s_{12}^2 \rangle_L$ with $s_{ij} = \frac{1}{2} \left(\frac{\partial u_{t,i}}{\partial x_j} + \frac{\partial u_{t,j}}{\partial x_i} \right)$ being the local shear stress (Tanaka & Eaton 2007; Adrian & Westerweel 2010). However as it will be shown in the next section, the velocity gradients are not fully resolved due to the limited spatial resolution of our measurements. The computed values of velocity gradients statics are to be considered as rough estimations.

The resulting spatial average of the computed local viscous dissipation rate $\varepsilon_S = \varepsilon_S$ is compared to the decay rate of the mean turbulent kinetic energy $\varepsilon_T = -\frac{d}{dt} e_{t,S}$ (*figure 3.3*). These

two terms are equal in freely decaying isotropic turbulence. In our case however a significant discrepancy between the two dissipation rates is observed with ε_T being 50% larger than ε_S at $t.U/M = 60$. This non negligible discrepancy then decays until the two terms became equal at $t.U/M = 110$. This discrepancy may be explained by the underestimation of the velocity gradients due to the limited spatial resolution of the PIV measurements, thus leading to an underestimation of the viscous dissipation rate ε_S . However, it is not clear why this discrepancy reduces with time. Another possible explanation is the effect of the TKE production terms which are not included in ε_S .

Length and time scales The computed values of the dissipation rates are used to estimate the length and time scale pertaining to the dynamics of the small scales, namely the Kolmogorov and Taylor scales $\eta_k = (\nu^3/\varepsilon_S)^{1/4}$ and $\tau_k = (\nu/\varepsilon_S)^{1/2}$. We choose to use our estimation of the viscous dissipation rate ε_S to compute these scales because this quantity is exclusively linked to the small scale dynamics, In this case, no production of TKE by the mean flow. whereas the temporal decay rate ε_T includes the contribution of the large scales. The discrepancy affects the estimation of the Kolmogorov scale, due to its dependence on $\sim \varepsilon_S^{-1/4}$. Hence an underestimation on ε_S of say 50% will lead to an overestimation of the Kolmogorov length scale of only 20%.

The integral length scale gives a spatial scale of the largest eddies. In our experiments, it is defined as integration of the longitudinal spatial correlation coefficient over the measured spatial separations smaller than the visualization field span D_{max} . Example of the computed longitudinal $f_i(r) = \frac{\langle u_{t,i}(\vec{x}) \cdot u_{t,i}(\vec{x} + r \cdot \vec{e}_i) \rangle_T}{\langle u_{t,i}^2 \rangle_T}$ and transverse $g_i(r) = \frac{\langle u_{t,i}(\vec{x}) \cdot u_{t,i}(\vec{x} + r \cdot \vec{e}_j) \rangle_T}{\langle u_{t,i}^2 \rangle_T}$ correlation coefficients, for each velocity component i are shown in *figure 3.4*. The resulting integral scales $L_{f_i} = \int_0^{D_{max}} f_i(r) dr$ are depicted in *figure 3.5*. The integral scales are shown to be close to the grid mesh size and to vary very slowly with the decay.

Finally the Taylor length scales of the flow have been computed from both the velocity components gradients $\lambda_i = \sqrt{2 \langle u_{t,i}^2 \rangle / \langle (\partial u_{t,i} / \partial x_i)^2 \rangle}$ and the spatial average of viscous dissipation rate $\lambda_\varepsilon = \sqrt{30 \nu u_{t,1}^2 / \varepsilon_S}$ (*figure 3.6*). The resulting values are found to be close (around 1cm) and slowly varying with the decay.

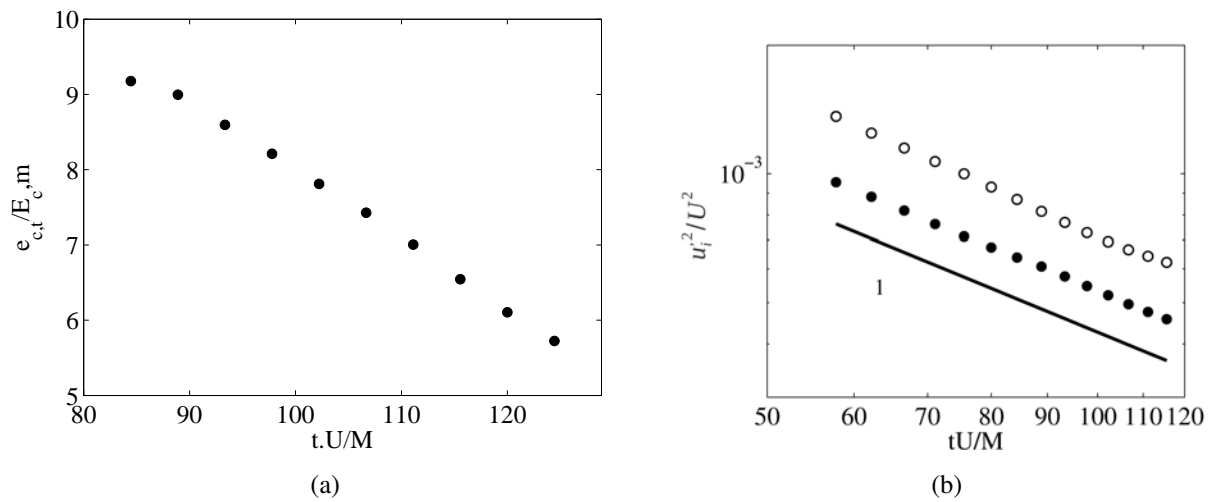


Figure 3.2: *a)* Ratio of turbulent motion to mean motion kinetic energies *b)* Decay of the turbulent components energies $\circ \langle u_1^2 \rangle_S / U^2$, $\bullet \langle u_2^2 \rangle_S / U^2$.

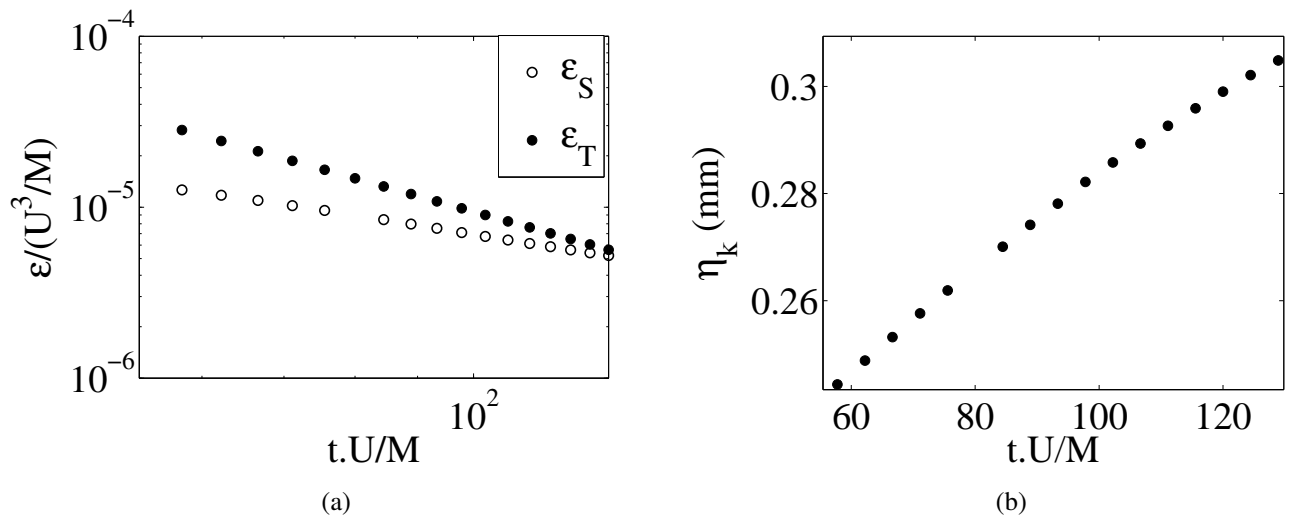


Figure 3.3: *a)* \circ Viscous dissipation $\varepsilon_S/(U^3/M)$, \bullet Decay rate of the turbulent kinetic energy $\varepsilon_T/(U^3/M)$, *b)* Kolmogorov Length scale.

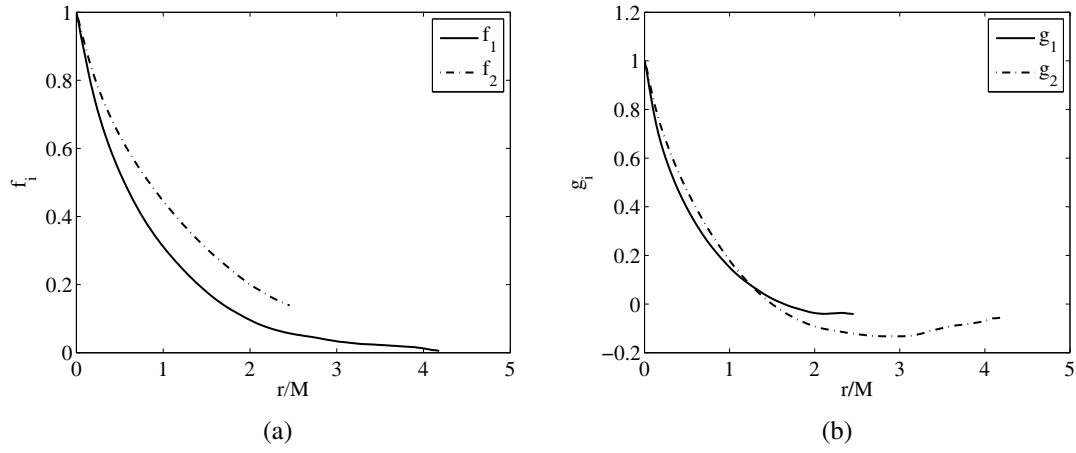


Figure 3.4: longitudinal f_i and transverse g_i correlation coefficients, for each velocity component i at $t.U/M = 84.4$.

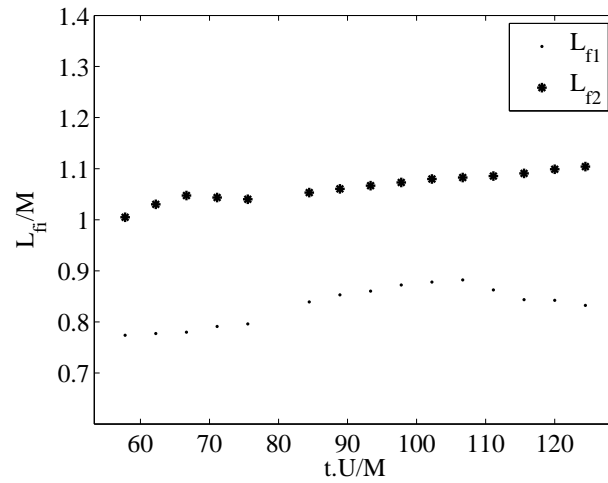


Figure 3.5: Evolution with time of the normalized integral scales L_{fi}/M .

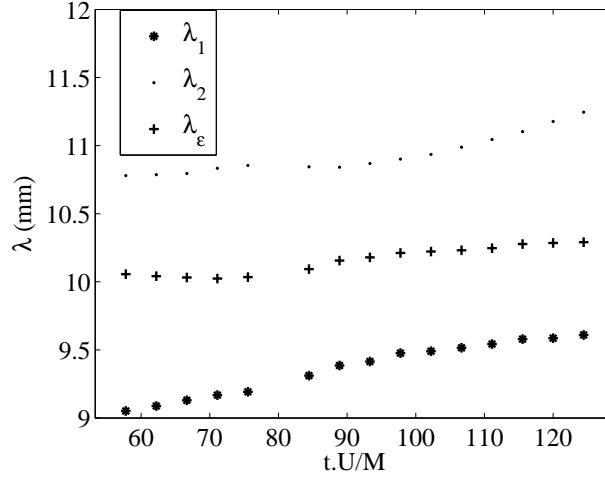


Figure 3.6: Variation of the Taylor scales associated with each of the computed velocity gradient : $\lambda_i = \sqrt{2 u_{t,i}^2 / (\partial u_{t,i} / \partial x_i)^2}$, and the Taylor scale deduced from the viscous dissipation $\lambda_\varepsilon = \sqrt{30\nu u_{t,1}^2 / \varepsilon_S}$.

3.3 Small scales dynamics

3.3.1 Velocity gradients statistics

Computation of velocity gradients First we describe briefly the method used to estimate the velocity gradients from the measured PIV velocity fields. Primarily it is worth recalling the bias pertaining to the computation of those gradients: first the noise associated to velocity measurements, which is amplified when computing associated spatial derivatives. Second the spatial resolution of the measurements which sets the accuracy of velocity gradients computations. And finally the oversampling of PIV interrogation, i.e. the 50% interrogation windows overlapping in our case.

The gradient is computed as the ratio of velocity difference to the spacing between two close points of the measurement grid : $\delta u / \delta x$ with δx sufficiently small, thus the noise related to the velocity gradients $\varepsilon_{\delta u}$ is increased in comparison with the noise related to the velocity measurements ε_u since $\varepsilon_{\delta u} \sim \varepsilon_u / \delta x$. Additionally, the minimum spacing δx is determined by the size of the interrogation window B which sets the spatial resolution of our measurements: a poor spatial resolution may lead to an underestimation of the velocity gradients.

To estimate the velocity gradients from our measurements, we compute the differences of velocity issued from close but non overlapping interrogation windows. This insures the fact that the two velocity measurements are weakly correlated, i.e. are not issued from measurements that share the same tracers (Raffel et al. 1998):

$$\frac{\partial u_{t,i}}{\partial x_1}(x_1, x_2) = \frac{u_{t,i}(x_1 + \delta x, x_2) - u_{t,i}(x_1 - \delta x, x_2)}{\delta x}, \quad \text{where } \delta x = B/2$$

What we actually compute is proportional to velocity differences with the second smallest possible separation permitted by the spatial resolution of our measurements. However, in the following we will show that this estimation, albeit its roughness, leads to results in relatively good agreement with other results issued from more accurate experimental and numerical studies and theoretical predictions, which will lead us to assume that our computations are good estimation of actual velocity gradients. We will then use those values to estimate other differential quantities pertaining to the turbulent flow, chiefly the viscous dissipation rate.

In *figure 3.7*, the longitudinal and transverse velocity gradients PDF are shown at $t.U/M = 84.4$; the values of the PDF are issued from all the turbulent velocities measured at this stage of the decay from 500 independent realizations, so the number of velocity measurements used for each PDF is 7.310^6 . The measurements can not obviously all be considered as statistically independent, since the velocities in a turbulent field remain strongly correlated at separations of the order of the integral length scale.

Local isotropy First we check the local isotropy of the generated turbulence: the first Kolmogorov hypothesis states that for sufficiently large Reynolds numbers, the local isotropy related condition of invariance under rotation of the two points joint velocity statistics at small separations induce that the longitudinal (or transverse) velocity gradients issued from the two velocity components should have similar PDFs¹. As shown in *figure3.7* $\partial u_{t,1}/\partial x_1$ and $\partial u_{t,2}/\partial x_2$ collapse on the top of each other, so are the PDF of $\partial u_{t,1}/\partial x_2$ and $\partial u_{t,2}/\partial x_1$. Since for example $\partial u_{t,1}/\partial x_1$ and $\partial u_{t,2}/\partial x_2$ can be deduced from each other by a rotation of 90° , this illustrate the high degree of isotropy of the small scales (local isotropy) achieved in our experiment, despite the observed large scale anisotropy and inhomogeneity.

1. The fluid velocity gradients PDFs have been compared to the turbulent velocity gradients PDF and have been shown to collapse at the top of each others. Thus one expect the total and turbulent velocity gradients statistical moments to be close. Besides, this may also confirm the local homogeneity of the generated turbulence.

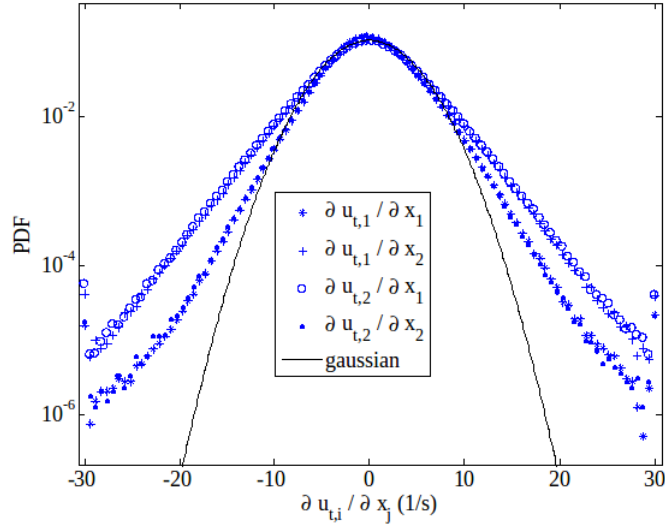


Figure 3.7: Turbulent velocity gradients PDFs at time $t.U/M = 84.4$, the continuous line represents a Gaussian distribution.

On the other hand, the transverse and longitudinal gradients PDFs are not similar, seemingly due to a larger dispersion around the mean of the values of the transverse gradients; this stems from the relationship between longitudinal and transversal structure functions, under the conditions of local isotropy and non-compressibility of the fluid, which states that transverse structure function is always larger than longitudinal one for the small to intermediate scales comprised in the inertial sub-range. More precisely, for separations comprised in the dissipative range, the predicted ratio is 2, while for the inertial sub-range, the ratio is $4/3$. In our measurements, however the separation between velocity vectors used for gradient computations is roughly 10 times larger than the Kolmogorov length scale, and thus the theoretical ratio of 2 is not exactly matched by our velocity gradients estimations. This is shown in *figure 3.9*, where the ratios $2 (\partial u_{t,i} / \partial x_i)^2 / (\partial u_{t,i} / \partial x_j)^2$, expected to be equal to 1 have been computed through the decay. In this figure, it is also shown that the value of the ratio varies relatively slowly with the decay (from 1.4 to 1.3 in $200.M/U$).

Intermittency The normalization of gradients values by their respective standard deviation $\sigma (\partial u_{t,i} / \partial x_j)$ leads to the superposition of their respective PDFs, as shown in *figure 3.8*, except for the right tails: the normalized gradients PDF seems to be slightly more skewed towards negative values, whereas the transverse velocity gradient PDF shows a remarkable symmetry (Sreenivasan & Antonia 1997 ; Yaglom & Monin 1975). The normalized and non-

normalized PDFs have been both compared to a normal distribution with the same means and variances, and large deviations in the tails are observed in comparison to the normal distribution: the turbulent velocity gradient PDFs seems to have a higher “peakiness”.

The departure from Gaussianity is a signature of turbulence *intermittency*: the form of the velocity gradients PDFs suggest that the probability for nearly zero and very large values are higher than predicted by a normal distribution, while the probability of moderate values is smaller. Such distributions are encountered in “bursting” signals, where long periods of nearly zero values alternate with short periods of high values of the signal. The observed intermittency thus translates the fact that velocity derivatives related quantities, such as viscous dissipation rate and vorticity, are highly localized in space: for example one expect that, although the flow kinetic energy may be distributed rather uniformly, i.e. with moderate deviations from the spatial average, its dissipation rate is conversely mainly concentrated on some regions of the flow, where most of the dissipation occurs. This induces a contradiction with the K41 theory, as pointed out first by Landau & Lifshitz (1987). Refinement of the K41 theory have been performed, based on the assumption that the dissipation is log-normally distributed, hence mean square velocity gradients are also log-normally distributed (Kolmogorov 1962).

In order to quantify the degree of intermittency of the velocity gradients throughout the decay we need to quantify the degree of departure from a Gaussian distribution. Thus we compute the skewness of the distribution and its flatness, at different stages of the decay. In a freely decaying, homogeneous and isotropic turbulence, the velocity gradient skewness is related to the production term of enstrophy by the strain field. The enstrophy is produced by the strain field and dissipated by viscous effects, and for the term related to the strain field to be positive, the velocity gradients skewness should be negative (Yaglom & Monin 1975 ; Davidson 2004 ; Townsend 1980).

As shown in *figure 3.10* the skewness of longitudinal velocity gradients is negative as expected, and has a value of around -0.15 , while the skewness of the transverse velocity gradients is roughly ten times smaller. The skewness seems not to vary significantly with the decay, but rather oscillates around a value for each case, with no clear tendency. The velocity gradients skewness is lower than previously reported values in the case of wind tunnel grid turbulence, which is -0.4 (Wyngaard 1970); these data have been issued from different measurements in laboratory and natural flow, performed with a sufficient resolution to accu-

rately estimate velocity derivatives². In contrast our values involve only spatial increments of the filtered fluid velocity field, due to the limited resolution of our measurements. This may explain the observed discrepancy with literature's results.

The velocity gradients flatness seems to decay slightly from 5.5 to 4.5 as shown in *figure 3.11*; this may be due to the fact that the Reynolds number or the turbulence strength decreases with the decay, leading to a lesser intermittency of the turbulent flow. Indeed as the TKE decay, the Reynolds number based on the mesh grid decreases from 1350 to 900. Nevertheless, the values of the velocity gradient flatness are in better agreement with the literature (Van Atta & Antonia 1980).

Exponential tails Finally, it is worth noticing that the tails of the PDF seems to stretch along straight lines in semi-log plot, showing that they may be approximated by an exponential distribution, whereas the PDF core is more likely to be approximated by a Gaussian, in agreement with some previous studies (Kida & Murakami 1989; Tabeling et al. 1996; Shafi et al. 1997). For sufficiently large values of normalized velocity gradients, the PDF fits the function: $P(\xi_{ij}) \sim \exp(-\beta_{ij}\xi_{ij})$, where $\xi_{ij} = (\partial u_{t,i}/\partial x_j)/\sqrt{(\partial u_{t,i}/\partial x_j)^2}$ are normalized velocity gradients and β_{ij}^{\pm} are related exponential PDF decay rate. As shown in *figure 3.12* and *figure 3.13*, this function seems to fit well the tails of both longitudinal and transverse gradients PDFs. We shall stress the difference between the decay rate of the right tails β_{ij}^+ and the left tails β_{ij}^- .

For all the considered stages of the decay, the two decays rates are found to differ for longitudinal velocity gradients, this fact translate the previously observed skewness of the related PDF. On the other hand, the two decay rates remain close for transversal gradients, as expected from the observed symmetry of the corresponding PDF. The values of decay rates are almost constant over the decay and are found to be close to 2 in absolute value, which in good agreement with results of Kida & Murakami (1989) for instance. It can be easily demonstrated that the exponential shape of the PDF at large values leads to the fact that of moments of successive order increases linearly with the order, as shown by Kida & Murakami (1989) and Frenkiel & Klebanoff (1971) .

2. Some authors (*Wyngaard*) have inferred velocity spatial derivatives from the temporal ones, using the frozen turbulence hypothesis, the used hot wire anemometer cut off frequencies were of the order of the Kolmogorov time scales. Others (*Shafi*) have used spatially close HWA to measure directly spatial derivatives.

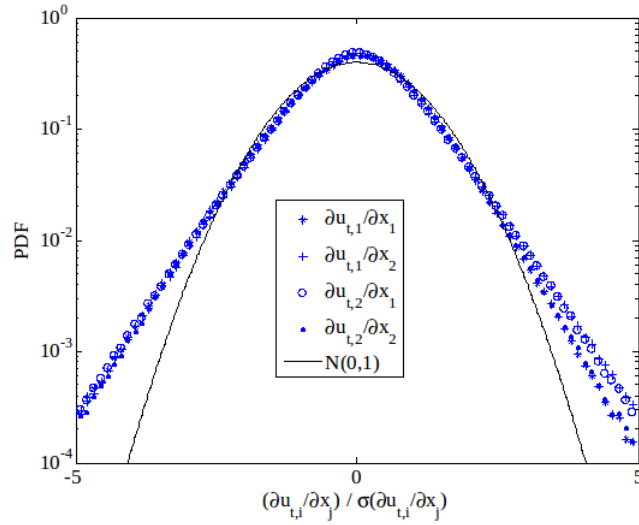


Figure 3.8: Normalized turbulent velocity gradients P.D.F at time $t.U/M = 84.4$; comparison with a normal distribution of mean 0 and standard deviation 1 (continuous line). Large deviations of the PDFs tails for the Gaussian distribution are noticed, which is a signature of turbulence intermittency.

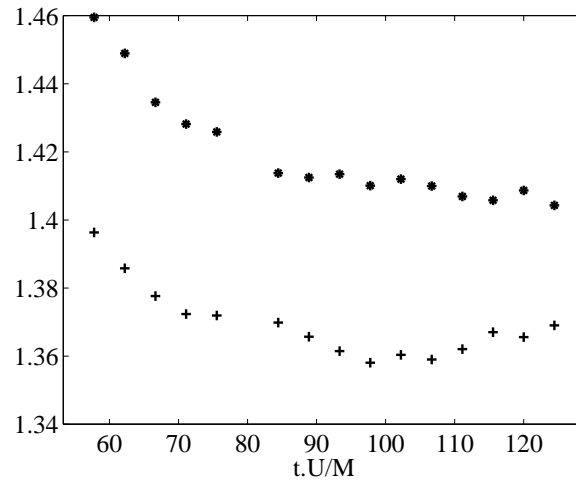


Figure 3.9: Ratios of longitudinal to transverse velocity gradients at different stages of the decay : (*) $2 (\partial u_{t,1}/\partial x_1)^2 / (\partial u_{t,1}/\partial x_2)^2$, (+) $2 (\partial u_{t,2}/\partial x_2)^2 / (\partial u_{t,2}/\partial x_1)^2$. The mass conservation and local isotropy imposes a value of 1 for the two ratios, but the computed values are significantly higher.

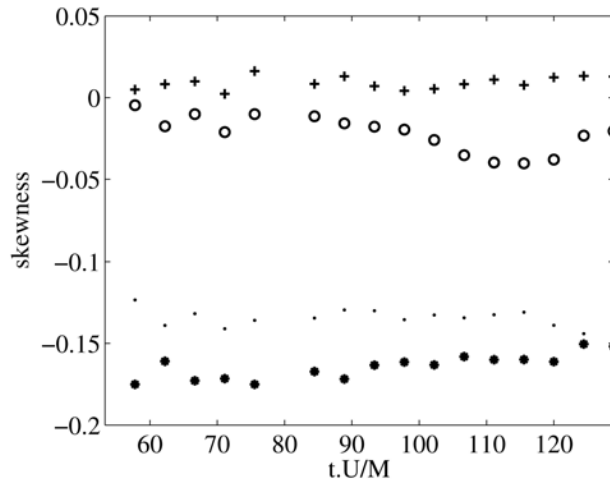


Figure 3.10: Evolution of the velocity gradients skewness $(\partial u_{t,i}/\partial x_j)^3 / (\partial u_{t,i}/\partial x_j)^2 \cdot 3/2$ with the decay. The two longitudinal velocity gradients have negative skewness. for legend see *figure3.8*.

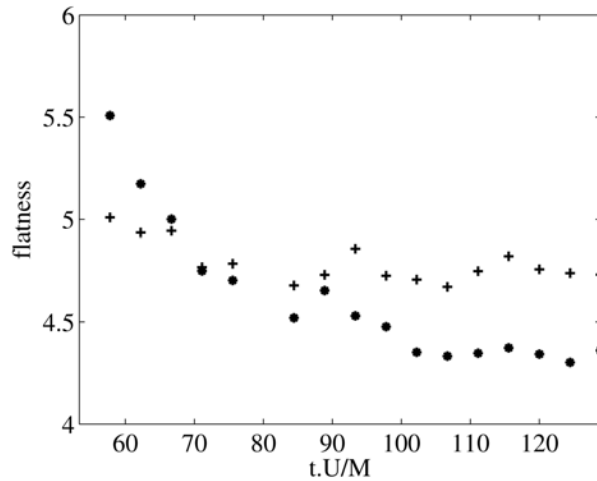


Figure 3.11: Velocity gradients flatness throughout the decay. No clear tendency is noticed. The values are all larger than 3, the flatness of a normal distribution, hence confirming the observed intermittency.. For legend see *figure3.8*.

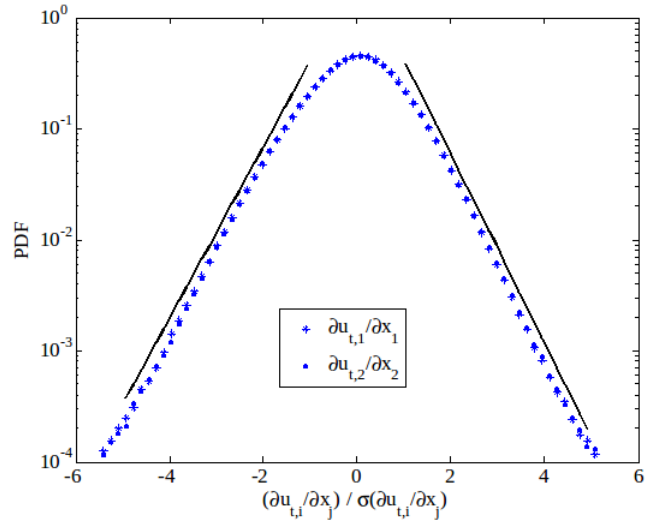


Figure 3.12: Longitudinal velocity gradients exponential tails at $t.U/M=84.4$; each tail of the PDF is compared to an exponential distribution $P(x) = \exp(-\beta x)$, where β is the exponential decay rate. The right tail exponent decay rate is larger than the left tail decay rate, translating the previously noticed skewness of the PDF toward negative values.

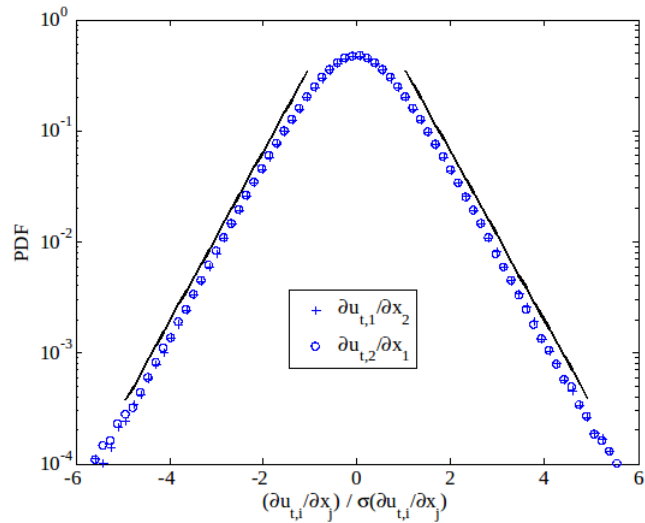


Figure 3.13: Transverse velocity gradients exponential tails at $t.U/M = 84.4$; The two computed tails exponential decay rates are similar, as expected from the observed symmetry of the PDF.

3.3.2 Velocity differences statistics

The previous subsection was devoted to the estimation of the turbulent flow velocity gradients which are related to the dynamics of the smallest eddies of the turbulence, responsible for most of the dissipation. In this section we are interested in the distribution of turbulent kinetic energy across the whole spectrum of eddy sizes and the inter-scales energy flux. Additionally we will verify the degrees of independence between large and small scale motion, by both checking the flow isotropy at scales included in the universal equilibrium range, and assessing the extend of the inertial sub-range.

The distribution of the energy across eddies and energy exchange between different eddies is often characterized by the energy spectra. This may be otherwise achieved in the real space, by considering the velocity structure functions. The statistics of velocity differences at a separation r may be used to characterize the dynamics of eddies of size r since the mean kinetic energy at scales r or less is of the order of the second order longitudinal structure function $D_{L,i}(r) = (u_{t,i}(\vec{x} + r\vec{x}_i) - u_{t,i}(\vec{x}))^2$ (the transverse structure function is $D_{N,i}(r) = (u_{t,i}(\vec{x} + r\vec{x}_j) - u_{t,i}(\vec{x}))^2$), but is dominated by the contribution from eddies of larger size r .

The intermediate eddies of the energy cascade are responsible of transferring the energy from the large energy containing eddies to the small dissipative eddies. Their dynamics may be characterized using statistical moments of the velocity differences at a given separation r included in the inertial sub-range. From similarity hypothesis, and considering the spatial average of dissipation over the whole fluid flow, Kolmogorov derived a simple power-law relationships for structure functions for separations r comprised in the inertial sub range; the structure function is expected to behave theoretically as: $D_{L,i}(r) \approx C(\epsilon r)^{2/3}$, $D_{N,i}(r) \approx C(\epsilon r)^{2/3}$. Where the constants $C \approx 2$ and $C = (4/3)C$ are universal, i.e. independent from the nature and the turbulent flow and its Reynolds number.

Now let's consider a scale of velocity u_r for separation r , the characteristic time of the decay of eddies of size r is then r/u_r thus the decay rate of energy for this eddy size is $u_r^2/(r/u_r) = u_r^3/r$. Since the dissipation rate is the same for all eddies included in the quasi-equilibrium range and equal to the viscous dissipation rate $u_r^3/r \sim \epsilon$, one then may assume $u_r^3 \sim (u_{t,i}(\vec{x} + r\vec{x}_i) - u_{t,i}(\vec{x}))^3$ so $(u_{t,i}(\vec{x} + r\vec{x}_i) - u_{t,i}(\vec{x}))^3 \sim \epsilon r$ which leads to the con-

stancy of the velocity differences skewness:

$$S_i(r) = (u_{t,i}(\vec{x} + r.\vec{x}_i) - u_{t,i}(\vec{x}))^3 / (u_{t,i}(\vec{x} + r.\vec{x}_i) - u_{t,i}(\vec{x}))^2 \cdot 3/2 = cte$$

Thus the equilibrium hypothesis leads to the conclusion of independence of the velocity difference skewness is independent from the separation across the inertial sub range, and from similarity hypothesis it can be shown that $S_1(r) = -(4/5)C^{-3/2} \approx 0.3^3$.

The large scales anisotropy and inhomogeneity have been shown to influence sensibly the small scales, even for high Reynolds number flows, where a large scale separation occurs (Ouellette et al. 2006). This obviously is in disagreement with the K41 theory hypothesis which states the independence of small and large scale motion when Reynolds number tend to infinity. In our case, since the Reynolds number of our flow is moderate, the independence between large and small scale motion is less expected than in the above cited study, we predict a limited extension of the inertial range (although as it will be recalled further, a precise criteria for quantifying this extend is hard to set in our case) and a relative local anisotropy due to the expected interaction of small and large scales.

In the previous section, the small scale isotropy has been assessed by the estimation of the “velocity gradients”, in the following we check the local isotropy for larger separations. If the turbulence is locally isotropic the two components longitudinal (or transverse) structure functions should be equal $D_{L,1} = D_{L,2}$, $D_{N,1} = D_{N,2}$; thus a comparison at the time $t.U/M = 84.4$ of the decay is made for longitudinal structure function and transverse structure function in *figure 3.14*. At this time, the flow Reynolds number based on the Taylor scale is estimated at 250. The two components longitudinal structure functions are equal up to separations of the order of the mesh grid (equivalent to the integral length), for this range, the value of the ratio between the two lies between 1 and 1.05, confirming the local isotropy assumption for those scales of the turbulence. On the other hand, for transverse structure function however, the values for the two components begin to diverge earlier. The observed isotropy of the small-scales persists until $t.U/M = 146.6$, then anisotropy began to appear in form of a larger discrepancy between the two longitudinal structure functions. This anisotropy is thought to be due to the lesser strength of the turbulence motion in comparison with the highly anisotropic mean motion at those decay stages.

The transverse structure function shows hence a reduced range of scales where the small

3. The exposed reasoning is used by Davidson (2004) and is rather simplistic. For rigorous exposition and demonstration of the above scaling see Yaglom & Monin (1975) and Davidson (2004).

scales isotropy is verified, in comparison with the longitudinal structure function. This has been observed by Arad et al. (1998) in the case of atmospheric boundary layer turbulence where the effect of large scale flow anisotropy is shown to be weak on the longitudinal structure function while significant on the transverse structure function. As proved earlier, the turbulent motion in our case shows also a certain anisotropy, thus this large scale anisotropy is then expected to induce the observed small scale anisotropy.

For a similar flow configuration, Sreenivasan & Dhruva (1998) and Dhruva et al. (1997) suggests that the mean shear may be the cause of the observed local anisotropy. Similar conclusions have been drawn from DNS made by Pumir & Shraiman (1995) where a violation of the small-scales isotropy has been observed for a homogeneous shear flow. In our case however, the mean shear although it exists, as it can be shown from the inspection of a mean velocity field, is expected to be weak and thus its influence on the small scales is not expected to be significant. The mean shear relates more generally to the flow inhomogeneity, and its effect on small-scales has been recently investigated by Blum et al. (2010) in a flow configuration close to ours, where the turbulence is generated by an oscillating grid in a water tank. The turbulence is shown to be highly inhomogeneous near the grid and more homogeneous at the center of the tank. The structure function was conditioned by the local large scale flow, and has been shown to depend sensibly on the value of the large scale velocity.

In conclusion, we believe that the flow inhomogeneity and thus the related mean flow anisotropy is chiefly responsible for the observed anisotropy of the small scales for transverse structure function, due to the fact that the mean flow gradient is mainly in the transverse direction $\partial U_{m,2}/\partial x_1$. For higher separations, the two component's structure function differs noticeably, translating the expected large scale anisotropy. We also notice that the second component structure function is always larger than the first, and this may be explained by the fact that the energy is also always larger for the former component.

The range of scale at which the local isotropy seems to be verified may define both the inertial and dissipative sub-ranges of the present turbulent flow. The value of the structure functions with separations belonging to the inertial range are expected to follow the two-thirds law. Since there is no systematic method at our disposal to set the limits of this range, we rather check which "portion" of the structure function fits well the two-thirds law as displayed in *figure 3.14*, this portion extends to less than a decade, with the noticeable exception of the transverse structure function along the second velocity component, which does not seem to follow the two-thirds law for any ranges of separations. Thus we conclude that of this

stage of the decay, the inertial range extend from $r \approx \lambda$ to 4λ . For this range we check the relation $D_{N,1}/D_{L,1} = 4/3$, which is a consequence of the similarity hypotheses and mass conservation, and the computed ratio lies between 1.2 and 1.36.

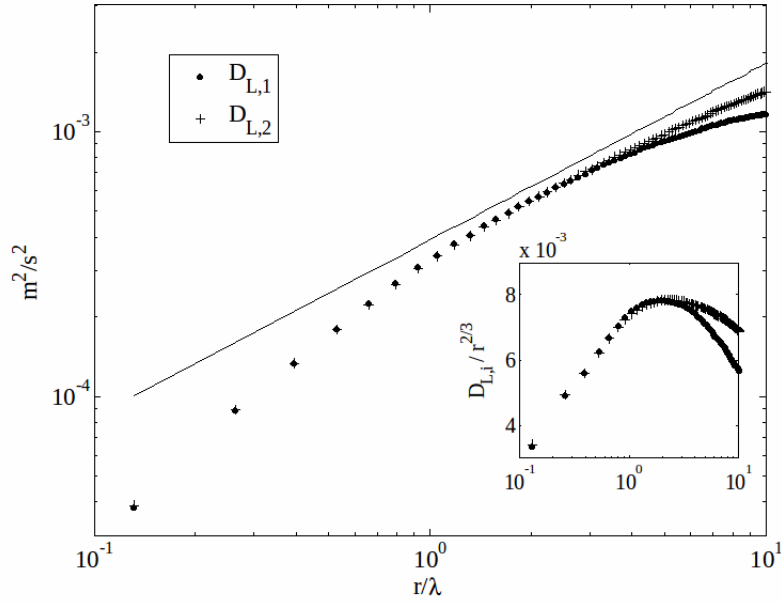
Do the conclusions made for this particular stage hold for other stages at the beginning of the decay? To answer this question we compare the normalized form of the structure function $C_1 = D(r) (\varepsilon r)^{-2/3}$ at three stages of the decay in *figure 3.15*. One first observes that for any stage the value of the Kolmogorov coefficient seems not to be constant but rather varies noticeably with the decay, in contradiction with the expected universality of this coefficient. The value for the beginning of the decay seems to be closer to the theoretical value of 2, which may also suggest that the small scales dynamics may not show a good similarity throughout the decay. Besides, The size of the inertial sub range, defined by the separations comprised in the function plateau, seems not to change significantly from different stages of the decay, although we expect that the size of the inertial range to decrease, since the Reynolds number is decreasing.

Finally we turn attention to the skewness of the velocity differences for the whole range of separations. As noted previously in the introduction, the skewness is expected to be constant in the inertial sub range since the dissipation rate is the same for every eddy size. As depicted in *figure 3.16* for three different stages of the decay 0.3.

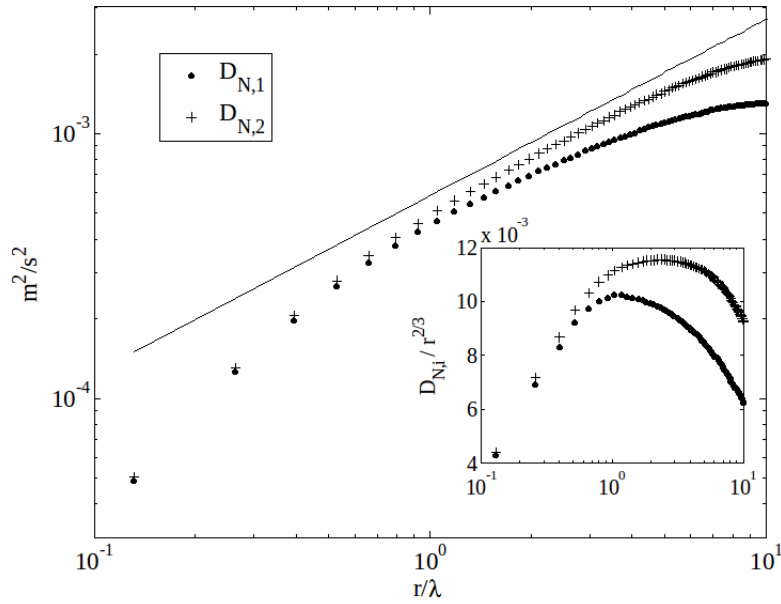
3.4 Conclusions

In this chapter, the generated turbulence have been characterized using a standard PIV technique. The most important feature of our experimental set-up is to generate an homogeneous and isotropic turbulence with weak mean flow. Those features, pertaining mainly to the large scale motion, have been thus investigated first. The departure of the turbulent velocity field from the isotropy and homogeneity have been found to be small, suggesting that the used turbulence apparatus is well suited for the study of isotropic turbulence.

However, a non negligible mean motion have been observed and found to be highly anisotropic and inhomogeneous, but weaker than the turbulent motion. This mean motion is structured



(a)



(b)

Figure 3.14: *a*) Longitudinal second order structure function $D_{L,i}(r) = \langle (\vec{u}_{t,i}(\vec{x}) - \vec{u}_{t,i}(\vec{x} + r.\vec{x}_i))^2 \rangle$ at $t.U/M = 84.4$. The separation is normalized by the Taylor scale λ (computed from ε_s). The two structure functions values are close up to separations of the order of $r \approx 4\lambda$, suggesting the local isotropy for this range of separations. Besides, $D_{L,i}$ are shown to fit the two-thirds law for the range of separations $r \approx \lambda - 4\lambda$, which may then define the inertial sub-range. Inset: the “compensated” structure functions. *b*) Transversal second order structure function $D_{N,i}(r) = \langle (\vec{u}_{t,i}(\vec{x}) - \vec{u}_{t,i}(\vec{x} + r.\vec{x}_j))^2 \rangle$ at time $t.U/M = 84.4$. The values of the two structure functions differs earlier than for longitudinal functions.

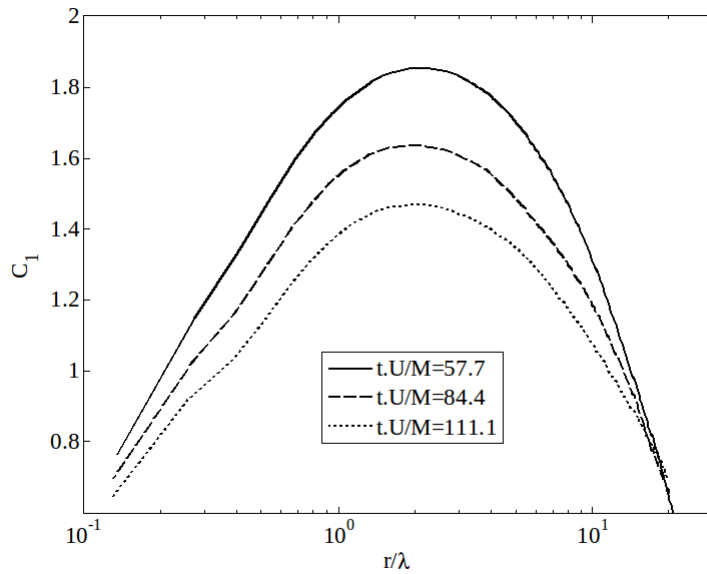


Figure 3.15: Comparison of the Kolmogorov coefficient $C_1 = D(r) (\epsilon r)^{-2/3}$ at different stages of the decay.

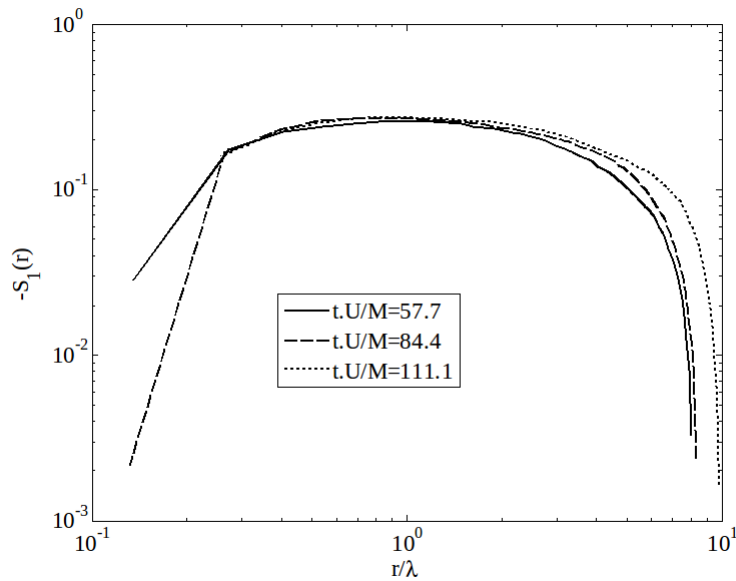


Figure 3.16: The first velocity component longitudinal velocity differences skewness at three different stages of the decay. For every stage, the skewness is fairly constant for separations from 0.3λ to 2λ . Noticeable is the fact that for the smallest measured separation is sensibly outside the inertial range, since the corresponding absolute value of the skewness is smaller than 0.3.

into vertical “streak like” structures which may be related to the moving grid wake; interestingly, the “vortex like” structure of the mean flow reported in previous studies have not been observed in our experiments. The mean flow is shown to be however weaker than the turbulent motion.

Then the focus was made on the small scales dynamics of the generated turbulent flow, which are of primary importance with regard to the local difference between particles and surrounding fluid, since this difference is thought to be mainly governed by these small scales. Due to the limited spatial resolution of our measurements, the whole range of the dissipative scales cannot be resolved, and so are the velocity gradients and related statistics such as the viscous dissipation rate; the computed values of these quantities are only rough estimations. Conversely, the spatial resolution of our measurements is sufficient to resolve the dynamics of eddies belonging to the inertial sub-range.

The small scales dynamics are investigated through both the computation of velocity gradients and velocity differences for a range of separations. First, the velocity gradients statistics are investigated in order to illustrate important notions pertaining to turbulence theory, namely the intermittency and the local isotropy.

The velocity differences statistics gives a more precise account for the small and intermediate scales dynamics: our results confirm the local isotropy of the flow for the smallest measured scales; although a slight anisotropy is observed for the inertial scales, which is thought to be related to the anisotropy of the mean motion. More importantly, a clear inertial sub-range of separations, following the classical Kolmogorov two thirds law, is observed.

3.5 References

Arad, I. et al., 1998. Extraction of Anisotropic Contributions in Turbulent Flows. *Physical Review Letters*, 81(24), pp.5330-5333.

Adrian, R.J. & Westerweel, J., 2010. Particle Image Velocimetry, Cambridge University Press.

Batchelor, G.K., 1953. *The Theory of Homogeneous Turbulence*, Cambridge University Press.

Bershanskii, A., Kit, E. & Tsinober, A., 1993. On universality of geometrical invariants in turbulence—Experimental results. *Physics of Fluids A: Fluid Dynamics*, 5(7), p.1523.

Blum, D.B. et al., 2010. Effects of nonuniversal large scales on conditional structure functions in turbulence. *Physics of Fluids*, 22(1), p.015107.

Comte-Bellot, G. & Corrsin, S., 1966. The Use of a contraction to improve the isotropy of grid-generated turbulence. *Journal of Fluid Mechanics*, 25(04), p.657-682.

Davidson, P.A., 2004. *Turbulence: An Introduction for Scientists and Engineers*, Oxford University Press, USA.

Dhruva, Brindesh, Tsuji, Y. & Sreenivasan, Katepalli R., 1997. Transverse structure functions in high-Reynolds-number turbulence. *Physical Review E*, 56(5), p.R4928-R4930.

Ertunc, O. et al., 2010. Homogeneity of turbulence generated by static-grid structures. *Journal of Fluid Mechanics*, 654, p.473-500.

Frenkiel, F.N. Statistical properties of velocity derivatives in a turbulent field. *Journal of Fluid Mechanics*, 48(01), pp.183-208.

Grant, H.L. & Nisbet, I.C.T., 1957. The inhomogeneity of grid turbulence. *Journal of Fluid Mechanics*, 2(03), p.263-272.

Kida, S. & Murakami, Y., 1989. Statistics of velocity gradients in turbulence at moderate Reynolds numbers. *Fluid Dynamics Research*, 4(5-6), pp.347-370.

Kolmogorov, A.N., 1962. A Refinement of previous hypotheses concerning the local structure of turbulence in a viscous incompressible fluid at high Reynolds number. *Journal of Fluid Mechanics*, 13(01), pp.82-85.

Landau, L.D. & Lifshitz, E.M., 1987. *Fluid Mechanics, Second Edition: Volume 6* 2nd ed., Butterworth-Heinemann.

McKenna, S.P. & McGillis, W.R., 2004. Observations of flow repeatability and secondary circulation in an oscillating grid-stirred tank. *Physics of Fluids*, 16, p.3499.

Mohamed, M.S. & Larue, J.C., 1990. The decay power law in grid-generated turbulence. *Journal of Fluid Mechanics*, 219(-1), p.195-214.

- Morize, C., 2006. De la turbulence 3D en déclin à la turbulence anisotrope dominée par la rotation. Thesis Université Denis Diderot - Paris VII.
- Ouellette, N.T. et al., 2006. Small-scale anisotropy in Lagrangian turbulence. *New Journal of Physics*, 8(6), pp.102-102.
- Pumir, A. & Shraiman, B.I., 1995. Persistent small scale anisotropy in homogeneous shear flows. *Physical Review Letters*, 75(17), pp.3114-3117.
- Raffel, M., Willert, C.E. & Kompenhans, J., 1998. *Particle image velocimetry: a practical guide*, Springer.
- Shafi, H.S., Zhu, Y. & Antonia, R.A., 1997. Statistics of $\partial u \partial y$ in a turbulent wake. *Fluid Dynamics Research*, 19(3), pp.169-183.
- Sreenivasan, K.R. & Antonia, R.A., 1997. The phenomenology of small-scale turbulence. *Annual Review of Fluid Mechanics*, 29(1), pp.435-472.
- Sreenivasan, K.R. & Dhruva, B., 1998. Is there scaling in high-Reynolds-number turbulence? *Progress of Theoretical Physics Supplement*, pp.103–120.
- Stewart, R.W. & Townsend, A. A., 1951. Similarity and self-preservation in isotropic turbulence. *Philosophical Transactions of the Royal Society of London. Series A, Mathematical and Physical Sciences*, 243(867), pp.359 -386.
- Tabeling, P. et al., 1996. Probability density functions, skewness, and flatness in large Reynolds number turbulence. *Physical Review E*, 53(2), pp.1613-1621.
- Tanaka, T. & Eaton, J.K., 2007. A correction method for measuring turbulence kinetic energy dissipation rate by PIV. *Experiments in Fluids*, 42(6), p.893-902.
- Townsend, Albert Alan, 1980. *The structure of turbulent shear flow*, Cambridge University Press.
- Van Atta, C.W. & Antonia, R.A., 1980. Reynolds number dependence of skewness and flatness factors of turbulent velocity derivatives. *Physics of Fluids*, 23(2), pp.252-257.
- Wyngaard, J.C., 1970. Measurements of the small-scale structure of turbulence at moderate Reynolds numbers. *Physics of Fluids*, 13(8), p.1962.
- Yaglom, A.M. & Monin, A.S., 1975. *Statistical Fluid Mechanics: Mechanics of Turbulence* Dover Ed., Dover Publications Inc.

4 Particle Dynamics

4.1 Overview

The present chapter is dedicated to the characterization of the dynamics of the neutrally buoyant particles suspended in the generated turbulent flow. With the velocimetry set-up previously described, we were able to measure simultaneously the velocity of each particle and the surrounding fluid, and thus to compare the velocity of the two phases locally and globally.

We first compare the particles size and viscous relaxation time to the Kolmogorov length and time scales respectively, for different stages of the decay. As shown in figure 4.1, the particles have a diameter 4 times larger than the Kolmogorov length scale, and a viscous Stokes number larger than 1. We recall that these ratios are to be taken as an estimation since the Kolmogorov scales used here are computed using the estimated values of the viscous dissipation rate $\langle \varepsilon_S \rangle$. However, the important conclusion of this comparison is that the particles are significantly larger than the Kolmogorov scale and have a relaxation time close to the Kolmogorov time scale.

Thus both inertia and finite size effects are expected to influence particles dynamics, and the particles cannot be considered as tracers. The study presented in this chapter is aimed to reveal any effect of particles finite size and inertia on their dynamics.

To that purpose, the results issued from the simultaneous velocity measurements of the available 610 independent two phase flow realizations are exposed. as the statical convergence test shows in *figure 4.2*, the number of detected particles in all the realizations seems sufficient to yield converged second order statistics.

This chapter is organized as follows: first the modification of the turbulent flow by the particles is studied through the comparison of velocity statistics and the decay dynamics to the

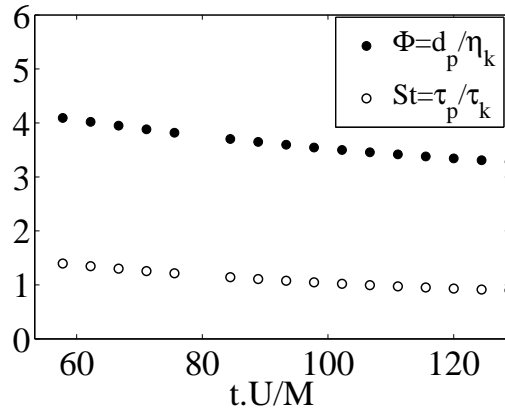


Figure 4.1: Comparison between particle scales and turbulence scales

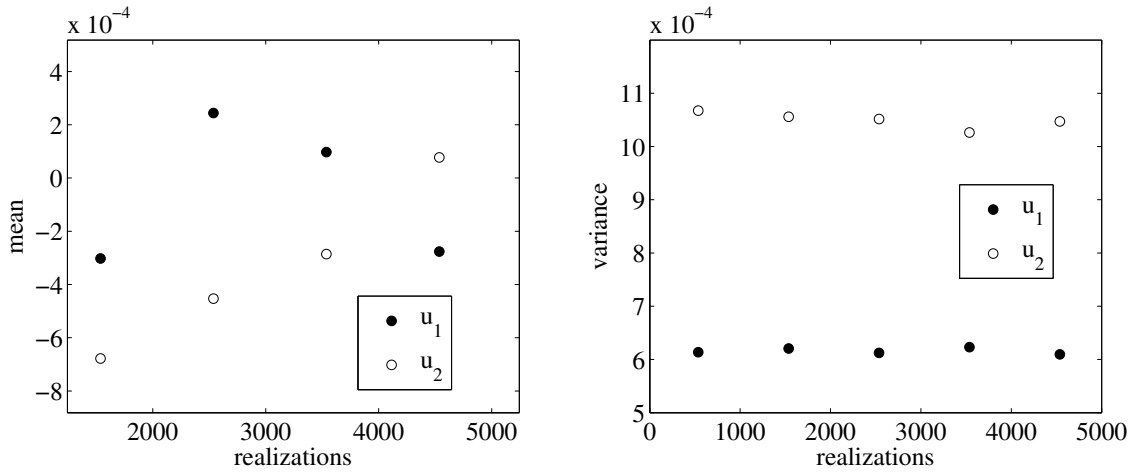


Figure 4.2: Particle velocity convergence tests. The particle velocity variance varies only slightly when the number of involved particles is larger than 1000.

unladen flow dynamics. The comparison will be shown not to be straightforward, due to the modification of the experimental conditions. Next, the velocity statistics of the two phases are compared to each other, in order to reveal any global differences between the two phases dynamics. A slight discrepancy between the mean kinetic energies of the two phases is observed, to which several explanation are suggested. Finally, the local velocity differences between each particle and the surrounding fluid are quantified. This difference is shown to be statistically significant, and several possible explanations are discussed.

4.2 Turbulence modification

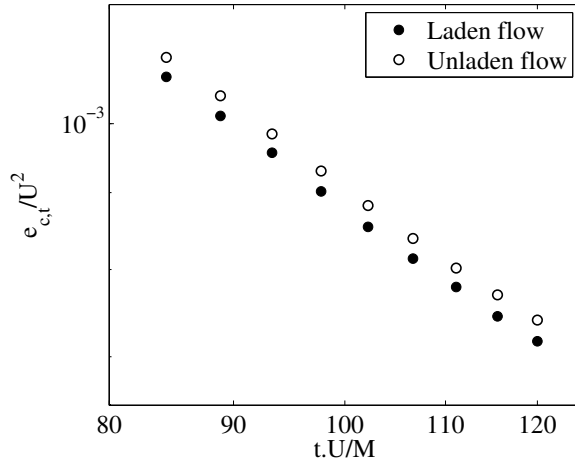
Even though the mass loading of particles is small, the turbulence may slightly be modified by their presence. The aim of this section is to quantify this modification.

The influence of particles on carrier turbulence may result in several possible modifications of the fluid flow: The turbulent kinetic energy (TKE) may be damped or enhanced, and its decay dynamics may be modified, both of these effects are investigated. Additionally, inertial particles have been shown to modify the turbulent energy spectrum of the carrier turbulence (Boivin et al. 1998). In this section we are going to study the modification of turbulence velocity statistics and decay rate. However, the spectrum modulation will not be studied.

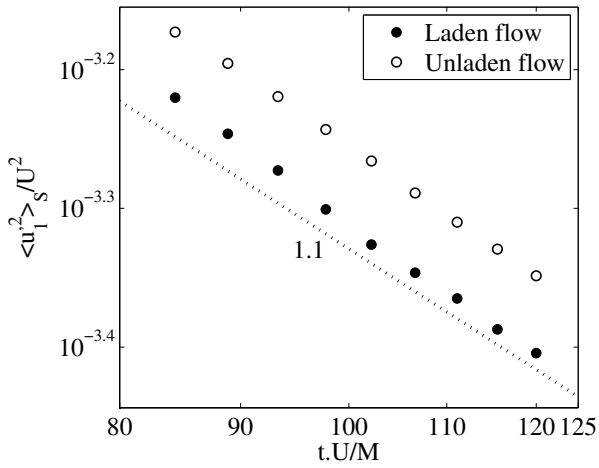
First of all, the focus is made on the modification of the TKE after the addition of particles to the flow. As depicted in *figure 4.3* the total TKE $e_{c,t} = \frac{1}{2} \langle (2u_1^2 + u_2^2) \rangle$ shows a slight diminution of less than 3% between the laden and unladen flows, this quantity is then considered to be fairly unchanged. However, the inspection of the TKE for each velocity component separately shows higher differences between the laden and unladen flows: a decrease of 10% to 13% for the first component and an enhancement between 8% and 13% for the second component.

This variation may be primarily due to the modification of experimental conditions, specifically the change of grid position, since the grid has been removed and put-back between the two measurements. This introduces a different inclination of the grid (the grid is not perfectly horizontal). A visual inspection of the generated mean velocity field before and after grid removal shows a different spatial configuration, suggesting a modification of the mean flow due to the change of the grid position. The modification of the mean motion may lead to a modification of the distribution of the flow energy between the two measured components.

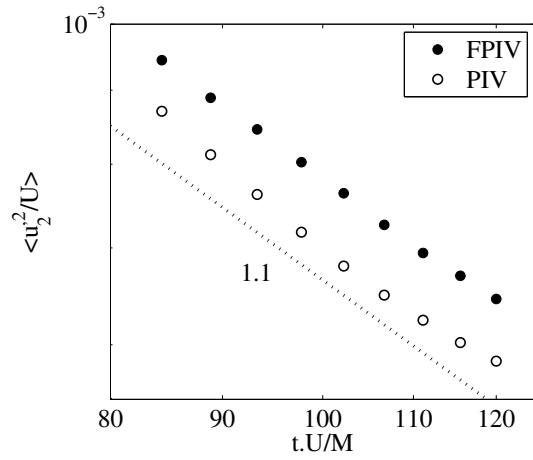
Despite the observed modification of the values of TKE in separate directions, the results suggest that the decay rates of the TKE are fairly unchanged between the laden and unladen cases. This suggests that the viscous dissipation, and thus the velocity gradients statistics, are unaffected by the particles' presence. This leads us to conclude the modification of the turbulence by the particles is weak.



(a)



(b)



(c)

Figure 4.3: Decay of the turbulent kinetic energy, comparison between single-phase flow (\circ) and two-phase flow (\bullet). The turbulent kinetic energies and their decay rates remain close.

4.3 Velocity and position statistics

In this section the velocity statistics of the two phases, issued from the simultaneous velocimetry measurements, are compared. The aim is to reveal global and statistically significant differences between the dynamics of the two phases, prior to the investigation of the local velocity differences. The PDFs of the particle and the fluid velocities are first compared and the degree of homogeneity of the spatial distribution of the particles in the flow field is quantified. Then the mean kinetic energies of the two phases are compared throughout the decay.

It should be noted that for the fluid phase, the focus is both on the local fluid velocity \vec{u}_{fp} at the closest position to the particles and the non-local fluid velocities \vec{u}_f , i.e not conditioned by particles presence. The two phases local velocity differences are quantified by comparing the velocity of each particle \vec{u}_p to the closest measured fluid velocity \vec{u}_{fp} . These different vectors are represented in *figure4.4*

The maximal distance between a particle and the nearest fluid velocity vector is $B/2 = 1.32 \text{ mm}$, this separation is of the order of the particle's diameter; which is equivalent to 4 to 5 Kolmogorov scales. We then avoid the use of interpolation of the fluid velocity at the position of the particle, which may induce an error on the computed velocity difference. In addition, the concept of fluid velocity at the position of the particle is not straightforward to understand physically (since obviously the fluid is not present in the volume occupied by the particles). On the other hand, a linear interpolation scheme has been successfully used by Ouellette et al. (2008), where the error induced by the interpolation was rigorously quantified and shown to be statistically negligible in comparison with the measured fluid-particles velocity differences.

4.3.1 Results

Velocity statistics: We first compare the particle velocity \vec{u}_p to the fluid velocity at particles position \vec{u}_{fp} and overall fluid velocity \vec{u}_f P.D.Fs at two different stages of the decay: $t.U/M = 84.4$ and $t.U/M = 128.8$ (*figure 4.5*): the PDFs for the two velocity components seem close to each other, which suggest both that the particles sample homogeneously the fluid flow and that the two phases have close velocity statistics.

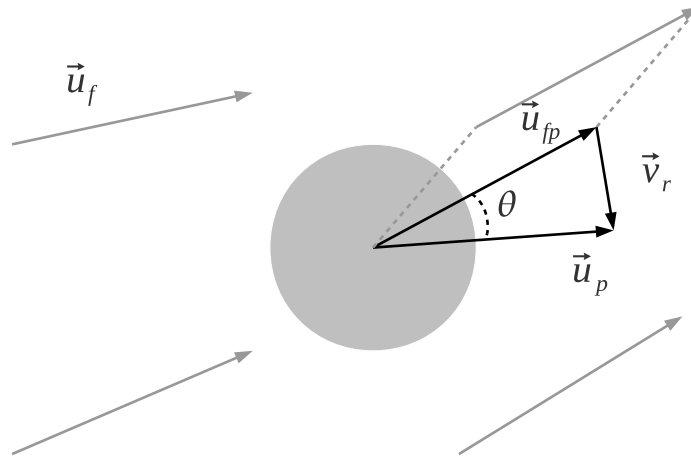
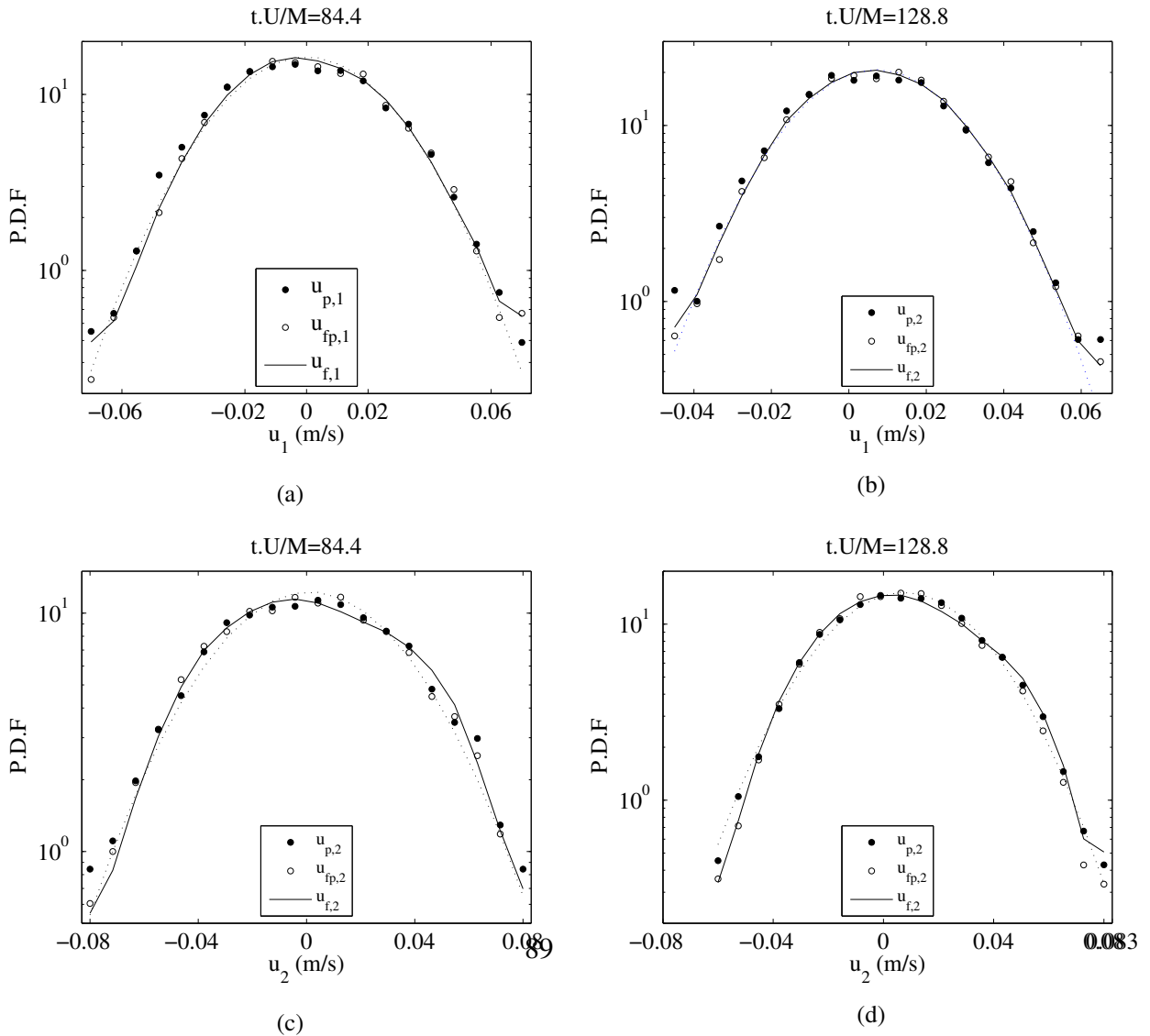


Figure 4.4: Scheme of the computation of the velocity differences. The particle velocity \vec{u}_p is compared to the nearest fluid velocity vector \vec{u}_{fp} , by computing the relative velocity \vec{v}_r and the angle θ between the two vectors. The other fluid velocity vectors in the field are written as \vec{u}_f .



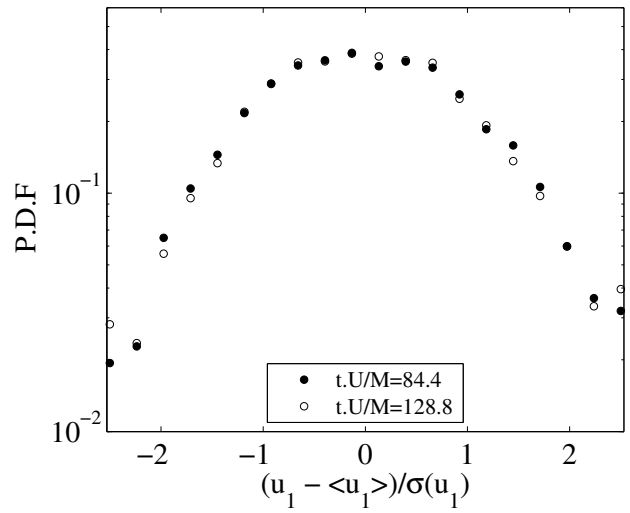
Additionally, the normalized particle velocity P.D.F are compared at two different stages of the decay (*figure 4.6*). Since the mean velocity field is evolving throughout the decay, the mean velocity is subtracted and the result is normalized by the timely particles velocity standard deviation $\sigma(u_i)$. No statistically significant differences are observed between the resulting P.D.Fs, leading us to conclude that the particles normalized velocity P.D.F is self-similar through the decay.

The degree of homogeneity of the spatial distribution throughout the measurement volume is investigated by computing the radial distribution function (RDF) $g_{pp}(r) = n_{pp}(r)/n_p$ which is a measure of the probability of finding two particles separated by a distance r , and is defined as the ratio of $n_{pp}(r)$ the number of particle couples separated by a distance r to the total number over the realizations n_p of detected particle at a given stage of the decay. This operator have been used by several authors to quantify particles clustering (Sundaram & Collins 1997; Xu & Bodenschatz 2008).

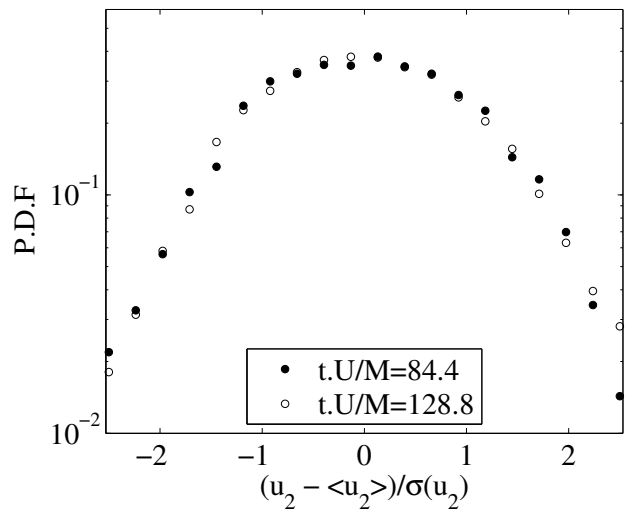
In parallel, we randomly generate a synthetic homogeneous distribution of positions the number, the number of which at each realization is equal to the average number of particles in the measurement volume. We then compute the RDF out of this distribution and compare it the RDF of an actual particle RDF for one stage of the decay as depicted in *figure4.7*. The values of the two functions are fairly close to each others which suggests that the particles have a weak tendency to cluster. However, these conclusions have to be considered carefully : due to the small number of particles in the viewing area (14 in average) particle clusters are difficult to identify.

We turn attention to the comparison of the kinetic energies of the two phases. *Figure 4.6* depicts the temporal decay of mean kinetic energies $e_{c,m} = \frac{1}{2} \langle 2u_1^2 + u_2^2 \rangle$ for each phase. It is shown that the kinetic energies of the particles and the surrounding fluid are close and decay with the same rate, as suggested by the previous comparison of the velocity PDFs. The local and global kinetic energies are also close confirming the fact that the particles sample the flow field homogeneously.

However particle mean kinetic energy is always larger than both local and global fluid mean kinetic energies with a discrepancy of around 6%. The particle velocity component mean squares are also shown to be larger than the local fluid velocity mean square, with a discrepancy ranging from 3.6% to 14.2% for the horizontal component and 3% to 8% for the vertical component. Nevertheless, the energy difference has not been observed to have a clear trend with the decay.

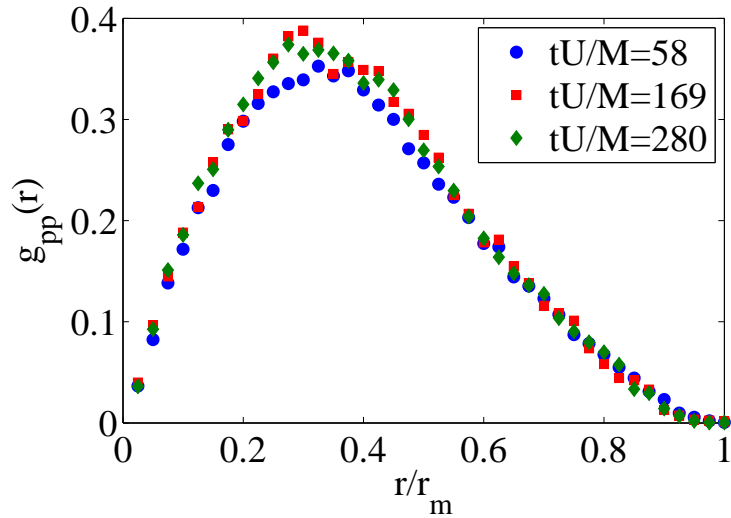


(a)

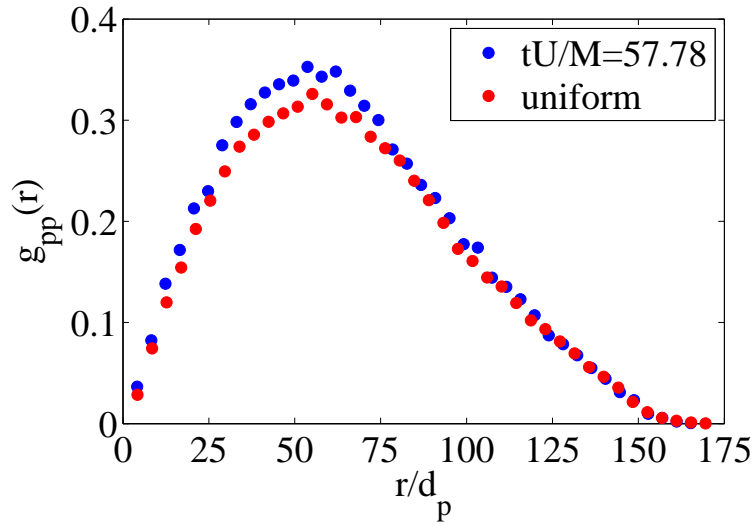


(b)

Figure 4.6: Comparison of the P.D.F of normalized velocities between two stages of the decay: no significant difference is observed between the two P.D.F's, showing that the shape of the normalized PDF remains unchanged throughout the decay.



(a)



(b)

Figure 4.7: Radial distribution function (RDF) compared at different stages of the decay. (a) The separation r is normalized by the maximal detected separation r_m for each case. The values of the RDF are close to each other for the different stages of the decay, suggesting that the spatial distribution of the particles do not vary significantly with the decay. (b) The value of the RDF for the particles at a stage of the decay is compared to the RDF of a computer generated uniform distribution of positions in the viewing area (the separation is normalized by a scale of particle diameters $d_p = 1mm$). The values of the two RDF are found to be close, suggesting that no particle clustering occurs for any stage of the decay.

4.3.2 Discussion

The absence of clustering for the neutrally buoyant particles has been confirmed by other studies, with a higher number of particles (Fiabane et al. 2012; Tagawa et al. 2012). They have shown that the particles remain homogeneously distributed over a significantly large range of Reynolds and Stokes numbers and size ratios (in Fiabane et al. 2012, the Reynolds number is varied from $Re_\lambda = 160$ – 395 and the Stokes number $St = 1.6$ – 24.2). The authors thus conclude that the neutrally-buoyant particles never cluster.

Considering the particles used in this study are perfectly neutrally buoyant, the discrepancy observed in our results between the two phase kinetic energies seem non-physical, since the particles cannot have a larger kinetic energy than the fluid flow by which they are transported. This discrepancy is also in contradiction with the results reported in other studies of neutrally buoyant particles in isotropic turbulence (Homann & Bec 2010; Calzavarini et al. 2012). In these studies the particles kinetic energy has been found smaller than the fluid kinetic energy for a large range of particle diameters. In addition, if spatial filtering (particle finite size effect) is ignored, the Tchen-Hinze theory for the specific case of neutrally-buoyant particles with finite relaxation time predict that the two phases kinetic energies should be equal in an isotropic turbulence, whatever the relaxation time value is (Hinze 1975).

Thus the observed discrepancy is first thought to originate from a bias on particle and/or fluid velocity measurements. This bias may leads to an overestimation of particle displacement and/or an underestimation of the fluid tracer displacement. To quantify the displacement differences of particles and tracers in pixels we computed the average displacement in pixel during the decay; average particle's displacement is found to be always larger by about 0.1 pixels (2.5%) than the average fluid tracers displacement, this discrepancy is rather small with regard to the measurement precisions of both PIV and PTV. In the following the possible bias sources related the two velocimetry techniques will be discussed.

The uncertainty related to the particle tracking velocimetry is mainly due to the uncertainty on the particle images weighted centroid localization, as have been shown in the second chapter. The position of the weighted centroid for each particle image depends on its illumination profile, which may change significantly between the two camera frame (as a consequence of the out of plane motion of the particles, for example); this may induce an “apparent” displacement of the computed centroid not related to the actual displacement of the particle, thus introducing an error on the particle displacement measurement.

The size of the particle images is of 10 *pixels* in average ; if the illumination profile is Gaussian the uncertainty is at least of the order of 0.5 *pixels*. The measurement of the displacement involves the computation of the centroid for the two particle images on both frames ; thus the uncertainty on the displacement is at least of the order of $2 \times 0.5 = 1$ *pixel*. The uncertainty is in fact higher, since the illumination profiles are not Gaussian, but rather saturate over several pixels. However it is not clear why this uncertainty leads systematically to an overestimation of the particles displacement and kinetic energies.

The measurement of the tracers displacement is less sensitive to variation of the light intensity between the two frames, since each cross-correlation computation involves several tracers images. On the other hand, the resulting measured displacement is a spatial average of the displacement of the tracers included in each interrogation window, the resulting measured displacement is biased toward lower values.

4.4 Velocity difference statistics

In this section the statistics of the velocity differences between the particles and the surrounding fluid flow are presented and discussed. The section aim is to investigate the local velocity differences between the two phases and to give an interpretation to these results. A similar approach is proposed by Ouellette et al. (2008) in the case of 2D chaotic flow, and thus a systematic comparison is made with his results for the larger and most inertial particles he used ($d_p = 2mm$, $Re_L = 220$, $St_L = 7.6 \times 10^{-2}$). The main questions guiding the following investigation are: to what extent do the particles follow the motion of the surrounding fluid? And how the spatial and temporal filtering (i.e. finite-size and inertia) effects may influence the particle dynamics?

As detailed in the introduction of this chapter, the velocity differences are expected to occur due to the finite size and inertia of the particles. However, some other origins may also explain the velocity discrepancy, related mainly to the measurements bias.

4.4.1 Results

Before computing the local velocity difference statistics between the two phases we first inspect visually the fluid-particle velocity joint probability density function for each component, represented in *figure 4.9*. Most of the values belong to the median line $x_2 = x_1$, with some non-negligible dispersion about this line. This suggests that the particles mainly have velocities close to that of the fluid, but velocity discrepancy occurs with a finite probability.

To further confirm these observations, the focus is made on the local velocity difference statistics. We compare each particle velocity to the nearest fluid velocity and compute the relative velocity $\vec{v}_r = \vec{u}_p - \vec{u}_{fp}$. In order to compare velocity differences statistics at different stages of the decay, we consider the normalized relative velocity components $v_{r,i} / \sqrt{\langle u_{fp,i}^2 \rangle}$ whose PDF is shown in *figure 4.10* at two different stages of the decay, and compared to a Gaussian distribution. The PDF's shape and values show several interesting features discussed in the following.

The PDFs are weakly skewed, but are flatter than a normal distribution (the PDF kurtosis is estimated to be always larger than 10, although the available number of realizations is not sufficiently large to yield exact estimations of high statistical moments). The shape of the PDF shows the intermittent nature of the two phase velocity differences : mainly the particles follow well the surrounding flow, but large departure from local fluid velocities occurs. Additionally, The PDF's tails seems to be well approximated by an exponential distribution, as is the case for the PDF of eulerian spatial or temporal fluid velocity increments. Moreover, the comparison of the normalized PDFs at two stages of the decay shows that the shape doesn't change significantly throughout the decay. This observation suggests that the local velocity differences are self-similar throughout the decay.

The inspection of the PDF values shows that, although the most probable value of velocity differences is zero, significant two phases velocity discrepancy occurs with a finite, non-negligible probability: Based on the assumption of exponential tails for the PDF, one can show that the particles have a probability of 19% to have a relative velocity equal or larger than half of the r.m.s of the fluid velocity, which corresponds to a displacement close to 2.5 *pixels*. Thus the values of the velocity discrepancy between the two phases are non-negligible and cannot be solely due to measurement bias.

Furthermore, the two relative velocity components may be considered simultaneously through the normalized norm of the relative velocity $w = \|\vec{u}_p - \vec{u}_{fp}\| / \langle \|\vec{u}_{fp}\| \rangle_T$, also considered by

Ouellette et al. 2008. In *figure 4.11* the P.D.Fs of w are shown at the two different stages of the decay and compared to Ouellette et al. 2008: in our experiments the probability of having a finite relative velocity is higher and decays slower with increasing w in our case. However, the two PDFs have close shapes.

The inspection of P.D.F tails shows a finite probability of having velocity differences of the order of the fluid velocity average norm.

To confirm the statistical significance of the local velocity differences we compute the average $\langle w \rangle = \langle \|\vec{v}_r\| \rangle_T / \langle \|\vec{u}_{fp}\| \rangle_T$ which is shown in *figure 4.12* for different stages of the decay. The norm of the relative velocity is to be on average larger than 30% of the fluid velocity average norm $\langle \|\vec{u}_{fp}\| \rangle_T$, we conclude that on average the local fluid velocity discrepancy is larger than the possible measurement bias.

One interesting remark is the slow temporal decay of the normalized velocity differences, which confirms the previous observation of the similarity of the relative velocity norm PDFs between two distant stages of the decay. Additionally, the decay tendency suggests that w decreases with decreasing Reynolds number (since the Re decreases with the decay); this may explain the fact that our values of w are higher in comparison to the values of Ouellette et al. (2008) since the Reynolds number is significantly higher in our case.

The highlighted velocity difference may originate from a difference of velocity norm between the particles and the surrounding fluid or a misalignment of the two velocity vectors. These two causes of velocity differences may be isolated and studied separately by computing the normalized difference of velocity norms $\delta u = (\|\vec{u}_p\| - \|\vec{u}_{fp}\|) / \langle \|\vec{u}_{fp}\| \rangle_T$ and the angle $\theta = \arccos(\vec{u}_p \cdot \vec{u}_{fp} / (\|\vec{u}_p\| \|\vec{u}_{fp}\|))$ between the two vectors. The PDF of these two quantities are represented in *figure 4.13* and *figure 4.14*, and a comparison is made with Ouelette's results.

Concerning the velocity norm differences, the shape of the P.D.F of δu at the two considered stages of the decay are symmetrical, suggesting that the particles are equally likely to move slower or faster than the surrounding fluid. Furthermore the shape of the PDF is flatter than a Gaussian distribution and its tails are also exponential. The inspection of the angle PDF shows that the particles have a finite probability to move in a direction significantly different for that of the fluid. In fact, the particles have an estimated probability of more than 16% to move with an angle larger than $\pi/6$ from the direction of the motion of the surrounding fluid. We conclude that the velocity differences between the two phases are both due to velocity norm differences and misalignment of the velocity vectors.

4.4.2 Discussion

As emphasized previously the velocity difference between the two phases is not negligible and is beyond the measurement uncertainties. It is then thought to have a physical origin, even though the measurement errors contribute to the observed discrepancy. In this subsection, we discuss the possible origins of the observed two phases velocity differences.

As shown previously, a major feature of the velocity differences statistics is their intermittency, which may suggest a link with other intermittent quantities of the turbulent flow, such as acceleration or Eulerian velocity increments.

If the particle inertia is predominant, then the velocity difference is proportional to the particle acceleration, as shown by the Stokes equation. On the other hand, if the finite-size effects are predominant then the velocity differences are proportional to the velocity Laplacian (Homann & Bec 2010). Both quantities are highly intermittent, since they involve spatial or temporal derivative of the fluid velocity.

If finally, both temporal and spatial filtering effects are weak, the particles then behave mainly as tracers. In this case the difference may be attributed to the fact that the velocities are not measured exactly at the same location. Thus the velocity differences are actually velocity spatial increments for separations of the order of the distance between the particles and the closest fluid velocity vector position. This difference obviously increases with the local velocity gradients of the flow. In addition, the effect of filtering of the PIV may also introduce a difference between the two phases. If the particles are tracers, then velocity discrepancy is comparable to a difference between a local value of the fluid velocity and the spatially averaged fluid velocity. This difference, when it exists, is caused by the flow velocity gradient inside the pattern box: the higher the gradients the larger the probability of velocity differences. Both differences origins scale with the fluid velocity gradients, which are intermittent quantities.

4.5 Conclusions

In this chapter, the dynamics of neutrally buoyant particles embedded in the turbulent flow have been measured and compared to that of the fluid. The particles have been found to

distribute homogeneously over the view field. The overall statistics of the two phases have been shown to be close, although a slight difference on mean kinetic energies of the two phases is observed, which is thought to be mainly due to an underestimation of fluid kinetic energy, inherent to the spatial filtering introduced by the PIV measurement.

However, significant local velocity differences between the two phases have been found to occur with a finite probability, and the average velocity difference between the two phases have been found to be significant, suggesting that this difference can be hardly explained by invoking accumulated bias from both PIV and PTV measurements.

Thence, a physical explanation is searched to the observed discrepancy. In their study Ouellette et al. (2008) suggest that the difference is due to the inertial behavior of the particles. We rule out this explanation in our case since, as it is shown by Homann & Bec (2010) and Calzavarini et al. (2012), the inertial effects are not the dominant effects on the dynamics of neutrally-buoyant finite size particles in turbulence, but rather the finite size effects (i.e. spatial filtering). An alternative explanation is to consider the particles behaving as tracers, and the observed discrepancy is then a spatial increments of the velocity between particle position and the closest measured fluid velocity vector.

At this point, no clear conclusion can draw regarding the velocity differences between the two phases. Further investigation with a higher resolution of the measurements and a larger number number of realizations is needed in order to confirm the observations. Besides, the effects of measurements bias on the velocity differences statistics still need to be quantified.

4.6 References

Boivin, M., Simonin, O. & Squires, K.D., 1998. Direct Numerical Simulation of Turbulence Modulation by Particles in Isotropic Turbulence. *Journal of Fluid Mechanics*, 375(-1), pp.235-263.

Calzavarini, E. et al., 2012. Impact of trailing wake drag on the statistical properties and dynamics of finite-sized particle in turbulence. *Physica D: Nonlinear Phenomena*, 241(3), pp.237-244.

Fiabane, L., Volk, R., et al., 2012. Do finite size neutrally buoyant particles cluster? *arXiv:1201.4953*.

Hinze, J.O., 1975. Turbulence 2nd ed., McGraw-Hill Companies.

Homann, H. & Bec, J., 2010. Finite-Size Effects in the Dynamics of Neutrally Buoyant Particles in Turbulent Flow. *Journal of Fluid Mechanics*, 651(-1), pp.81-91.

Ouellette, N.T., O'Malley, P.J.J. & Gollub, J.P., 2008. Transport of Finite-Sized Particles in Chaotic Flow. *Physical Review Letters*, 101(17), p.174504.

Qureshi, N.M. et al., 2007. Turbulent transport of material particles: An experimental study of finite size effects. *Physical review letters*, 99(18), p.184502.

Sundaram, S. & Collins, L.R., 1997. Collision Statistics in an Isotropic Particle-Laden Turbulent Suspension. Part 1. Direct Numerical Simulations. *Journal of Fluid Mechanics*, 335, pp.75-109.

Tagawa, Y., Mercado, J.M., et al., 2012. Three-dimensional Lagrangian Voronoï analysis for clustering of particles and bubbles in turbulence. *Journal of Fluid Mechanics*, 693, p.201.

Xu, H. & Bodenschatz, E., 2008. Motion of inertial particles with size larger than Kolmogorov scale in turbulent flows. *Physica D: Nonlinear Phenomena*, 237(14-17), pp.2095–2100.

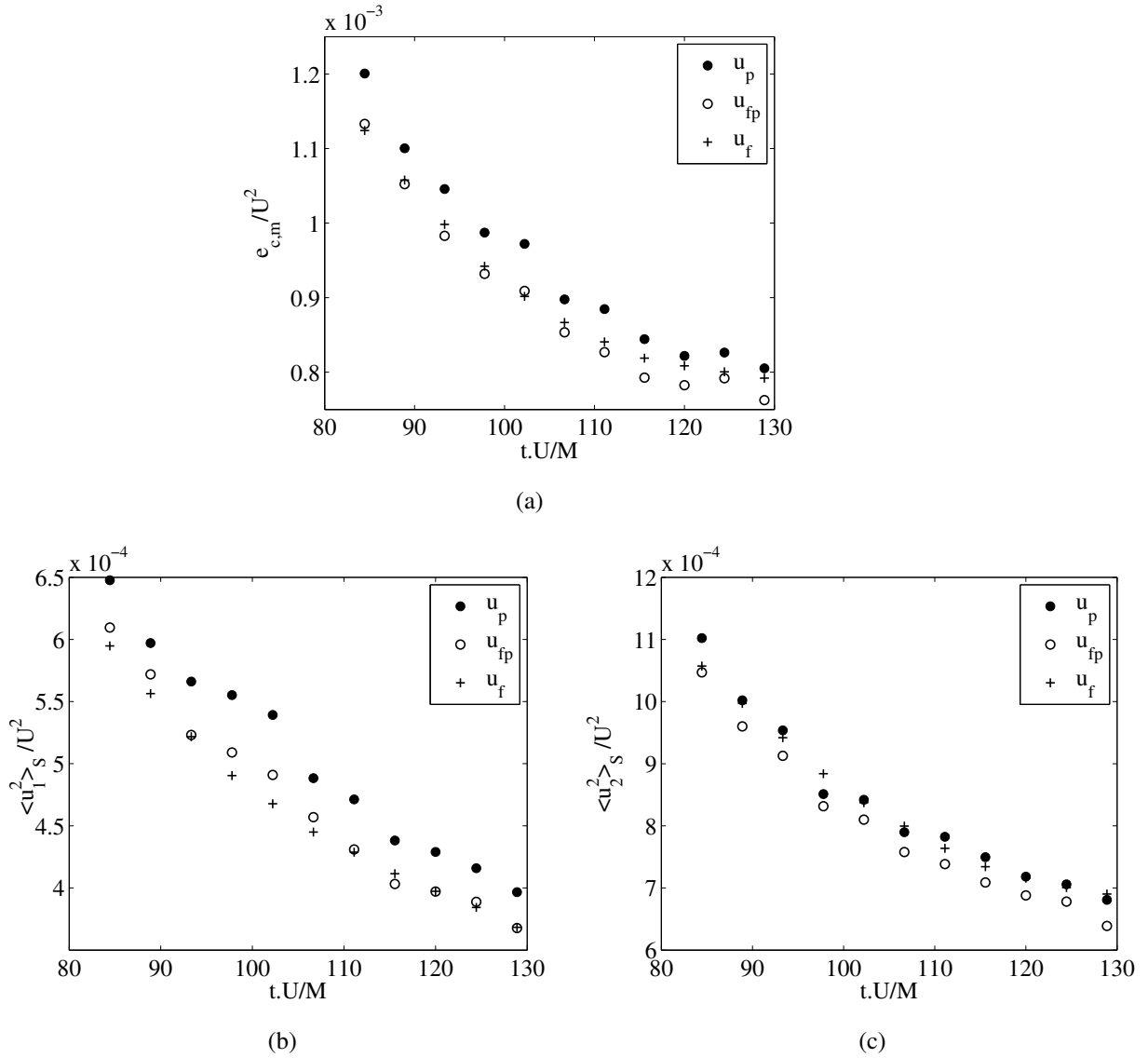
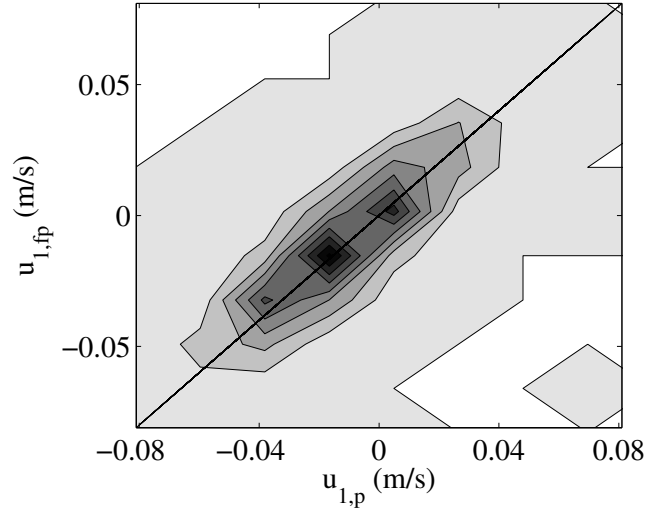
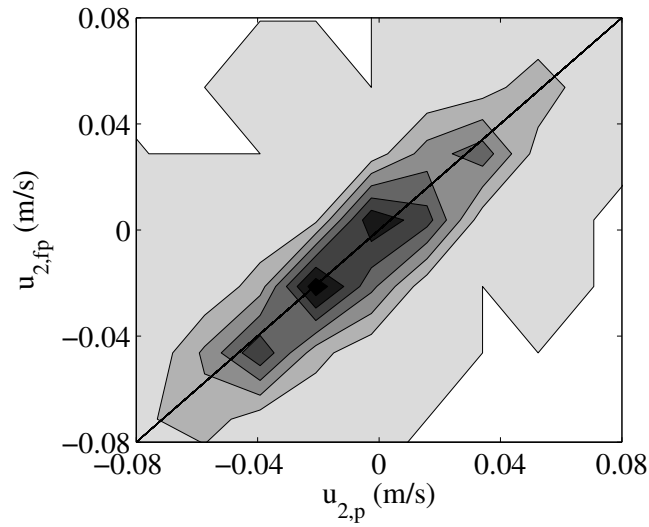


Figure 4.8: (a) Comparison between particles \bullet local \circ and non-local $+$ fluid mean kinetic energies $e_{c,m} = \frac{1}{2} \langle 2u_1^2 + u_2^2 \rangle$: the values remain close, although the particles kinetic energy is always larger than the fluid one. The kinetic energies of both phases decay with the same rate (b)(c) mean square of velocity components : although the decay rates are close, the discrepancy between the two phases is around 10%.

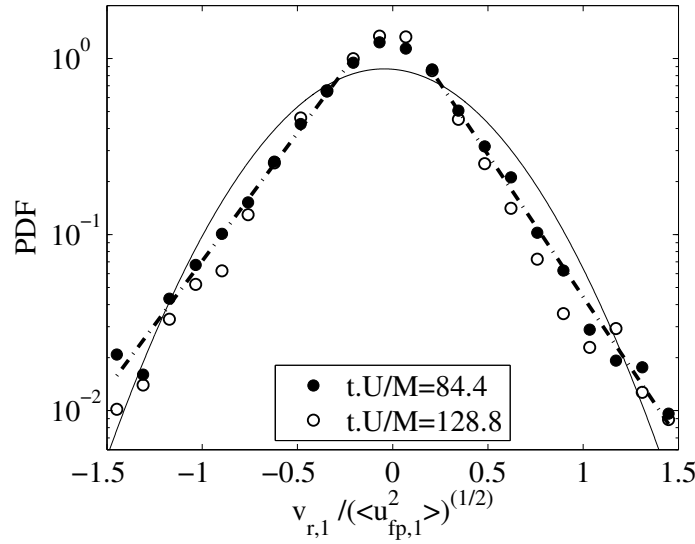


(a)

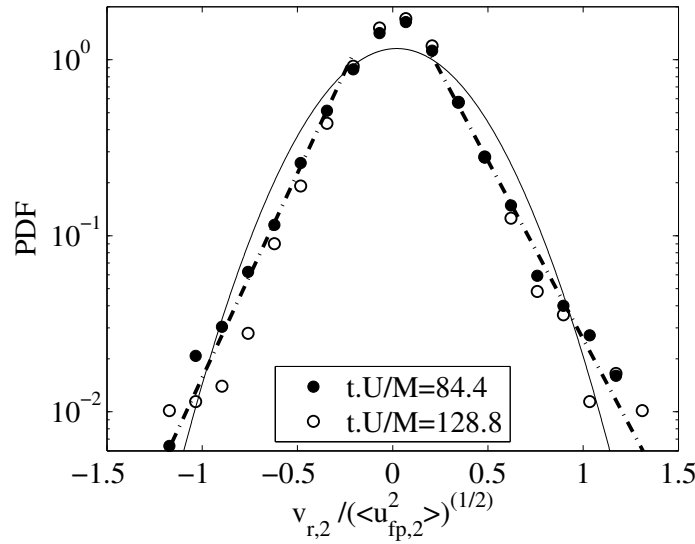


(b)

Figure 4.9: Fluid particles joint probability PDF at $t.U/M = 84.4$, the most darker regions corresponds to the higher probabilities. Solid line represents the median line $y = x$. The most probable values are close to the median line.



(a)



(b)

Figure 4.10: Normalized relative velocities PDF at two different stages of the decay. The continuous line represents the Gaussian distribution. The dashed line represents an exponential distribution, with the following decay rates (a) right tail : -4.66 , left tail 5.34 (b) right tail : -3.71 , left tail: 3.34 . The tails of the velocity PDF at time $t.U/M = 84.4$ are shown to fit well the exponential distribution.

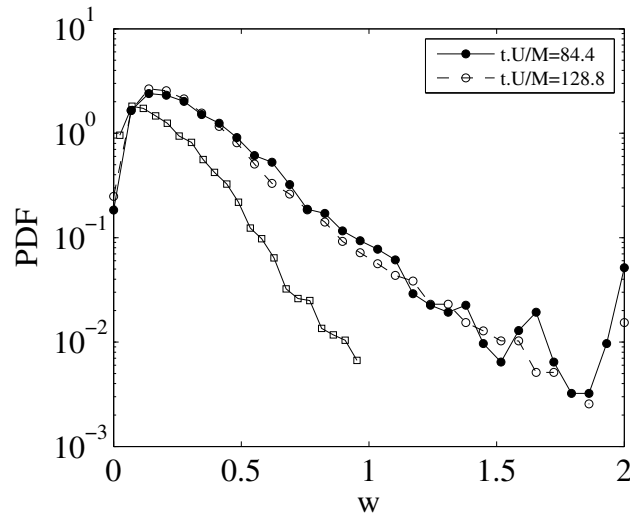


Figure 4.11: P.D.F of the normalized relative velocity norm $w = \|\vec{u}_p - \vec{u}_{fp}\| / \langle \|\vec{u}_{fp}\| \rangle_T$ at two stages of the decay with comparison to Ouelette & al. (2008) (\square)

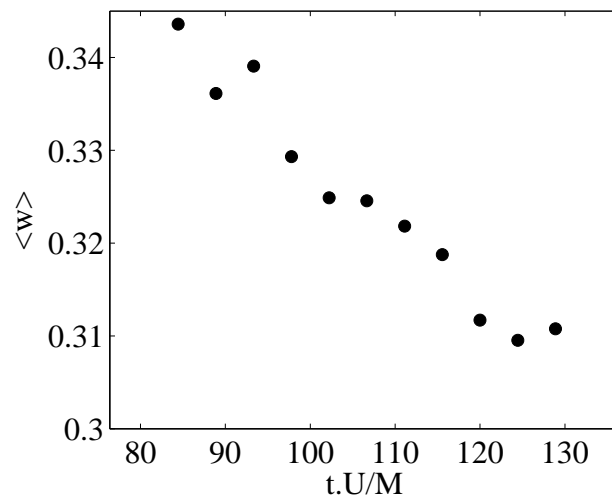


Figure 4.12: Temporal decay of the average relative velocity norm. The value of $\langle w \rangle$ is shown to drop by 11% during $60M/U$.

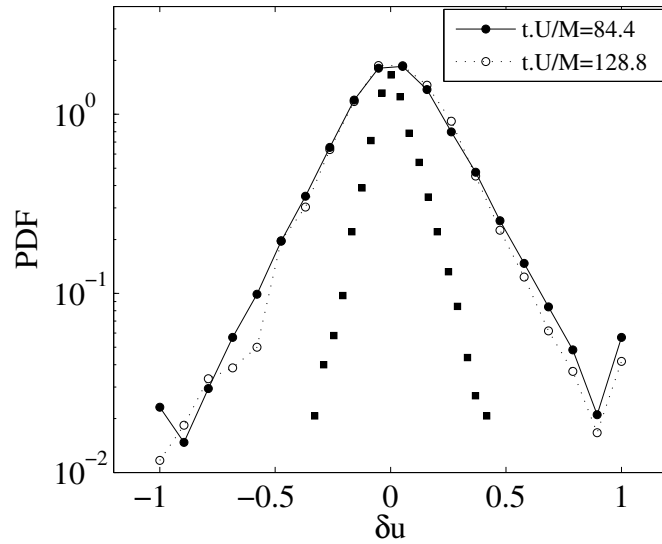


Figure 4.13: Velocity norm difference $\delta u = (\|\vec{u}_p\| - \|\vec{u}_{fp}\|) / \langle \|\vec{u}_{fp}\| \rangle_T$ P.D.F at two stages of the decay with comparison to Ouelette & al. (2008) (■).

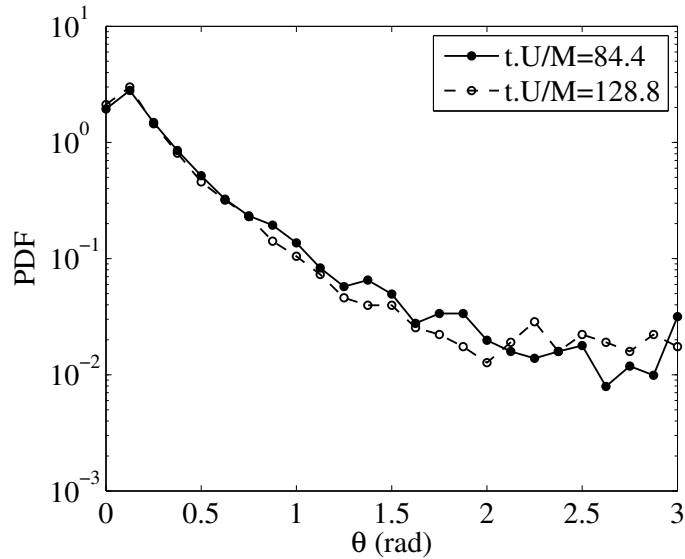


Figure 4.14: The angle $\theta = (\vec{u}_p, \hat{\vec{u}}_{fp})$ P.D.F at two stages of the decay.

5 Conclusions and Perspectives

In this experimental study, the focus is made on the characterization of the dynamics of solid neutrally buoyant particles embedded in a freely decaying, nearly isotropic turbulence, with a weak mean flow. The particles are spherical with diameters several times larger than the flow Kolmogorov length scale, but smaller than the integral scale. Due to large particle sizes, the local flow around particles can not be considered as uniform and due to fluid-particle density ratio of around unity, the history and Basset forces cannot be neglected in comparison with the viscous drag force.

Particle equation of motion is then fully non-linear, in contrast to the equation for heavy particles with diameters smaller than the Kolmogorov scale, for which only the Stokes drag is considered (Homann & Bec 2010). Recently Ouelette & al. (2008) have studied experimentally the dynamics of small, neutrally buoyant particles embedded in a two-dimensional chaotic flow. The particles have been shown to have velocity and acceleration statistics close to that of the fluid, but locally, the particles often move with velocities different from the surrounding flow.

The aim of the present thesis is to generalize study Ouelette & al. (2008) to the case of three-dimensional, fully turbulent flow. This flow configuration have not been studied experimentally, and its numerical study is very expensive, due to the necessity of resolving the fluid flow around each particles.

To that purpose, a towed grid turbulence generator has been set-up: one realization of the turbulent flow is produced by moving the grid upward in a water tank with a constant velocity, the generated turbulence then decays freely until the next stroke. First the characteristics of the the resulting turbulence have been measured using a standard Particle Image Velocimetry (PIV) technique. Our results shows that the used apparatus yield a turbulent flow which can be considered fairly homogeneous and isotropic; in addition, the local isotropy is found to be verified for the smallest measurable separations.

Then the flow was seeded with neutrally-buoyant particles of size 4 times larger than the flow Kolmogorov length scale and with a Stokes number around 1, so that finite size and inertia effects are expected to influence particles dynamics. In order to measure the velocity of the particles and the surrounding fluid simultaneously, the two measurements techniques, PIV and PTV, were combined in a two camera set-up where each camera is dedicated to one phase. The flow was seeded with fluorescent tracers and the dedicated camera equipped with a cut-off filter, thus receiving only the fluorescence signal and avoiding to catch the light reflected by the large particles. This method have been shown to enable successfully the measurement of the fluid velocity close to the particle.

The aim of the investigation was to reveal any global or local differences between the dynamics of the two phases. We first compared the statistics of the two phases: The global velocity statistics of the two phases have been shown to be close, although a discrepancy of the 6% between the mean kinetic energies of the particles and closest fluid is noticed. This discrepancy is non-physical, since the particles cannot have a larger kinetic energy than the flow by which they are transported. It is thought to be due to an error on particles images tracking which may induce an overestimation of particles displacement of less than 3% in average, or to an underestimation of the fluid flow kinetic energy caused by the filtering of the velocity field resulting from the PIV measurement.

In addition the spatial distribution of the particles have been investigated by computing the radial distribution function (RDF). The particles have been shown to distribute homogeneously, in agreement with other studies on the clustering of neutrally buoyant particles. However, the clustering cannot be detected in our case due to the small number of particles in the visualization field (14 in average).

Then the focus is then made on the statistics of the local velocity differences between the two phases: We compare each particle velocity \vec{u}_p to the closest fluid velocity vector \vec{u}_{fp} by computing the relative velocity $\vec{v}_r = \vec{u}_p - \vec{u}_{fp}$. The important results of our measurements is that the norm of the relative velocity is to be on average larger than 30% of the fluid velocity average norm for the considered stages. Thus, the velocity differences are not negligible, and can be hardly explained by measurements bias only. In addition, the velocity difference between the two phases have been found to result from both misalignment and norm differences between the two velocity vectors.

The observed discrepancy is thus considered to have a physical origin, and several possible interpretations are discussed. In their study, Ouelette & al. (2008) conclude that the observed

difference is due to the particle inertia. However, other interpretations can be proposed: in addition to spatial or temporal filtering effects on particles dynamics due to their finite size and inertia, the difference may also be attributed to the PIV spatial filtering of the fluid velocity field, or to the fact that the particle and fluid velocities are not measured at exactly the same position. The precise origin of the observed velocity difference is still unclear and is currently under investigation.

As emphasized in the introduction, an important aspects of the dynamics of the neutrally buoyant particles is the dependence of their velocity statistics with their size; this can be investigated using our experimental set-up by adding particles with larger diameters. We have tested the feasibility of applying simultaneous velocimetry techniques to particles of diameter of 4 *mm*. Since they have a larger surface, the particles reflect more fluorescence light than the 1 *mm* particles, thus a higher intensity threshold need to be applied to PIV images, which will yield an increased number of holes and generally poorer PIV images quality. Thus, the application of the simultaneous velocimetry to larger particle is not straightforward and specific problems may arise, which require an adaptation of this technique.

In addition, the constructed turbulence generator may also serve to study other two phases flows: the rise of bubbles or the settling of particles in turbulence, although an appropriate feeding system must be added to the existing set-up in order to enable the control of the instantaneous mass loading of the particles.